Origins of Variability in Electron Beam Powder Bed Fusion of Ti6Al4V

Sean S. Ghods

A dissertation

submitted in partial fulfillment of the

requirements for the degree of

Doctor of Philosophy

University of Washington

2021

Reading Committee:

Dwayne Arola, Co-Chair
Ramulu Mamidala, Co-Chair
Lucas Meza

Program Authorized to Offer Degree:

Materials Science and Engineering

University of Washington

Abstract

Origins of Variability in Electron Beam Powder Bed Fusion of Ti6Al4V

Sean S. Ghods

Chairs of the Supervisory Committee:
Dr. Dwayne Arola, Materials Science and Engineering
Dr. Ramulu Mamidala, Mechanical Engineering

Additive Manufacturing (AM) processes for metals are advancing at a rapid pace. Among many attractive qualities, AM relaxes design constraints, enables customization and can significantly reduce material waste in comparison to subtractive manufacturing processes. However, there are some fundamental issues that must be addressed for metal AM to become prevalent in aerospace. Most critical is the reliability of the mechanical properties of the metal and an identification of contributions (i.e., the root causes) to the mechanical variability.

In powder bed fusion (PBF) AM, powder reuse from previous build cycles is desired to improve process economics. However, there is limited understanding of the contributions from feedstock reuse to particle-powder-properties and part quality. The first half of this dissertation investigates this topic in electron beam melting (EBM) powder fusion AM of a titanium alloy

(Ti6Al4V) over 30 cycles of build and powder reuse. Results show that nearly all aspects of the process are influenced by powder reuse. Specifically, the particle size distribution tightens with reuse, but particle damage increases, which includes surface deformation (reduction in sphericity), partial melting and/or particle fusion and fracture. While no changes in the concentration of Al, V, Fe, H and N occur, there is a significant increase in Oxygen with reuse, which exceeded the concentration limit (0.20%) in just 11 build cycles. Results showed that the strength of the metal increased with powder reuse, whereas the ductility decreased significantly, both relevant to the damage tolerance of the metal.

Powder reuse covers inter-build variability but not address the intra-build variability. Establishing an understanding of the mechanical response variation within a build is also necessary for quality control in metal AM. A design of experiments approach was adopted to determine the relative effects of part location, geometry, and proximity on quasi-static and cyclic properties of the metal. Significant effects were found from the radial distance from the center of the build plate and from the thickness of the parts to the ductility and fatigue life. The highest ductility and fatigue life can be obtained from part placement near the center of the build plate and with increasing thickness. This knowledge makes a fundamental contribution and supports successful application of EBM additive manufacturing for stress-critical components in aerospace and beyond. Nevertheless, more expansive efforts are necessary to further mature the technology, such that it can be integrated into aerospace manufacturing as a reliable production process.

TABLE OF CONTENTS

LIST OF FIGURES

LIST OF TABLES

Some passages have been quoted verbatim from the following sources:

S. Ghods, R. Schur, E. Schultz, R. Pahuja, A. Montelione, C. Wisdom, D. Arola, M. Ramulu, Powder reuse and its contribution to porosity in additive manufacturing of Ti6Al4V, Materialia. 15 (2021) 100992. https://doi.org/10.1016/j.mtla.2020.100992.

S. Ghods, E. Schultz, C. Wisdom, R. Schur, R. Pahuja, A. Montelione, D. Arola, M. Ramulu, Electron beam additive manufacturing of Ti6Al4V: Evolution of powder morphology and part microstructure with powder reuse, Materialia. 9 (2020) 100631. https://doi.org/10.1016/j.mtla.2020.100631.

ACKNOWLEDGEMENTS

During my time at the University of Washington (UW) I have had the immense pleasure of working with many wonderful individuals. My time here has shaped who I am today, and I am proud to have completed my degree at this institution.

Dr. Dwayne Arola has been an incredible advisor, constantly providing insightful guidance that has led me to where I am now. During my time in his group, I have been able to work on numerous projects, which he encouraged and thus allowed me to expand my expertise and determine what aspects of the materials science field interest me. I am truly grateful for all his help during my time at UW.

Dr. Ramulu Mamidala has also been an amazing mentor. Specifically, I appreciate the push provided to complete the degree. Dr. Ramulu wishes to see his students accomplish as much as they can, an important characteristic in a teacher and mentor.

I would like to thank Stacy Huang and the other Boeing representatives for their continued collaboration and motivation of the work presented in this dissertation. Research conducted and provided here would not have been possible without their funding and frequent thoughts about the research.

Thanks to all the various students that assisted with many portions of this research, whether through data collection, analysis, or discussions. Collaboration with my colleagues is the only reason this effort was successful and would not be completed without their help.

Finally, I would like to thank the staff and engineers that trained me on the equipment used in this research. Their training essential to my ability to conduct experiments.

To my friends and family, you are the reason I continued with this process and achieved this level of education. It was arduous, but through your support I made it through. Especially, the constant “are you done yet?” comments.

DEDICATION

To my loved ones

Chapter 1. INTRODUCTION

1.1 CURRENT STATE OF METAL AM

Additive manufacturing (AM) is making the transition from a research topic to a viable method of manufacturing for a variety of industries. Advancements in technology and understanding have overcome many challenges and raised the feasibility of its application for nearly every class of materials. AM offers greater flexibility in design and unique component geometry, as well as lower material waste and potential for lighter and more efficient structures. Indeed, review articles encompassing AM highlight its adoption and growth as a potent and enabling method of manufacturing [1,2].

With progress still to be made, the adoption of metal AM appears to be growing at an impressive rate [3,4]. A number of reviews have been reported over the last decade that chronicle various aspects of metal AM [5–7]. There are immense benefits to the technology such as significantly reduced material usage from both optimized geometry and low stock material usage [8]. Nevertheless, there are some critical challenges to overcome, including the relatively lengthy manufacturing time [9,10]. The variation in the quality and corresponding mechanical properties of the metal require statistical qualification of the processes [11] and computationally intensive modeling [12,13].

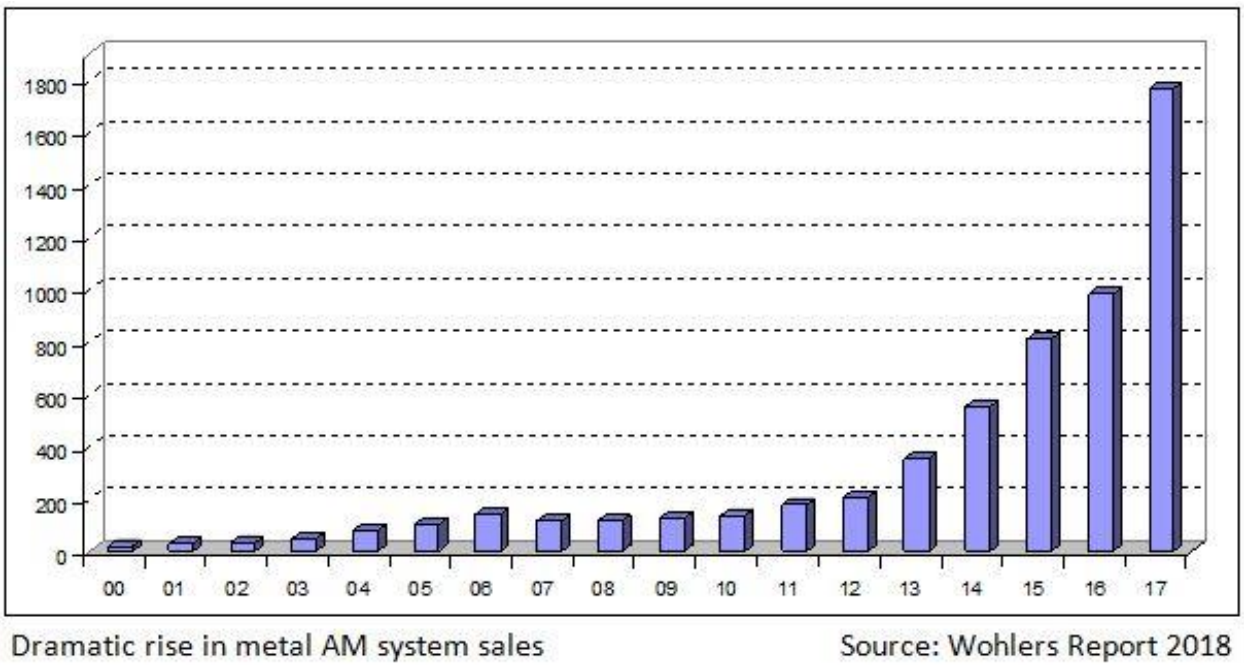

Figure 1.1. Annual expenditure on metal AM products in millions of USD **Error! Reference source not found.**.

The opportunities for metal AM to be used for manufacturing components intended for stress-critical applications has caused need for greater understanding of the process. Contributions of various factors to the quality of metal produced including the process parameters (beam power, beam size, hatching patterns, etc.) and design parameters (build space optimization, location, orientation, etc.) are primary concerns [14]. Their contribution to the microstructure, chemistry, and defects of the built metal, as well as the resulting mechanical properties are key for AM processes [15]. For example, the contributions of part spacing and location to these qualities has been investigated, with only minor contributions in properties from part size [16]. The build orientation can alter the β grain distribution in Ti6Al4V parts with grain texture being different near the contour vs the melt pool [17]. The orientation also alters quasi-static tensile properties of as-built parts, with lower elongation at break reported for parts oriented along the build direction

in comparison to those aligned transverse to that orientation (i.e., in the build plane) [18]. This is corroborated by another group where they show β grains are coarsening with build height in AM Ti6Al4V, which causes increases in the yield strength and hardness with build direction [19]. Reinforcing this knowledge together with computer modelling is of substantial interest in metal AM to improve consistency of parts printed [20]. This understanding and modeling of the process is essential for AM processes to be used be adopted for a greater number and variety of applications.

The Electron Beam Melting (EBM) powder bed fusion process involves distributing a layer of powder metal across the build layer and then selectively sintering and melting using an electron beam. Partial sintering is performed to prevent electrostatic build up and particle repulsion before the melt beam can raster [21]. Additional layers of powder are deposited, sintered and melted sequentially to complete the required build. The chemical and physical characteristics of the powder are important to this process and can influence the mechanical properties of the components [14].

There are a number of aspects of powder handling and the build cycle in EBM that can influence the powder quality, such as adsorbed water from ambient humidity leading to oxidation [19]. While powder reuse is pursued to lower material waste and improve process economics, it has important implications to powder quality and the consequent part properties and performance. Thermal cycling of the powder during the build process could alter the microstructure of reused powder [22]. Furthermore, the extraction process during recovery can cause physical damage [23]. The retrieved powder is generally mixed with virgin (unused) powder, which is distributed through the volume in the subsequent build cycle. Previous studies have investigated powder reuse and focused on particular aspects of the powder, such as the oxidation distributions [24] for other

materials like Inconel and 17-4PH steel [25,26]. However, a rigorous understanding of contributions from reuse to part microstructure and properties has not been developed for Ti6Al4V. One limitation is that most studies have performed a limited number of reuse cycles, typically15 or less use cycles [27]. Renishaw plc has reported the most extensive to date, which involves 38 reuse cycles but was performed with a selective laser melting (SLM) system and using extra-low interstitial (ELI) titanium powder [28].

One complication to this issue of powder reuse and its contributions to mechanical properties of the metal, is the different methods of powder manufacturing. Powders for metal AM are produced using processes such as gas atomization (GA) and the plasma rotating electrode process (PREP). As a result of their respective manufacturing techniques, there is variability in the characteristics of powders from the different companies [14,29]. The spectrum of materials and their unique compositions (e.g. Ti6Al4V vs. 17-4PH) is equally important to powder reuse; their passivity, the alloy content and degradation from certain interstitial contaminants are all highly relevant. Mechanical properties of the powder will also affect the powder morphology in regard to its resistance to surface damage and deformation. There are many concerns that remain to be addressed in powder reuse for metal AM.

A fundamental concern to all metal AM processes is porosity of the metal [6]. Pores causes stress concentrations that degrade the mechanical properties and reduce the reliability of AM parts [30]. Process control is key to minimizing porosity and maximizing the component quality. Understanding the origins of porosity and how to minimize it are prerequisites to the use of AM for stress-critical components. Recent efforts have focused on understanding the mechanisms contributing to their generation [31] and developing relationships between the formation of these

pores and the process parameters, such as laser beam speed and power [32,33] and powder characteristics [34].

Of the candidates for metal AM processing, EBM is reportedly capable of producing components with very low porosity, as low as 0.1 % by volume [14]. But powder spreading and choice of electron beam parameters are key to achieving fully dense parts [19,35]. An overall low porosity, but poor control of pore size and pore distribution, can be detrimental to the mechanical properties and component reliability. Furthermore, tight control of porosity for a single build, but inconsistent levels of porosity over multiple builds can have equally dire consequences. Another approach is to utilize post-processing to reduce the potential degradation of metal quality posed by pores. Utilizing post-processing to reduce the severity of pores using such as hot isostatic pressing (HIP) is another approach being explored for industrial applications [36–38].

Owing to its prevalence in nondestructive inspection [39], microcomputed tomography (μCT) is a viable approach for quantifying the pore distributions in AM parts [40]. But the ability to characterize porosity from the μCT reconstruction requires appropriate image analysis techniques and sequences [41,42]. Data from the reconstructions are being investigated for statistical qualification analysis [43]. Vastola et al. (2018) introduce computer modeling of melt dynamics along with statistical methods to qualify part porosity. Apart from these areas of emphasis, powder reuse is an important topic in metal AM, but its contribution to the porosity distribution and its evolution through the subsequent builds has received limited attention.

In AM of nickel and titanium alloys, the effects of powder reuse on printed metal properties has been investigated for both the Selective Laser Melting (SLM) and EBM processes [25,27]. Evolution in the powder microstructure [22] and the distribution of Oxygen in the microstructure of reused powder has been investigated for Ti6Al4V [24]. There are apparent changes to the

powder morphology with reuse [23] and a reduction in the flowability [19], which may influence the consistency of the powder distribution process and the packing factor, both relevant to metal porosity. But the importance of powder reuse to the porosity and its distribution in AM of metals has received limited attention overall. This is a critical issue that must be addressed before metal AM can be considered a viable manufacturing process for the commercial aerospace industry.

This investigation is focused on understanding the ramifications of powder reuse in EBM on the microstructure and mechanical properties of Ti6Al4V. Specifically, the effort involves 30 build and reuse cycles, the largest of any reported study in a peer reviewed investigation. The investigation addresses the changes in powder chemistry and particle size distribution with reuse, their contributions to the microstructure of the built metal and their overall contribution to its mechanical behavior.

Powder reuse could be considered an “inter-build” factor because the powder condition can change between builds. It is potentially one the most prominent variables from build to build. Powder degradation is only one of the factors that may contribute to the metal properties and changes over a production period. Another important concern is the variation in metal properties over the build envelope, which involves both design and manufacturing concerns, including part geometry, location, orientation and proximity. This can be considered “intra-build” variation because properties of the printed metal could vary spatially within a single build based on the process physics. This is an important aspect of metal AM that needs to be fully understood.

Design optimization is generally focused on geometry and a key benefit to AM is the opportunity to optimize topology for minimizing part mass [1,45]. The resulting geometry may include thin wall structures where internal struts narrow to only a few millimeters wide [46]. Consequently, understanding mechanical property dependence on part dimensions is warranted.

The next step is the intelligent placement of parts within the build envelope, which involves location, orientation, and adjacent part proximity. These are the staples of Design for Additive Manufacturing (DFAM) in metal powder bed fusion. Part orientation is potentially the most important of the three [18,36]. Apart from its importance to performance, part orientation affects the feasibility of builds, i.e. a complex lattice structure may have struts oriented one direction which would necessitate that the build direction follows to avoid unnecessary support structures or poor dimensional accuracy [45]. Finally, orientation could affect cost and part density [47] as well. Location and proximity are typically only considered by manufacturing engineers as metrics for optimizing material usage and time. Thus, parts are typically close to the build plate, to minimize build height and the extra time required to complete builds with parts placed at larger vertical distances from the build plate. Also, parts will likely be clustered to minimize build height if the parts can fit tightly at a lower z position. The aforementioned factors (i.e., geometry, orientation, location and proximity) may contribute to properties and should be included in the present study to achieve a robust understanding.

1.2 Specific Objective and Aims

The overarching goal of this research is to develop an understanding of mechanical property variability in EBM of Ti6Al4V resulting from powder reuse and both inter- and intra-build variations. Identifying and understanding the contribution of the most important factors to the damage tolerance of this metal is a prerequisite to the application of powder bed fusion AM across the aerospace industry. Control of these key factors can diminish the potential contributions of chemical, microstructural, and other related defects to the mechanical properties and consequently

reliability of the metal in structural applications. The following aims of this research will be pursued:

Aim 1: To evaluate the changes in powder chemistry, morphology, and flow characteristics of metal powder resulting from its reuse and their effects on the resulting microstructure and properties of Ti6Al4V components.

Aim 2: To evaluate the effects of powder reuse on the internal defects of parts utilizing X-ray MicroCT non-destructive examination and determine any changes in defect characteristics with powder reuse.

Aim 3: To evaluate the effects of key build space parameters (position, geometry, and proximity) on the microstructure, defects and mechanical properties associated with monotonic loading to failure.

Aim 4: To evaluate the effects of the key build parameters outlined in Aim 3 on the stress-life fatigue performance.

1.3 Definition of Acronyms

The following acronyms are used prevalently throughout the rest of the document:

AM: *additive manufacturing*, a computer-controlled method of processing used to produce 3D components by depositing material in a layer-by-layer manner.

PBF: *powder bed fusion*, an AM process in which a bed of powder feedstock is layered and exposed to an energy source that melts and fuses the powder into contiguous material.

EBM: *electron beam melting*, a powder bed fusion process where metal powder is melted by an electron beam energy source.

SLM: *selective laser melting*, a powder bed fusion process where metal powder is melted by a laser beam energy source.

LOF: *lack of fusion*, a defect present in powder bed fusion metal parts that is characterized by incomplete fusion of the powder particles into contiguous metal. LOF defects are typically caused by insufficient energy of the electron or laser beam.

XCT/µCT: *x-ray micro-computed tomography*, non-destructive inspection technique where a material is rotated and exposed to an x-ray source, then the radial x-ray images are compiled to produce a 3D model of the part.

DOE: *design of experiments*, statistical experimental design typically employed for efficient time and material usage while allowing for thorough statistical understanding of factor effects on properties.

Chapter 2. EVOLUTION OF POWDER CHARACTERISTICS AND PART MICROSTRUCTURE WITH POWDER REUSE

2.1 SYNOPSIS

Additive Manufacturing (AM) processes for metals are advancing at a rapid pace. Among many attractive qualities, AM relaxes design constraints and can significantly reduce material waste in comparison to subtractive manufacturing processes. However, there are some fundamental issues that must be addressed for metal AM to become prevalent in aerospace. In powder bed fusion AM, powder reuse from previous build cycles is desired to improve process economics. However, there is limited understanding of the contributions from powder reuse to particle and part quality. The present study investigates this topic in electron beam melting (EBM) powder bed fusion AM of a titanium alloy (Ti6Al4V) over 30 build cycles (~480 hr of build time) and powder reuse. Results show that nearly all aspects of the process are influenced by powder reuse. Specifically, the particle size distribution tightens, largely due to fewer particles with small diameter. Particle damage increases with reuse, which includes surface deformation (reduction in sphericity), partial melting and/or particle-particle fusion and fracture. Regarding the built metal, the microstructure exhibits increasingly finer basket weave and greater surface area to volume ratio of α with reuse. Yet, there are no apparent trends in α-lath thickness or volume. In the analysis of composition, no substantial changes in the Al and V alloy content are apparent, nor in Fe, H and N. However, the O concentration of the powder increased significantly with reuse and exceeded the concentration limit (0.2%) in just 11 build cycles. Overall, powder reuse should be considered carefully in the development of titanium parts for performance critical applications by EBM.

2.2 MATERIALS AND METHODS

The powder used in this study consisted of a Grade 5 Titanium alloy (Ti6Al4V) that was produced through plasma atomization and was acquired from the machine manufacturer (ARCAM: Batch P1303, Part #430944). Thirty consecutive builds were conducted over a period of approximately 6 months. The builds were defined from b1 for the first build performed with 50 kg of virgin powder and subsequently up to b30 for the final build. No new powder was added to the original 50 kg of powder after b1.

The printing process was conducted with an ARCAM A2X Electron Beam AM system. The filament used with this system consists of lanthanum hexaboride. Printing was conducted according to the default parameters of the machine, which includes beam speed of 4530 mm/s, beam current of 15 mA, max current of 20 mA, focus offset of 25 mA and speed function of 45. The preheat temperature for the default theme was set at 650 °C. The 30 build cycles accumulated to approximately 480 hours of total build time under the aforementioned conditions.

2.2.1 *Build Design*

A "core" build was designed for the investigation including a set of specific parts that was followed for each build (Figure 2.1a). These parts were present in all builds and in the exact same locations to avoid variability. The coordinate system for the build is defined by ASTM F2924-14. The center of the build plate was vacant to enable other parts to be built as needed. When additional parts were included, they were placed as far from the core parts as possible to minimize changes in the thermal profile of the build environment. The builds performed with additional parts were noted and considered in the analysis. The core build design consumed approximately 0.4 kg of powder each build. After completing the final build, approximately 35 kg of powder remained, which was slightly less than the residual volume expected of 38 kg when accounting for build consumption

alone. The difference is due to the loss of fines, spillage and small portions remaining within the PRS chamber.

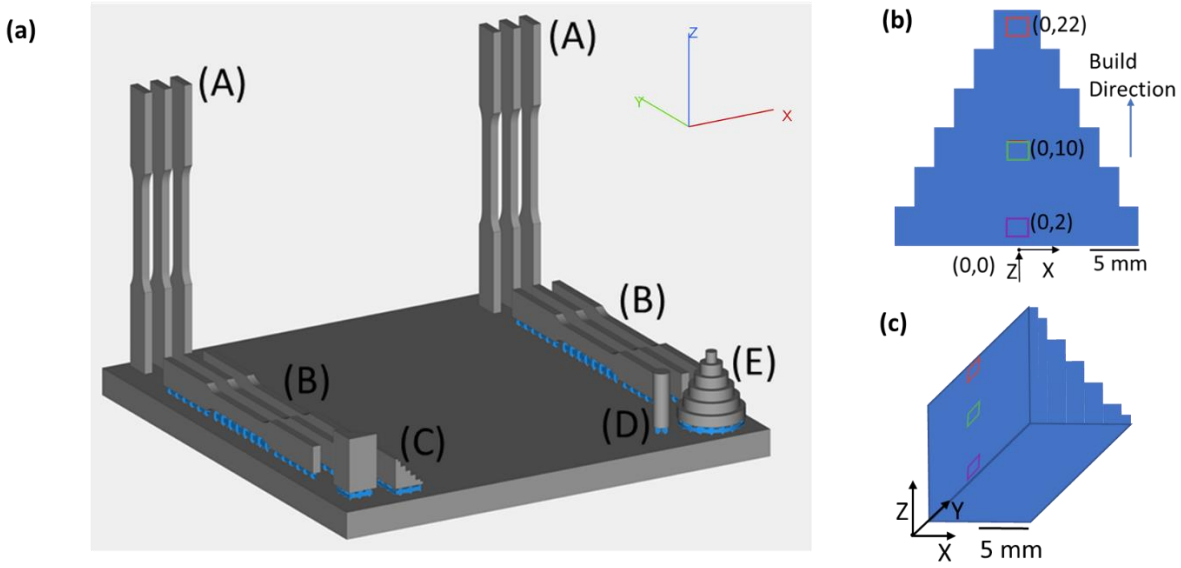

Figure 2.1. Details of the manufactured specimens. **(a)** Schematic diagram of the parts and their distribution in each build. Parts in each build include (A) six vertical and (B) six horizontal oriented flat tensile specimen (ASTM E08M), a (C) vertical and horizontal oriented staircase, a (D) small cylinder, and (E) a cylindrical step pyramid. **(b)** geometry of the staircase specimens and **(c)** pyramid specimen showing relevant dimensions and locations of repeated microstructural analysis.

To explore the importance of powder reuse on powder and metal quality, two different specimen geometries were adopted, including a staircase and a pyramid (Fig. 1b). The staircase dimensions are 11 mm x 11 mm x 20 mm. Each step of the staircase is 2 mm by 2 mm except for the top and bottom stair, which are both 1 mm by 1 mm. There is a total of 7 steps. The pyramid is 24 mm tall with a radius of 12 mm. Each step of the pyramid is 4 mm tall and 2 mm wide (total of 6 steps).

Two identical staircase specimens were printed in each build, including one each with vertical and horizontal orientation. The two different orientations were used to explore the effects of thermal profile and boundary conditions on the metal microstructure. A cylindrical pyramid was included to have a similar reduction in layer area with distance from the build plate, and an axisymmetric thermal profile. Locations chosen for microstructural analysis are outlined in the schematics of the horizontal staircase and pyramid parts in Figure 2.1b. Finally, the core build design also included a uniform cylinder printed in a vertical orientation for porosity analysis and a set of horizontal and vertical flat tensile specimens, conforming to the ASTM E08M subsize standard. Six specimens each were printed in these two directions and for each build.

2.2.2 *Powder Reuse*

ARCAM recommends mixing of virgin powder in between each build to maintain powder volume and quality. However, this practice was circumvented herein to accelerate powder aging, which introduces a worst-case scenario and intentionally exacerbates the effects of reuse. Care was taken to avoid extraneous contamination of the powder in all steps. When a build is completed in EBM the chamber must reach the appropriate temperature for safe removal of the parts. To minimize degradation from atmospheric elements (O, N, and H), the builds were allowed to remain under helium in the build chamber until it reached ~25 °C. All builds followed this routine for consistency. After opening the chamber door, all loose powder was vacuumed out using a dedicated vacuum, which is only used for uncontaminated powder. The thermocouple was removed from the bottom of the build plate and all partially sintered powder was transferred to the Powder Recovery System (PRS). Within the PRS, partially sintered powder was blasted away from the parts using loose partially-sintered powder of that build. Special care was taken to ensure that

all partially sintered powder was removed from the build plate and parts, as well as broken up sufficiently.

The volume of powder removed from the PRS process was then added to the volume of unsintered powder, including the powder left in the hoppers, that was vacuumed from the chamber and the two were manually mixed for approximately 15 minutes. Special care was taken to ensure that the powder from the two sources of recycling were thoroughly mixed. Thereafter, the mixed powder was passed through the sieve, with a 120 mesh size, to remove any large particles (>125 µm) and achieve further mixing. This powder was transferred back into the hoppers in the build chamber and a small portion, approximately 30 g, was removed from the top of the hopper in a clean plastic vial for analysis. The hoppers were then placed back into the chamber for the next build. The plastic vial of powder was sealed and placed in a desiccator to minimize the potential for atmospheric contamination during storage and prior to analysis.

2.2.3 *Chemical Analysis*

Chemical analysis was performed on the powder samples obtained from each build to characterize the changes in elemental concentration with reuse. X-Ray Fluorescence (XRF) was performed using a Bruker M4 Tornado to estimate the metallic component concentrations of the powder, including Ti, Al, V, Fe, and Y. This method has sufficient precision to be used for quantifying trends between builds. A total of 10 scans were performed per powder sample, with each scan performed at 50 kV and 600 uA, with a scan time of 180 s. The measures of each element were compared with the acceptable ranges or maximum permissible weight percent of each element in AM of Ti6Al4V as reported in ASTM F2924. Inert Gas Fusion (IGF) was used for quantitative analysis of the concentration of small elemental contaminants in the powder from each build cycle,

including O, N, and H. The IGF analysis was performed using a LECO Model 836 and on three separate 0.1 g samples obtained from the powder of each build.

2.2.4 *Powder Size and Morphology*

Light Scattering Powder Analysis (LSPA; Horiba Partica LA950-V2) was used to quantify the particle size distribution of powder for all the builds according to the standard operating procedures of the instrument. Three measurements were performed with the powder for each build. Scanning Electron Microscopy (SEM; JEOL 6100) was also used to examine the powder morphology and particle size distribution. Results from SEM analysis included an assessment of powder damage, as well as estimates of the particle size distribution, to compare with results obtained from the LSPA. To perform this examination, samples of the powder of each build were distributed onto conductive carbon tape. The sample preparation was performed gently to avoid accidental removal of small particles that were bonded onto the surface of larger particles. Images were obtained at 100X magnification and analyzed using a commercial software (NIH ImageJ, Bethesda, MD, USA).

2.2.5 *Part Microstructural Analysis*

The staircase and pyramid parts were used to investigate the importance of powder reuse on the microstructure of the printed Ti6Al4V as well as any spatial variations. These two different parts provide a means to assess the metal microstructure. Two build orientations of the staircase were chosen, including horizontal and vertical orientations. The difference in height-dependent volume to surface area ratios of the horizontal and vertical staircase (Figure 2.1b) provided a means for studying the effect of geometry and build height on microstructure. Note that the differences in volume and shape influence the thermal mass of the parts within the build plane. To eliminate any

variation caused from their locations on the build plate, the staircase and pyramid samples were built in the same locations every build.

The samples were cross sectioned and then mounted for the microstructural analysis. The horizontal staircase was cross sectioned in half along the 20 mm axis. The pyramid was cross sectioned through the central axis. The samples were mounted in a conductive graphite-based powder with a Bueher Pneumet I hot mounting press. The exposed surfaces of the mounts included the cross sectioned surface of the pyramid, the cross section of the horizontal staircase and the flat free surface of each vertical staircase. In total, there were 4 mounted surfaces for each build. After mounting, each sample was polished incrementally using SiC paper with increasing mesh numbers of #120, 240, 400, 600, to #800. The remaining fine polishing was performed with felt pads and DiaLube diamond suspensions of 6-micron. A final attack polish was performed to achieve a mirror finish using 100 ml of 0.05 µm diamond, 5 ml ammonium hydroxide, and 5-10 drops of hydrogen peroxide. Before each fine polishing step and after final polishing with the attack polish the sample was ultrasonically cleaned with Deionized (DI) water. The samples were then etched by immersion with Kroll's Reagent (2% HF, 6% HNO_3, and 92% water) for 15 seconds. Two of the evaluated surfaces are reported here over the multiple build cycles including the cross section of the pyramid and the free surface of the horizontal staircase.

After etching, the prepared surfaces were examined via Optical Microscopy (OM) and Scanning Electron Microscopy (SEM). They were examined in three primary locations, including at the bottom (closes to the build plate), the middle, and near top of each sample. For the pyramid sample, the XZ surface was investigated, with the locations outlined in Figure 2.1b. For the horizontal staircase sample, the YZ surface was investigated, and at the locations shown in Figure 2.1c. The bottom location is on the center axis and 2 mm from the base. The top location is on the

center axis and 22 mm vertically from the base. The middle location is approximately 10 mm from the base.

The microstructure of Ti6Al4V consists of α and β phases. The metal printed by EBM originally solidifies into columnar β grains that grow along the build direction (Figure 2.2a). As the printed parts cool, the β grains boundaries act as nucleation sites for α grains and the initial β within the grains transforms into α/β lamellar structures. This process promotes the development of β ribs surrounded by a continuous α phase [48]. Characterizing the grain structure of the microstructure resulting from the EBM process involves measuring the prior β grain widths and the α lath thicknesses. The line intercept method can be used to characterize the grain dimensions by drawing parallel lines perpendicular to the columnar grains according to ASTM E112. Here, the OM images were used to measure prior β grain widths. At each location of interest three OM images were taken to construct a window of evaluation of 600 μm x 200 μm as evident in Figure 2.2b. In each image, five parallel lines were drawn perpendicular to the columnar grain axis (and perpendicular to the build direction). Using the line intercept method, each prior β grain boundary that intersected these lines was counted as shown in Figure 2.2b. Note that only one line is shown in this figure for clarity. The prior beta grain size measurement at each location was obtained from the average of measurements obtained from the three images.

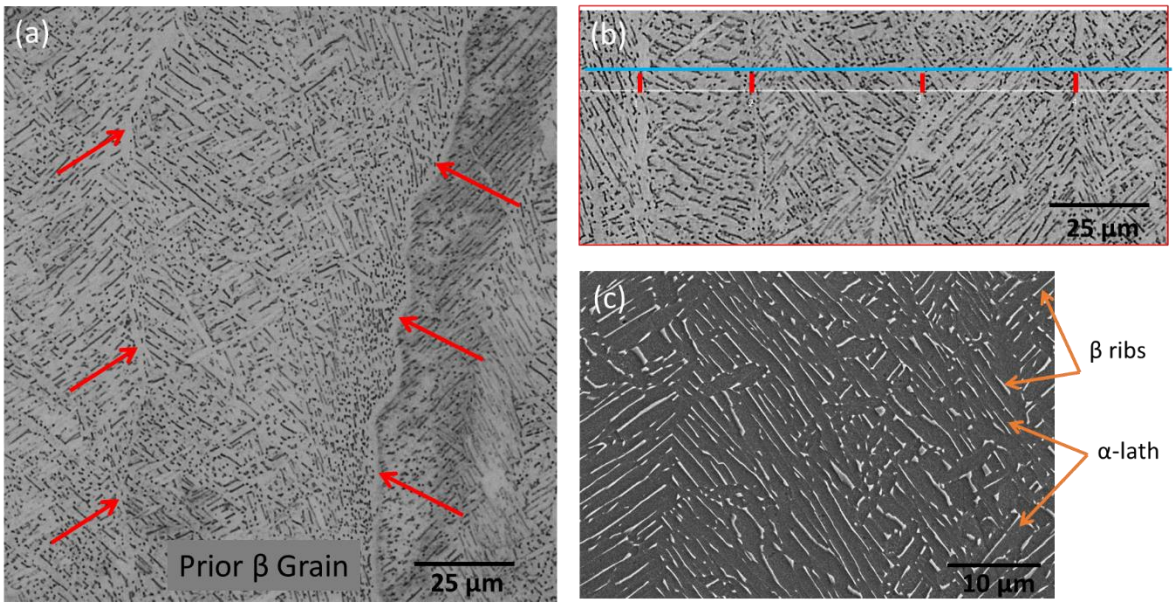

Figure 2.2. Micrograph of the "as-built" microstructure. A) prior β grains with boundaries outlined with red arrows. **(b)** The line intercept method employed to determine the prior β grain columnar width. **(c)** Micrograph of as-built microstructure with highlighted β ribs and α laths.

The α lath thickness was measured using images obtained from the SEM analysis. An example of α laths and β ribs in a micrograph of the EBM of Ti6Al4V are shown in Figure 2.2c. Three SEM images were taken at each location of interest to achieve a window of evaluation with area of 45 µm x 30 µm. The α lath thickness is defined as the shortest distance between two adjacent parallel β ribs. Image processing was performed using a commercial software (Adobe Photoshop, San Jose, CA, USA) to measure the α lath thickness at each location of interest according to Searles et al. [49]. First, thresholding of the image grayscale is performed. Then, parallel lines are drawn at a specified angle that intersect the β ribs. The length of each of these line segments are measured and the average line length was recorded. The process was repeated

by rotating the parallel lines by 30°. The process is repeated until the lines have been rotated a total of 360°. The α lath thickness is calculated by using the average line length, λ, according to:.

$$\alpha\ lath\ thickness = \frac{1}{(1.5*(\frac{1}{\lambda}))} \quad (2.1)$$

To achieve a higher statistical accuracy of measurement, the average α lath thickness was measured from three images at each location.

The parts obtained from each build were investigated using the aforementioned OM and SEM imaging process to evaluate the microstructure as a function of build cycles and powder reuse. Due to the time required for conducting the microstructural analysis, not every build cycle was evaluated. Rather, the builds were evaluated from the first (build 1: b1), to the last (build 30: b30) in increments of approximately every 3rd build.

2.3 RESULTS

2.3.1 *Powder Size and Morphology*

A micrograph of the virgin powder from optical microscopy is shown in Figure 2.3a. Highlighted in this micrograph are the large range of particle sizes, the satellite particles adhering to the larger particles and an example of non-spherical particles. Micrographs of powder samples from each build were used to characterize the powder size distribution through an image analysis. Figure 2.3b shows the size distributions obtained from the micrographs from several builds including b1, b10, b20 and b30. There is a clear decrease in the number of small particles, as well as a narrowing of the distribution around the median to a more gaussian distribution.

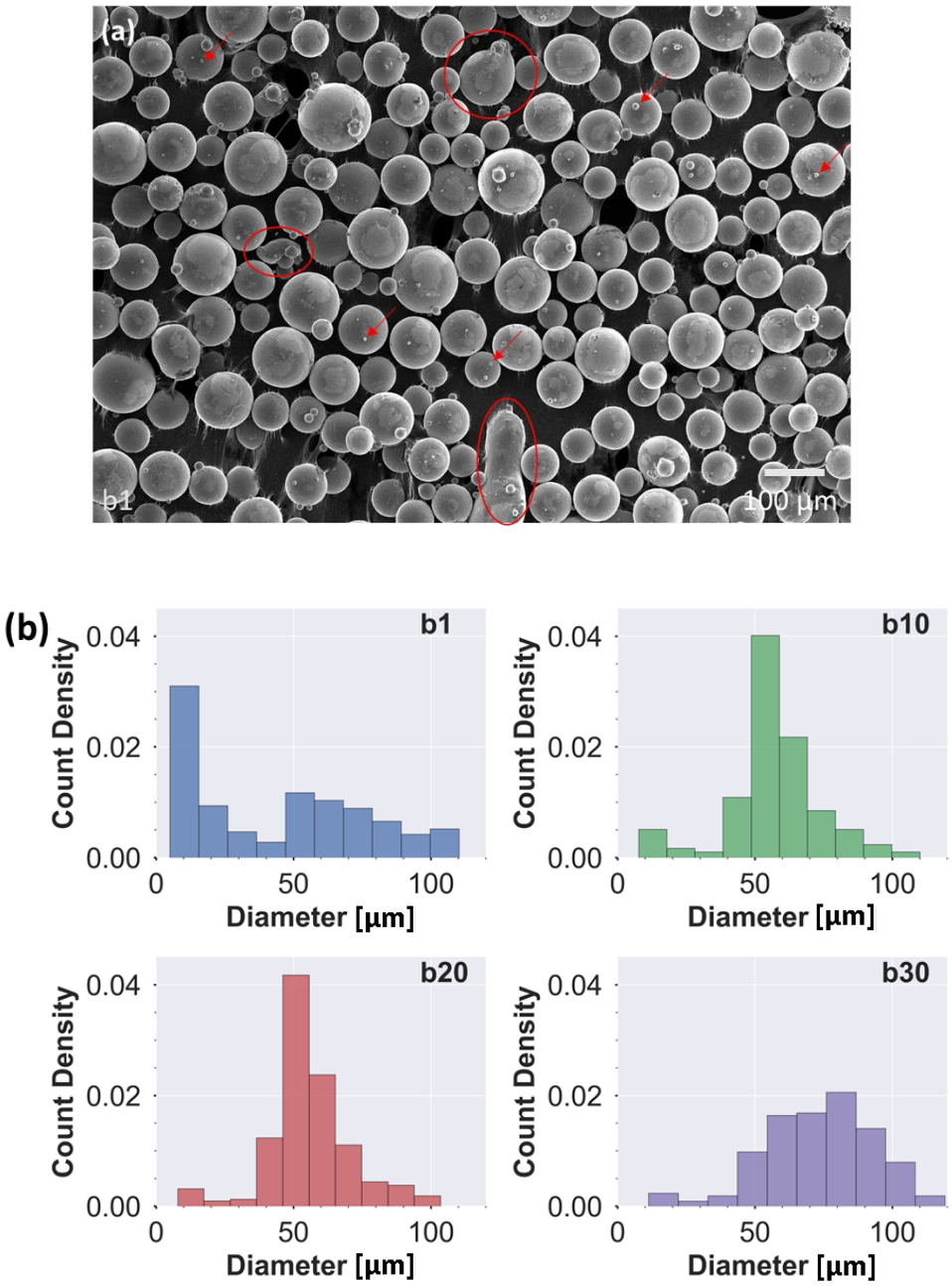

Figure 2.3. Powder characteristics. **(a)** Micrograph of virgin powder from build 1. Red arrows highlight selected small particles that exist in the virgin powder. Red circles highlight some of the irregular particles. **(b)** Powder size evolution from build 1 to build 30.

Measurements of the particle size distribution obtained from LSPA are shown in Figure 2.4. These results are presented in terms of the upper (D90) and lower tenth (D10) percentile as well as the median. Although the median particle size remained nearly constant with powder reuse, there is a minor decrease in D10 and a more substantial decrease in the D90 distribution as evident from the trends in upper and lower percentile distributions.

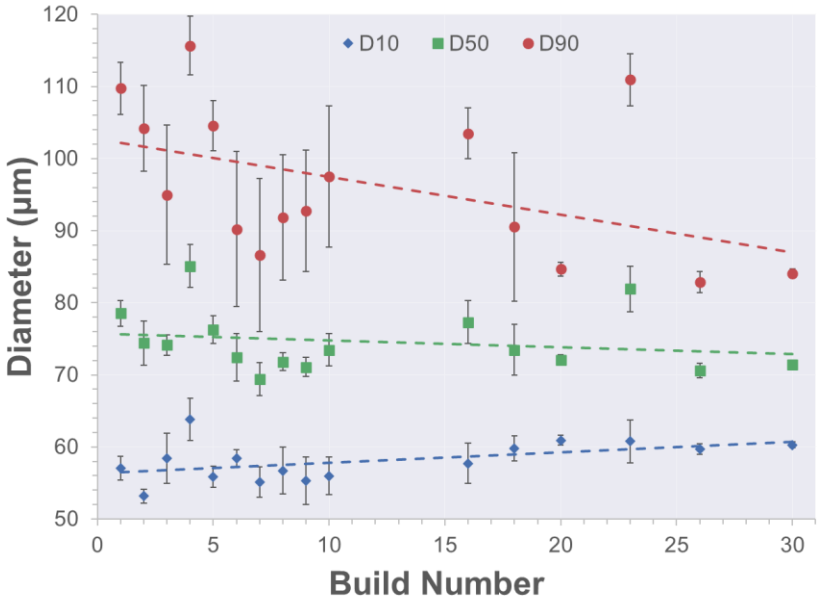

Figure 2.4. Powder size distribution with powder reuse across the 30 builds. The 10th, 50th, and 90th percentile are plotted as determined by LSPA.

In addition to the changes in size of the particles, the surface texture and overall morphology changed with reuse. A comparison of powder from b1 to b30 is shown in Figure 2.5. Specifically, representative images of particles from b1, b7, b10, b20 and b30 are shown in Figures 2.5a through 2.5e, respectively. The microscopic analysis showed that there were distinct changes within only four reuse cycles with regards to the virgin powder. Most notable were the

reduction in the number of small particles (e.g., Fig. 2.5a), as well as morphological changes. The particle surfaces show evidence of surface deformation, including dimples (e.g., Fig. 2.5b) that evolved in size with greater number of reuse cycles (Fig. 2.5c-e).

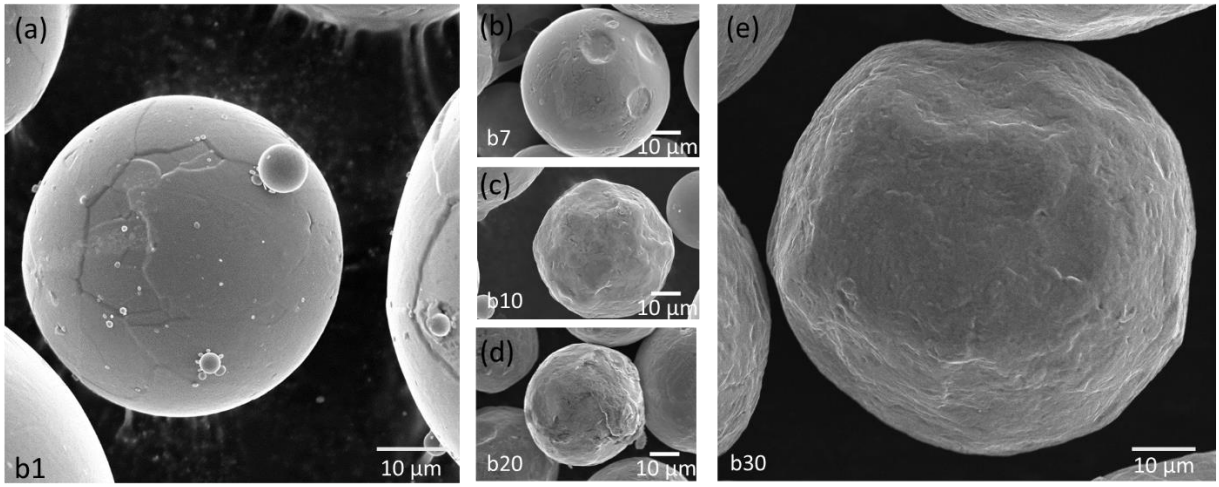

Figure 2.5. Progression of powder size and morphology through the reuse process. **(a)** In virgin powder (b1), particle surfaces are relatively smooth and they have high sphericity. There is numerous tiny particles that agglomerate or adhere to the surface of larger particles. Representative views of powder in b7, b10, and b20 in **(b)-(d),** respectively, show the progression of particle surface damage and the absence of tiny particles. In b30 **(e)**, the particles are irregular with some exhibiting major deformation and damage.

In addition to the evolving degree of deformation, there were several irregular particles noted with high aspect ratio, with a general increase in number with powder reuse. Examples of particles in this category are presented in Figure 2.6 and include fractured particles (Fig. 2.6a), fused particles (Fig. 2.6b) and what appears to be recast particles (Fig. 2.6c).

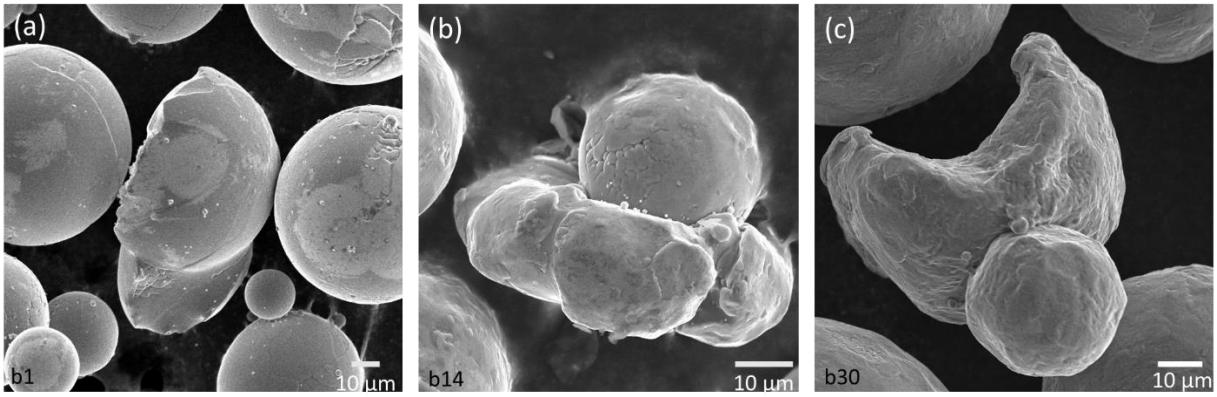

Figure 2.6. Examples of damaged particles in powder of b1, b14, and b30. Selected examples of **(a)** fractured, **(b)** agglomerated/fused, and **(c)** melted/irregular particles are shown, respectively. In general, damaged particle of these types were observed in the powder of all builds evaluated by SEM.

2.3.2 *Chemical Analysis*

Regarding the analysis of chemical composition, Figure 2.7a presents the weight percent distribution of metallic elements in the powders as a function of the build and recycling process. As evident in this figure, there is negligible change in weight percent for V, and a small (0.03%) increase in Al over the 30 build cycles. The values for Al and V are appropriate for examining trends in the composition, but not necessarily for obtaining absolute composition.

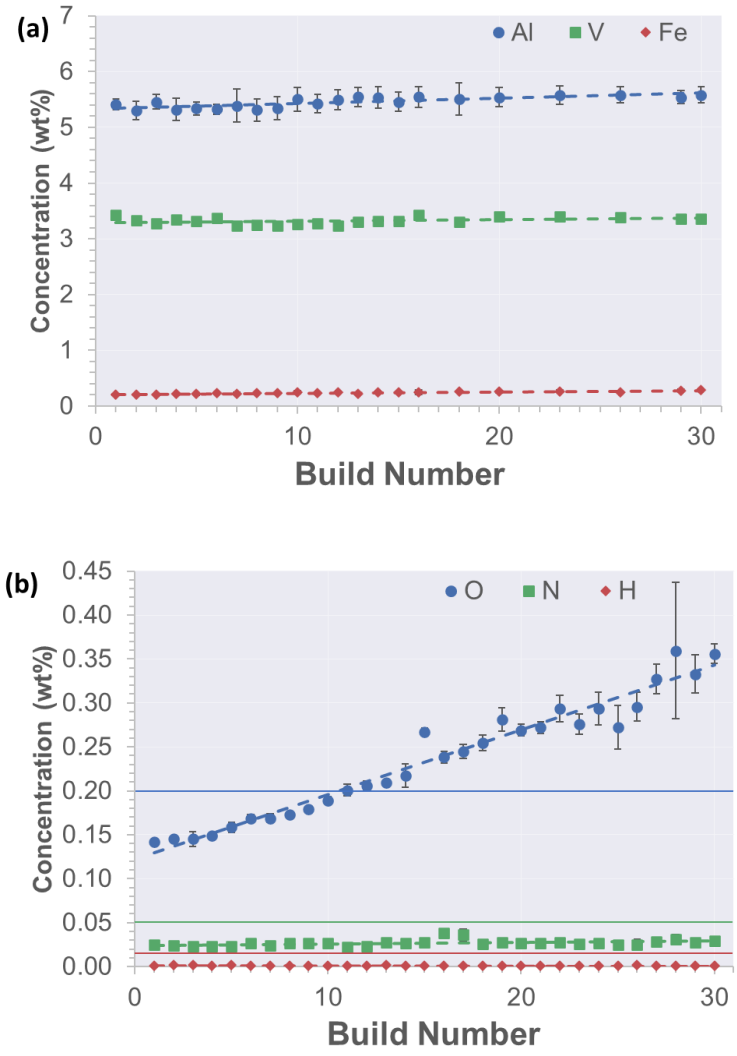

Figure 2.7. Chemical composition of the powder over the build history. **(a)** Al, V, and Fe from XRF shown to have a nearly constant trend. The Fe remains below the 0.30 wt% limit. **(b)** O, N, and H from IGF. Concentration limits are represented with dashed lines and colors coordinated with the elements. The N and H content remain constant whereas the O content increase with reuse and exceeds the 0.20 wt% limit by b11.

Average measures of the major elements are listed in Table 2.1 for builds b1, b10, b20, and b30. As apparent from the table, there is an increase in Fe from 0.21 to 0.29 wt%. Yttrium

was also included in the scan but does not appear in the Figure 2.7a as it was identified in only a few of the builds and the wt% was on the order of 0.001 or less. That level of Y is far below the limit specified by ASTM F2924 of 0.005 wt%.

Table 2.1. Concentrations of key elements (ordered by Z number) in the powder for b1, b10, b20, and b30.

Build	H (wt%)	N (wt%)	O (wt%)	Al (wt%)	V (wt%)	Fe (wt%)
1 (virgin)	0.0014	0.024	0.142	5.41	3.43	0.21
10	0.0010	0.026	0.189	5.50	3.26	0.25
20	0.0012	0.027	0.269	5.54	3.40	0.26
30	0.0009	0.030	0.356	5.58	3.36	0.29

Contrary to the limitations of XRF, the IGF technique provides accurate quantitative data for absolute composition and are shown in Figure 2.7b. The O and N dissolve interstitially into the Ti lattice and form oxides and nitrides upon reaching adequate weight percent, which can influence various aspects of the mechanical behavior. In addition to the experimental measures of these elements, the concentration limits for Ti6Al4V according to ASTM F2924 are also shown. The measured concentration of N remains relatively constant across all builds at 0.014 wt%, which is well below the limit of 0.05 wt%. Similarly, the H concentration remained nearly constant with powder reuse around 0.0012 wt%, which is well below the 0.015 wt% limit. In contrast to the other contaminants, the level of O underwent a linear increase in wt% with build number as evident in Figure 2.7b. The concentration exceeds 0.20 wt% by b11, which is defined

is defined as the limit for Grade 5 Ti6Al4V by ASTM F2924). With an average increase of about 0.007 wt% per build, the levels of O in b30 reached an average of 0.356 wt%, which is 1.75 times greater than the limit of O allowed within this grade of titanium alloy.

2.3.3 *Microstructure*

The first phase of the microstructural analysis addressed prior β grain width, and results are shown in Figure 2.8. For the pyramid geometry Fig. 2.8a, the prior β grain width increases significantly with increasing build height along the center axis from the base to the top of the specimens. This trend was observed regardless of build number as evident in the figure. There is no apparent increase in prior β grain width with increasing build number and increasing powder use. For the staircase geometry (Fig. 2.8b), the prior β width dimensions showed a much tighter size distribution with comparatively lower height and overall lower widths when compared to the prior β dimensions of the pyramid. For all builds, the staircase had a prior β width as much as 47% smaller than the pyramid at near equivalent height (10.5 vs 10 mm), with an average 30% lower width.

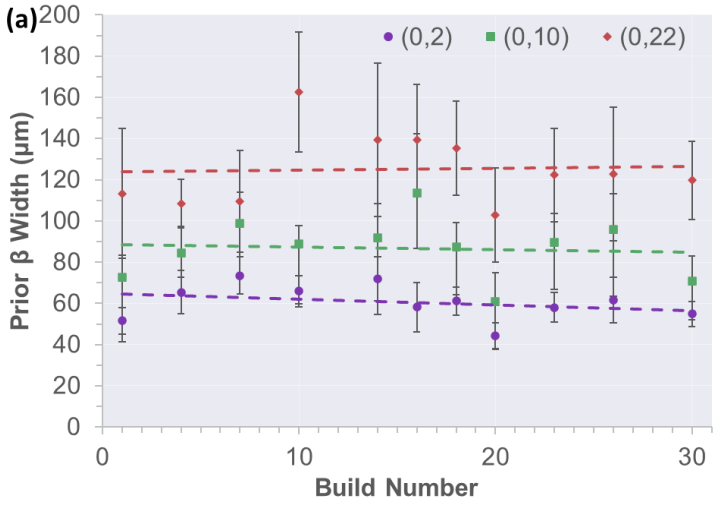

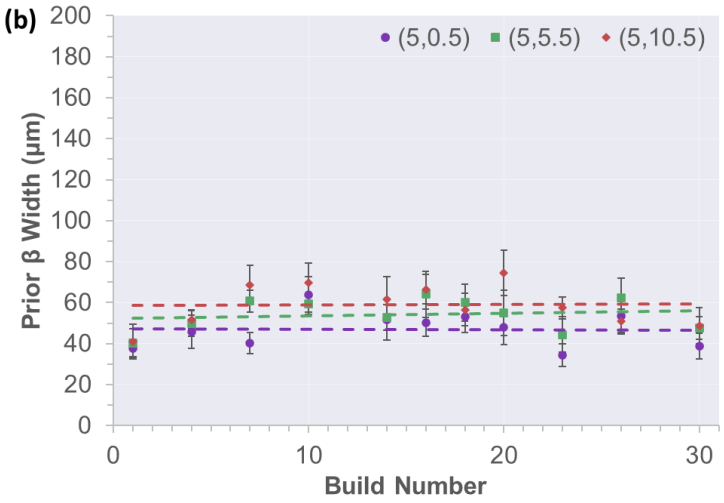

Figure 2.8. Prior β grain dimensions for the pyramid **(a)** and staircase **(b).**

Measurements for the α-lath thickness were obtained from SEM images and representative images for the microstructure of b1 and b30 of the pyramids and staircase are shown in Figure 2.9 and Figure 2.10, respectively.

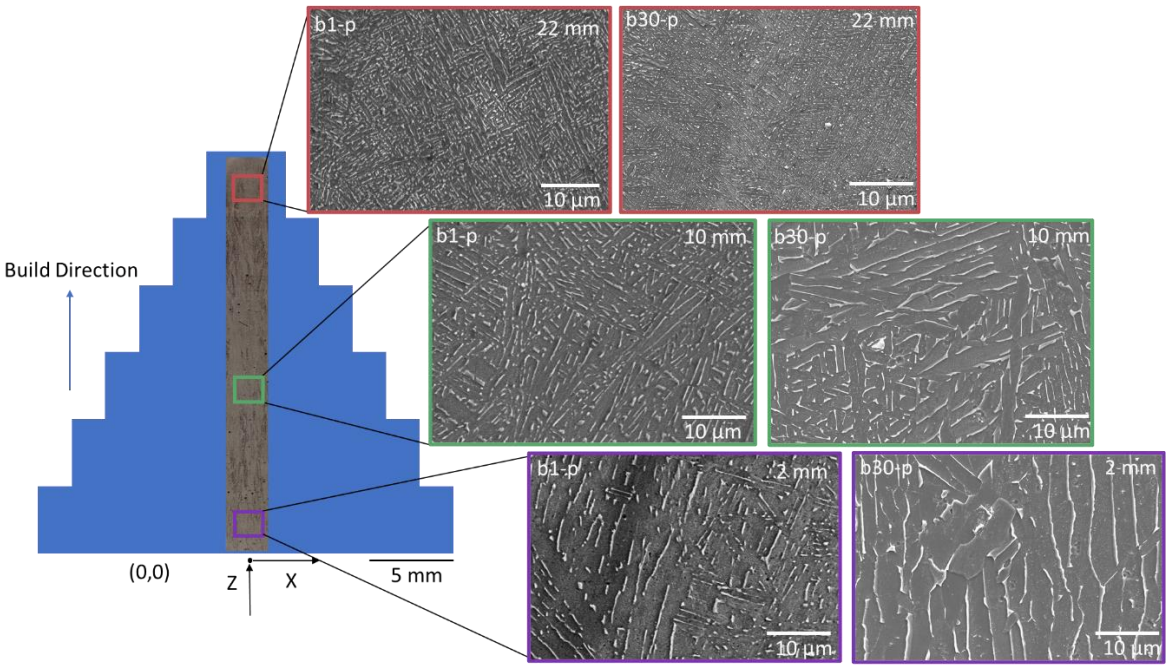

Figure 2.9. Microstructure of the pyramidal specimen from bottom to the top at distances of 2, 10, and 22 mm from the base of the part. At each height micrographs are shown from b1 (left) and b30 (right). Note the trend toward a tighter basket-weave pattern from the base to the top of the pyramid.

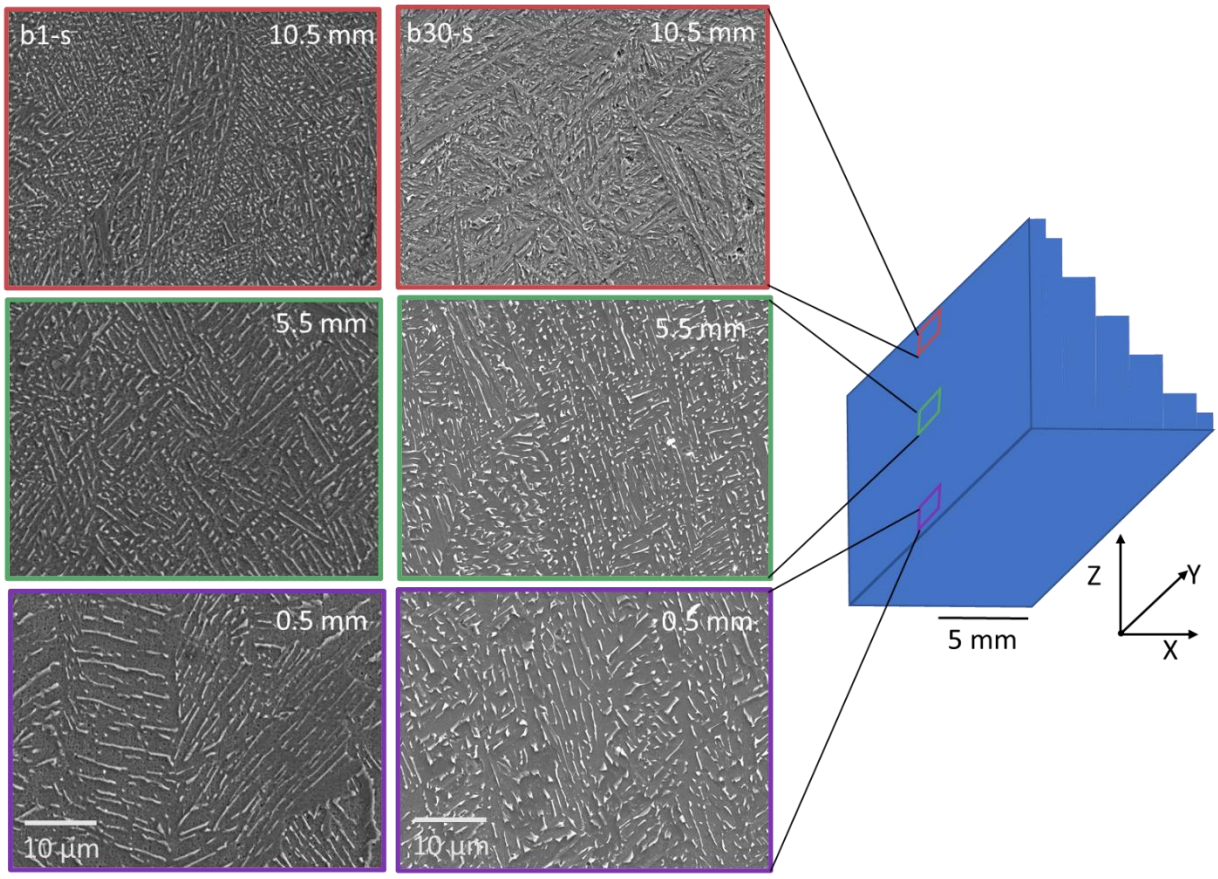

Figure 2.10. Microstructure of the staircase specimen from bottom to top at distances of 0.5, 5.5, and 10.5 mm from the base of the part. At each height micrographs are shown from b1 (left) and b30 (right). Note the trend toward a tighter basket-weave pattern from the base to the top of the staircase.

As evident from these figures, there is a distinct change in the microstructure with build height for both build geometries. These changes were quantified in terms of the α volume fraction and the α-lath thickness and as function of the build number (Figure 2.11). Specifically, the α volume fraction and the α-lath thickness for the pyramid is presented in Figures 2.11a and 2.11b, respectively, and for the staircase in 2.11c and 2.11d, respectively. In general, the α characteristics appear to exhibit a dependence on build height. In the pyramid, the α volume fraction decreases with increasing build height for all build numbers except for b20 (Fig. 2.11a). The α-lath thickness also decreases with increasing distance from the build plate, and exhibits broadening of this spatial feature with increasing degree of reuse of the powder (Fig. 2.11b). For the staircase, the volume fraction of the α phase appears to be less spatially dependent (Fig. 2.11c) and no trend is apparent with reuse. Figure 2.11d shows the α lath thickness measurements of the free surface of the staircase specimens as a function of location and build number.

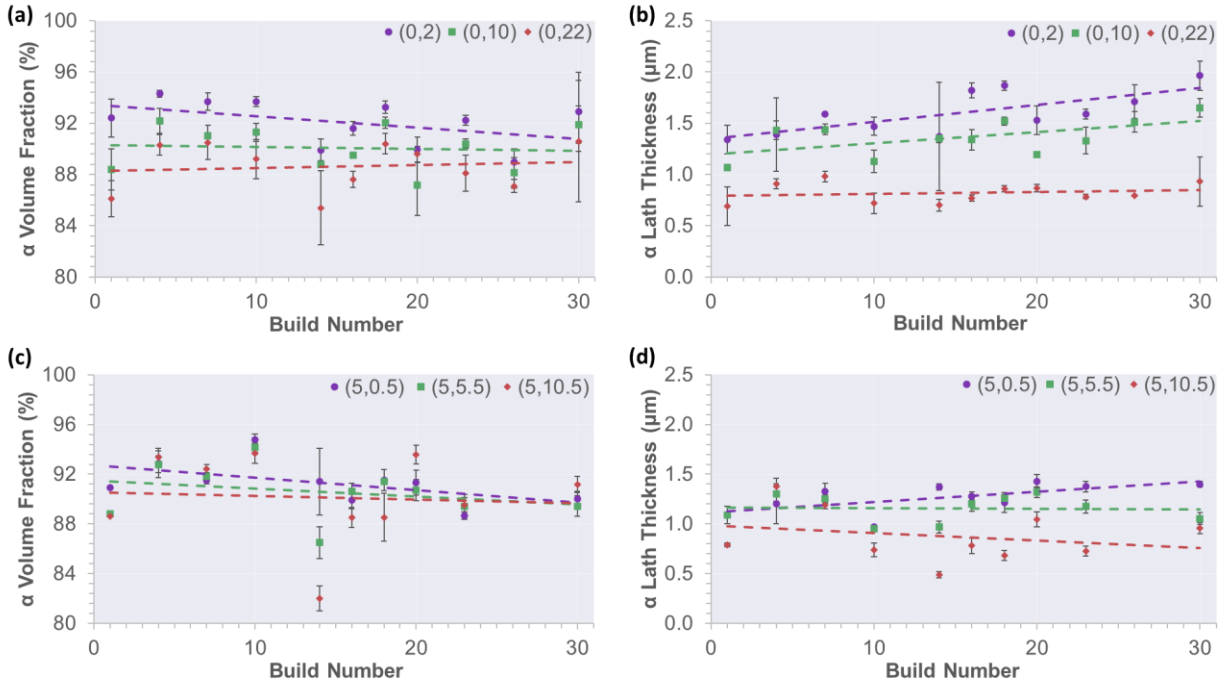

Figure 2.11. Microstructural parameters of the α content. **(a)** α volume fraction percentage for the pyramid specimen. **(b)** α lath thickness in micrometers for the pyramid specimen. **(c)** and **(d)** are the same as **(a)** and **(b)**, respectively, but for the staircase specimen.

There appears to be a broadening of the distribution with powder reuse that is similar for the pyramid. In comparing responses for the two geometries, the primary difference in microstructure between the pyramids and staircases is the broader spread of alpha volume and alpha lath thickness in the pyramid, along with the increase in alpha lath thickness with powder reuse. Regardless of location in the built parts (Table 2.2), there is only a trend in the alpha lath thickness with powder reuse, as opposed to the alpha/beta volume fractions and prior beta width, which varied inconsistently through the study.

Table 2.2. Key microstructural features for the pyramid and staircase parts. The values are averages for all heights in the given part.

	Pyramid				Staircase			
Build	**α V_f (%)**	**β V_f (%)**	**α lath thickness (µm)**	**prior β grain width (µm)**	**α V_f (%)**	**β V_f (%)**	**α lath thickness (µm)**	**prior β grain width (µm)**
1	88.97	11.03	1.03	79	89.43	10.57	0.99	40
10	91.40	8.60	1.11	106	94.23	5.77	0.89	64
20	88.90	11.10	1.20	69	91.88	8.12	1.27	59
30	91.79	8.21	1.52	82	90.20	9.80	1.14	45

2.4 DISCUSSION

As a consequence of the cost of powders in metal AM, and particularly in applications of Grade 5 Ti6Al4V, the topic of powder reuse could be considered more important than it is for other feedstock materials. The potential variability in part properties that arises with powder reuse is an equally important concern. It is perhaps the most important to address before metal AM can be adopted for mission-critical applications. Therefore, while a thorough understanding of all parameters contributing to the quality and reliability of metal produced in AM will be needed, addressing reuse is an equally high priority. Consequently, the present study addressed changes in the powder and the built metal with powder reuse.

2.4.1 *Powder Size and Morphology*

Results showed that nearly all aspects of the powder and printed metal qualities evaluated were dependent on the extent of powder reuse. According to the SEM micrographs and image analysis,

the virgin powder exhibited a bimodal distribution in particle size. The bimodality comes from the large number of very small diameter particles along with a relatively wide distribution of the measured diameter.

There was a reduction in the number of small particles with reuse (Fig. 4). Small particles could be consumed during the building process, fused onto the surface of larger particles or lost during the powder recovery process and sieving. Slotwinski et al. [50] showed similar results, namely an increase in particle sizes with increasing powder reuse. They attributed the change in size distribution to the consolidation and loss of the small particles. The study by Grainger [28] concerning powder reuse in selective laser melting reported similar results. Their powder started with many small particles that disappeared with powder recycling. Consumption/loss of the small particles can explain the increase in D10, but does not appear related to the decrease in the D90. Reduction of the 90^{th} percentile most likely comes from the use of a 120 mesh sieve that eventually removes particles and agglomerates above 125 μm.

Flowability is one of the key properties of powder used for powder bed fusion. It dictates how the powder will flow by the rake and will influence distribution of powder within that build layer. Poor flowability may result in improper spreading in the powder and directly cause porosity. Through the reuse process the powder had an improvement in flowability (Figure 2.7) that appeared to plateau, which is consistent with other powder reuse studies [19]. The largest reduction in the flowability may come immediately after the first use of virgin powder [27]. Small particles (<D10) are removed almost immediately during the reuse of powder and this may explain the initial improvement in flowability. The other possibility is that deformation of the powder causes a particle morphology that is different from the free-flowing spherical shape.

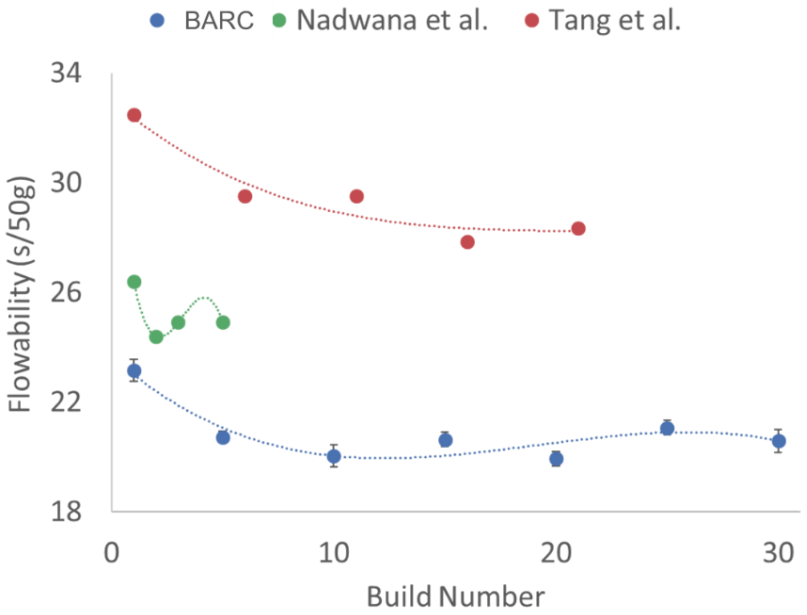

Figure 2.12. Flowability measurements for virgin powder (b1) and every 5th build (b5, b10,…,b30). This is compared to data adapted from other powder reuse studies [19,27].

Previous studies on powder reuse have also observed progressive surface damage to the particles with reuse [19]. Most of this damage is expected to result from the deformation involved in the mechanical aspects of powder recovery [19], including the bombardment of the powder against itself and parts in the PRS, along with other aspects of general powder handling (pouring, scooping, extraction, etc). Changes in particle shape due to imbedded and fused particles have also been previously noted [23]. Nevertheless, the recycling process involved in selective laser melting is expected to be less aggressive than that in the EBM process, particularly due to the need for dislodging partially sintered powder in the ARCAM PRS.

The bimodal distribution of the virgin powder could be beneficial to the apparent “bulk” density due to the ability for small particles to fill voids between the larger particles. The tap and apparent density of the particles, as outlined in ASTM B243, were not measured in the present

study. An appreciable increase in packing density for a binary distribution of particles requires the ratio of diameters between particles to be >5 (ideally >10) and a volumetric percent of small particles of 50-80 vol% [51]. Nevertheless, based on the image analysis distribution of particles in b1, the diameter ratio of particles is >6 and there is only 0.3 vol% of small particles, implying that the increase in apparent density would be minimal. The more normal and less broad distribution of the reused powder could result in lower packing density of the powder bed [52]. In a study that compared powders with two different PSDs, it was found that the powder with the tighter uniform distribution had lower packing density and resulted in higher porosity in built parts [53]. In this regard, the powder reuse could be considered detrimental as the PSD transitions from a broad binary PSD to the uniform distribution, which could be a concern for defect generation and resulting damage tolerance of built parts.

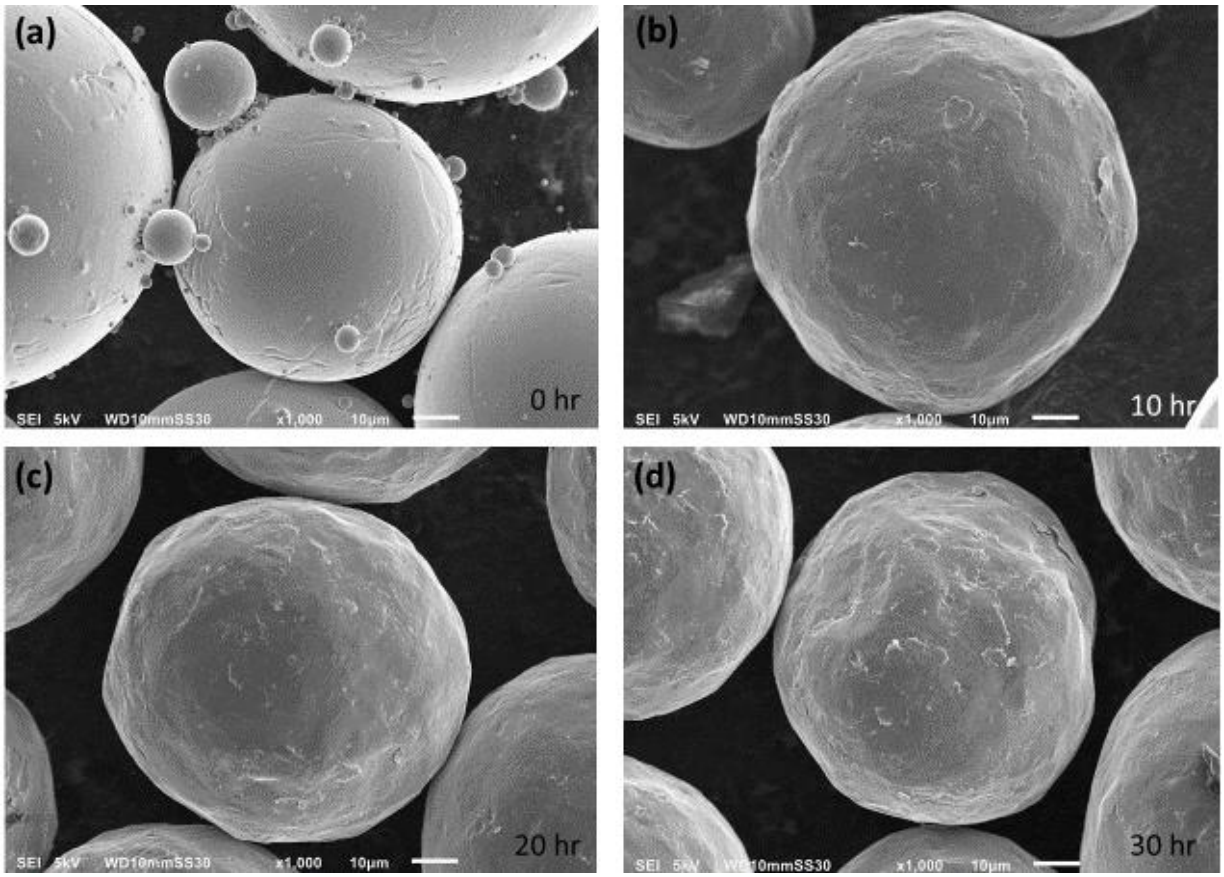

Figure 2.13. Micrographs of powder after running in the powder recovery system (PRS) for 0, 10, 20, and 30 hr, (a)-(d), respectively.

Changes in the surface morphology of the particles became increasingly apparent with number of build cycles and powder reuse. Most notable was the accumulation of surface deformation of the particles with increasing build cycles. There was also substantial damage apparent in some isolated particles of the reused powder (Figure 2.6) including cracking, fused particles and recast particles. Although evidence of this damage was noted after only a few build cycles, it increased with the extent of reuse. The powder underwent a transition from smooth and spherical to rough and irregularly shaped with an overall decrease in sphericity. The powder recovery process in EBM involves air assisted blasting of the partially sintered powder with loose

powder and it appears to be the most likely cause of the aforementioned damage. It can also explain the partially embedded small particles into the surface of the larger ones. A control condition involving only powder recovery (PRS conditioning treatment only) was also conducted. Specifically, a volume of powder was cycled through the PRS system for 30 hours continuously without builds. This powder, regarded as t30, had significantly lower circularity than even b30 as shown in Figure 2.14.

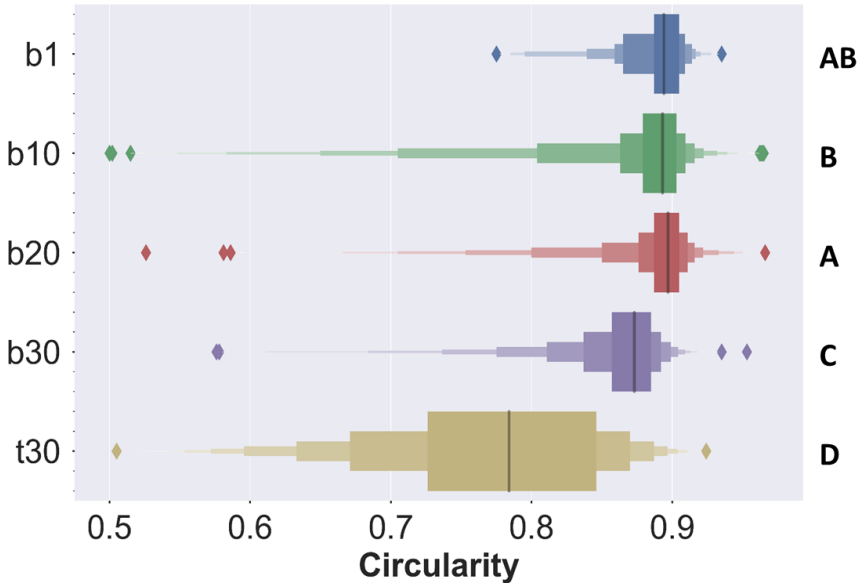

Figure 2.14. Boxplots of powder circularity for builds b1, 10, 20, and 30, as well as for powder that was cycled through the PRS for 30 hours (t30). The bolded letters to the right indicate the groups which have no significant difference of $p<0.05$ (e.g. b1 is labelled 'AB' and as such is not significantly different from b10 or b20 which are labelled as 'B' and 'A', respectively).

2.4.2 *Chemical Analysis*

Regarding results of the chemical analysis, the concentrations of Al and V remained below their respective limits for Ti6Al4V as specified in ASTM F2924 [34]. It is important to note that the XRF analysis provides semi-quantitative results for the metallic elements in the powder. As Al is a relatively light element, the X-Rays emitted will be relatively weak and may be absorbed or not have enough intensity to be accurately detected, even under vacuum. Since V is next to Ti in the periodic table, it has only slightly higher Kα. As such, there will be some overlap in the acquired spectrum, which requires deconvolution of the peaks and may not be completely accurate. Moreover, Ti is a significantly higher percentage of the composition and can diminish the response of V. On the other hand, Fe is a relatively heavy element with strong Kα, which should help to provide strong signal and accurate estimate of concentration. As highlighted earlier, the concentration of Fe and Y were present in the powder as metallic contaminants, but below their allowable tolerance level.

Light element contaminants including O, N, and H are typically more of a concern for the mechanical properties of Ti alloys than the heavy elements [54]; contamination by O, N or H can cause embrittlement, even in small concentrations [55]. The limits outlined in ASTM F2924 for these elements are 0.20, 0.05, and 0.015 wt%, respectively. The level of H was approximately 0.0012 wt% and nearly constant over the 30 build cycles, which is well below the concentration limit. Similarly, the level of N stayed almost constant across the subsequent builds with only a small increase from 0.025 to 0.030 wt%. Virgin powder (b1) was found to have 0.024 wt% of N and this is slightly more than the value quoted with the initial powder of 0.02 wt%. Most alarming was the change in O; the concentration increased with powder recycling, starting at 0.14 wt% and increasing to 0.356 wt % by b30. In fact, the O concentration exceeded the limit of 0.20 wt% by

b11. The rise in O concentration of the powder is concerning since the limit is defined to prevent embrittlement and diminished mechanical performance due to contamination. Although the strength may increase as a function of the oxygen, the ductility will decrease. Grainger [28] reported O and N concentrations in the recyclability study in laser powder bed AM of Ti6Al4V . They also reported linear increases in O and N with number of builds (starting around 0.09 and 0.01 wt%, respectively) for their Grade 23 powder. However, after 30 builds their powder never exceeded the limits defined for Grade 5. The lower values reported in the study of Grainger could be due to the lower starting oxygen content and their process being conducted within an argon atmosphere for most steps, including the extraction the powder for recycling into the next build. In the present study performed with EBM, the powder was exposed to ambient atmosphere during build extraction, and involved transfer to the PRS, mixing, and sieving. This exposure is a source of moisture which could results in oxidation for the next build [19,27]. Mechanical deformation from the PRS may potentially accelerate the process of oxidation through production of new surfaces that are not oxidized.

2.4.3 *Microstructure*

The microstructure resulting from EBM of the Ti6Al4V was evaluated in the specimens with pyramid and staircase geometry (Figure 2.1a). Many factors could contribute to variations in the microstructure of these printed parts, independent of powder reuse. Possible contributions include the gradients in temperature, thermal mass, surface to volume ratio, and cooling rates with distance from the build plate. Changes with chemistry as a result of powder-reuse are also of concern.

The prior β grain sizes of Ti6Al4V are primarily driven by the time above the β transus temperature (≈1000C) [56]; longer time results in larger prior β grain sizes. As build height increases in the pyramid the melt experiences a longer time above the β transus due to the

accumulation of thermal mass from the layers of deposited build material, thereby causing an increase in prior β width along the center axis of the pyramid. However, the free surface of the staircase did not undergo a change of prior β dimensions with increasing build height, as expected, because the free surface experiences similar time above the β transus temperature throughout the build height. Considering powder reuse, there is no trend in prior β grain size as build number increases in both the free surface (staircase) and center axis (pyramid). Increased oxygen can increase the β transus temperature for Ti6Al4V [57], which could result in less time above the transus temperature. However, the range of oxygen accumulated during the reuse process does not appear to be sufficient to influence the prior β grain width.

Cooling rates play a significant role in determining the α lath thickness; faster cooling rates result in smaller α lath thickness [58]. At the free surface of the staircase there was no trend with build height, as expected, due to the similar cooling rates throughout the build height. In contrast, the center axis of the pyramid experiences an increase in cooling rate with increasing distance from the build plate due to the reduction in volume to surface area ratio. Collectively, this results in decreasing α lath thickness with increasing build height. In both the free surface of the staircase and the center axis of the pyramid, recycling powder does have an effect on the α lath thickness. Nevertheless, the local cooling rates driven by the boundary condition and the thermal mass appear to be more important. For regions of high thermal mass or large volume/surface area ratio, the α lath thickness increases with powder reuse. Conversely, in regions of low thermal mass or low volume/surface area ratio, the α lath thickness decreases.

There was a change in powder chemistry with increasing powder reuse (Fig. 7(b)) that could contribute to the α lath thickness. Oxygen is an α stabilizer. There is an increase in the α lath thickness with powder reuse (and build number) resulting from the increasing oxygen

concentration. Interestingly, however, that there was no apparent trend of α volume with powder reuse. Increasing oxygen concentration should result in increased α volume fraction [57], which is not apparent in the printed material. One possible reason for the lack of α volume increase is the dissolution of excess oxygen into the β phase [23].

According to the work of Tan et al. [59] on EBM, α lath thickness and prior β width increases with build height. However, there are limited reports that also consider the local effect of part geometry on microstructure in the EBM of Ti6Al4V. The results obtained for the α lath thickness and prior β width measurements in the present investigation are comparable to those previously reported [18,56], which showed a decrease in α lath thickness with build height. This trend could be attributed to the change in total layer area with steps of the pyramid. The smaller layer area of the higher steps of the pyramid results in a smaller amount of in-fill hatching on the build layer. According to Tan et al. [60], decreasing the extent of in-fill hatching results in smaller α lath thickness. The free surface does not exhibit a change in α lath thickness as a function of build height. The material at the free surfaces is influenced by the contour beam as compared to the hatching beam, which could be the causal factor for the unique trends. Nevertheless, this interpretation is admittedly speculative and further research is planned to address this issue in future studies.

2.5 CONCLUSIONS

Based on an experimental investigation of powder reuse in EBM of Grade 5 Ti6Al4V over a routine involving 30 consecutive builds, the following conclusions were made:

1) The particle size distribution evolved from a bimodal distribution in the virgin condition (b1) to a Gaussian distribution with powder reuse. In addition, the range in particle sizes decreased with increasing degree of powder reuse, which resulted from a decrease in the number of satellite and small particles (<<D10) as well as a decrease in the average diameter of the largest particles.

2) The concentration of major alloying elements (Al and V) and metallic contaminants (Fe and Y) were well below the limits defined by ASTM F294 for Grade 5 Ti6Al4V over the 30 builds. Furthermore, the concentration of H and N remained well below their respective limits.

3) The O contamination increased linearly with powder reuse, and more than doubled over the 30 build cycles. The concentration of O exceeded the limit of 0.2 wt% by b11.

4) One of the most marked changes in powder with reuse was the increase in surface deformation to the particles and physical damage. The particles changed shape from spherical to deformed with surface dimples and irregular shape. This aspect of the powder degradation appears to result from the mechanical aspects of the recycling and part extraction process. In addition, there was an increase in fractured particles, partially fused particles and recast particles with powder reuse.

5) The α lath thickness of the central axis of the pyramid decreased with increasing build height and increased slightly with powder reuse. This suggests that the cooling rate increases with increasing build height. Conversely, the prior β grain widths of the center axis increased with

build height, but not with powder reuse. This implies that the time above the β transus increased with increasing build height, but powder reuse does not affect the time above the β transus.

6) The α lath thickness of the free surface of the staircase did not exhibit dependence on build height or powder reuse. This implies that the cooling rates remained constant throughout the build height and recycled builds at the free surfaces. The prior β grain widths increased with build height but much lower than that in the pyramid, indicating the free surface condition experienced similar thermal history regardless of height.

Chapter 3. POWDER REUSE AND ITS CONTRIBUTIONS TO POROSITY IN ADDITIVELY MANUFACTURING OF TI6AL4V

3.1 SYNOPSIS

Powder reuse has become a central issue in the pursuit to industrialize metal Additive Manufacturing (AM). Furthermore, build porosity is a critical concern to component reliability and damage tolerance of the metal. However, the contributions of powder reuse to metal porosity have received very limited attention. In this study, the porosity resulting from Powder Bed Fusion-Electron Beam Melting (EBM) AM of Ti6Al4V was characterized over a series of 30 build cycles (consisting of ~ 480 hr cumulative build time) using X-ray Micro Computed Tomography (μCT). Investigated were the volume fraction of pores (i.e., the porosity), as well as the pore size, shape, and spatial distribution. The most prevalent pores identified were: i) those originating from the gas atomized powder, and ii) those caused by incomplete fusion of the melt pool. Although there was a minor reduction in the pore size distribution with powder reuse, the overall average volumetric porosity was 0.10±0.02% and there was no significant change with increasing reuse. An inverse relationship between pore diameter and sphericity was found, with large pores posing greater effective stress concentration. Whereas the greatest pore density was located at the transition between the contour and melt beams, approximately 0.5-1.0 mm adjacent to the surface of parts, the largest pores were located within the interior hatching region. Hence, despite progressive deformation of the particles and an increase in oxidation, there was no discernable change in metal porosity with powder reuse in EBM of Ti6Al4V.

3.2 INTRODUCTION

Additive manufacturing (AM) is an exciting area of research and advancements are taking place in feedstock, machines and processing for nearly all classes of materials. Based largely on industrial interest, the rate of advancement in metal AM appears to be outpacing that for the other material systems [4].

Metal AM processes are often differentiated in terms of the feedstock, manner of distributing or depositing the materials, and the consolidation technique [61]. Broadly speaking, the central issues are universal and involve the feedstock material, the processing parameters, the corresponding microstructure of built metal and its mechanical properties. Reviews on this topic convey that process-structure-property relationships are under development but are challenged by the large number of processing parameters [8,13]. For metal AM to be capable of consistent part performance, the development of robust process-structure-property relationships will be needed, as well as the appropriate qualification standards [62].

One of the fundamental concerns that pervades all metal AM processes is part porosity [6]. Pores cause stress concentrations that degrade the mechanical properties and reduce the reliability of AM parts [30]. As such, understanding the origins of porosity and how to minimize it are prerequisites to the use of AM for stress-critical components. Recent efforts have focused on understanding the mechanisms contributing to the generation of pores [37] and developing relationships between the formation of these pores and the process parameters, such as beam speed and power [31,33], as well as powder characteristics [34]. Yet, less seldom explored are the specifics regarding the pore size, shape, and spatial distributions.

Among the powder bed fusion processes (PBF) for metal AM , electron beam melting (EBM) and selective laser melting (SLM) are the two primary powder bed fusion techniques

[11,14]. Both EBM and SLM processes have their own unique characteristics [5,12]. EBM is reportedly capable of producing components with lower porosity, as low as 0.1 % by volume [14]. Powder spreading and choice of electron beam parameters are critically important to achieving fully dense parts [19,35]. Poor control of pore size and pore distribution can be detrimental to the mechanical properties and component reliability, even for metal with low porosity. Tight control of porosity for a single build, but inconsistent levels of porosity over multiple builds due to process variability can have equally dire consequences.

Due to its prevalence in nondestructive inspection [39], microcomputed tomography (μCT) has been identified as a viable approach for quantifying the pore distributions in AM parts [40]. Characterizing porosity from μCT reconstructions requires the appropriate image analysis techniques and sequences [41,42]. Furthermore, the information acquired from CT reconstructions is a promising source of data for statistical qualification of metal AM parts [43].

Based on the high cost of feedstock, powder reuse is considered a key factor in the industrialization of metal AM in commercial aerospace. The effects of powder reuse on printed metal properties has been investigated for the SLM and EBM processes and has included nickel and titanium alloys [25,27]. Previous investigations concerning EBM of Ti6Al4V have explored the evolution in powder microstructure [22] and the changes in oxygen content with powder reuse [24]. There are changes to the powder morphology with reuse [23], which can reduce the flowability [19]. These changes in powder characteristics could influence the packing factor, which is relevant to metal porosity. However, the importance of powder reuse to the metal porosity and its spatial distribution in metal AM components has received limited attention.

Gruber et al., [63] recently presented results of a novel investigation concerning the generation of defects in EBM of Inconel 718 as function of powder reuse. In that study, the porosity

increased with reuse as a consequence of precipitates that formed with accumulation of excess interstitial elements. That mechanism may not contribute to the development of porosity in other metal systems, for example Ti6Al4V. Understanding whether powder reuse contributes to porosity for titanium is a critical concern that must be addressed. The present study is the first to evaluate how powder reuse contributes to metal porosity in EBM of Grade 5 Ti6Al4V.

3.3 Materials and Methods

A Grade 5 Titanium alloy (Ti6Al4V) powder was acquired from the machine manufacturer for this study (ARCAM: Batch P1303, Part #430944). The program started with a total of 50 kg of powder.

3.3.1 *Build Design and Powder Reuse*

The printing process was conducted with an ARCAM A2X Electron Beam AM system. All printing was conducted according to the default parameters of the machine for Ti6Al4V, which includes a beam speed of 4530 mm/s, beam current of 15 mA, max current of 20 mA, focus offset of 25 mA and speed function of 45. The influence of powder reuse on the printed metal porosity was evaluated using a simple cylindrical part with 6 mm diameter and 21 mm height. The geometry was chosen to best serve the μCT analysis. The build design is shown in Figure 3.1a. As evident from this figure, the part was printed together with additional specimens that were used for characterizing other aspects of the microstructure and mechanical properties of the metal with reuse.

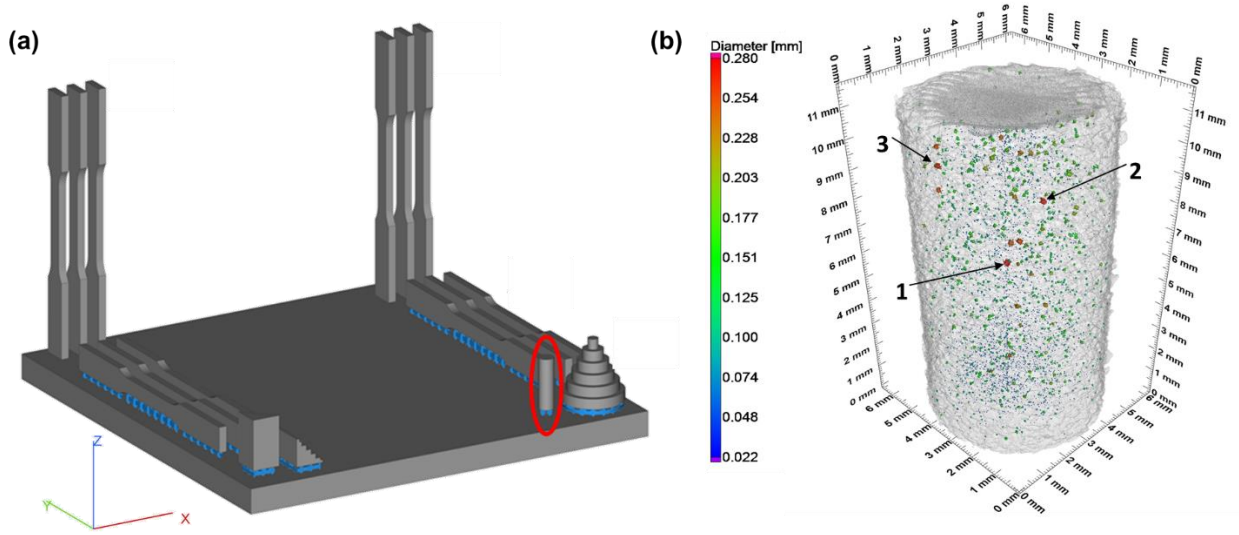

Figure 3.1. **(a)** Build design used through the powder reuse study. Circled in red is the cylindrical part that was scanned via µCT. **(b)** Pore size distribution as identified by µCT. The three largest pores in this representative cylinder are highlighted with arrows and have effective diameters of 280 µm (**1**), 270 µm (**2**), and 260 µm (**3**).

Thirty consecutive builds were performed over a period of approximately 6 months using the EBM system. The total powder consumed in each build was approximately 0.16 kg, and roughly 12 kg of powder was exposed to the electron beam during the pre- and post- heating stages. For consistency, part placement remained the same in all builds of the investigation. The builds were defined from b1 for the first build, which was performed with virgin powder, and subsequently up to b30 for the final build. After completion of a build, all partially sintered powder was removed from the build plate and parts using the Powder Recovery System (PRS). ARCAM recommends mixing virgin Ti6Al4V powder with the powder retrieved from each build. However, in the present study that process was circumvented to accelerate powder aging. A more detailed

explanation of the powder reuse procedures, build design, and purpose of all parts in the build have been outlined earlier within Chapter 2 of this document and in Reference [64].

3.3.2 *MicroCT Analysis*

The porosity and its distribution within the cylindrical components of the thirty builds were evaluated using X-Ray micro computed tomography (μCT). The evaluation was performed using a commercial system (X5000, North Star Imaging (NSI), Rogers, MN, USA). Scans were performed in a step mode, averaging two frames for each step. A total of 1600 projections were taken for the full 360° rotation. The scan parameters and fixturing consisted of power source settings of 100 kV and 100 uA, with geometric zoom of 20.83X, no binning, 1 fps, and a 0.127 mm brass filter. A dark field offset, and 7 gain maps were attained prior to the scans, which were taken to ensure accuracy of the greyscale variations in the projections. Using the aforementioned parameters, the resolution was approximately 9 μm. Low and high edge-preserving gaussian noise filters were explored in pilot studies to determine their effect on measurement of the pore sizes. Application of the low noise filter introduced errors in the porosity measurements. In contrast, the high noise filter had no apparent effect on the results, i.e. the volumetric porosity did not change and there was only a small decrease in the low probability pores. As such, a high noise filter was applied to all scans to decrease computation time.

Projections were first reconstructed in the proprietary software of the μCT system (efX CT, NSI, Rogers, MN, USA). This software embedded the geometric data from the geometry tool after the specimen was scanned. Once reconstructed, the volume was then exported as a slice stack along the build height direction and then imported to VGSTUDIO MAX (Volume Graphics Inc., Charlotte, NC, USA) where the surface was determined using automatic determination due to the very distinct material and background intensity peaks. Pores were excluded during the surface

determination so they could be included in the porosity calculation. Porosity was then calculated with special care to exclude μCT streak artifacts. A fully reconstructed porosity map from μCT evaluation is shown in Figure 3.1b. The three pores with largest effective diameter are highlighted in this figure along with the measured total porosity (pore volume per cylinder volume).

The porosity data was then analyzed to extract important characteristics related to the pores within the parts and trends with powder reuse. Most important for this analysis were the pore size and its distribution. The pore morphology was also analyzed due to its contribution to the effective stress concentration posed by the pore. In addition, the spatial distribution of pores was evaluated in two ways. The first approach evaluated the pore concentration along the build direction (z-axis). The second approach evaluated the spatial distribution of pores in-plane with the build layers. The radial distance from the center of the printed cylinders to their free surface was used for quantitatively assessing the pore distribution, which took advantage of the axisymmetric circular cross-section of the printed cylinders.

Machine learning (ML) approaches are becoming more prevalent in materials processing and selection [25, 26]. One major application in metal AM has been developing ML algorithms for defect detection and in-situ monitoring during the printing process [27–29]. To further evaluate contributions from the porosity to mechanical properties of the Ti6Al4V, a form of machine learning (ML) was applied to the μCT dataset for porosity. Self-organizing maps (SOM) are a ML technique where an array of points of arbitrary location in multidimensional space are slowly iterated, based on weighting of the variables and neighbor distance, until they align with data points in the multidimensional space [65]. The SOM enables visual correlations to be made between the variables of interest in a two-dimensional space. A recent application explored relationships between materials properties for material selection [66]. In the present study, SOMs were applied

to results of the μCT analysis and the pore characteristics to identify the factors that have the greatest influence on mechanical properties.

3.3.3 *Microscopy*

Optical Microcopy (OM; Olympus BX50 Microscope, Olympus Scientific Solutions America, Waltham, MA, USA) and Scanning Electron Microscopy (SEM; JSM-6010PLUS/LA, JEOL USA Inc., Peabody, MA, USA) were used to visually inspect voids within the specimens that were identified in the microstructural analysis. In addition, a fractographic analysis was performed on the fracture surfaces of specimens from the same builds that were subjected to tensile loading to failure (Figure 3.1a). This analysis included specimens with both vertical and horizontal orientations to further assess qualities of the voids and their contributions to the initiation of failure. Detailed results concerning the microstructure and mechanical properties of the metal as a function of powder reuse are reported elsewhere [64,67]. Nevertheless, relevant results of the tensile testing are provided in Appendix A for review and correlation with the porosity measurements.

3.4 RESULTS

Porosity measurements were obtained from analysis of the μCT scans of the cylindrical specimens produced in builds b1 to b30. The volumetric porosity ranged between 0.06 to 0.14 % and the overall average volumetric porosity including the metal from all builds was 0.10±0.02 %. There was no trend in the volumetric porosity of the Ti6Al4V with powder reuse over the 30 builds.

While volumetric porosity provides an understanding of the metal density, it does not describe important specifics such as the pore size and its distribution. Excluding the build b7, which was identified to contain several layers of unfused metal, the measured pore size (effective diameter) ranged from roughly 20 μm to 440 μm. The median pore size over the 30 builds as well

as the distributions in the upper (D90) and lower (D10) tenth percentiles are shown in Figure 3.2. These values provide an understanding of the range in pore sizes and their evolution with powder reuse. For instance, a high D90 for a specific build indicates a greater number of larger pores when compared to other builds. As evident from Figure 3.2, the median pore diameter increases slightly with build number. The D10 exhibits a similar increase as the median. Conversely, the D90 values undergo a decrease with build number, indicating that there is a lower number of large pores with increasing powder reuse. It is noteworthy that the build to build variation was relatively large, with some builds exhibiting pore sizes on the fringe of the size distribution, which is not apparent in Figure 3.2. Specifically, b11 has a similar D90 as b1, yet the largest three pores in b11 (average diameter of 400 µm) are substantially larger than those in b1 (270 µm). Due to the variation in build to build pore size, linear regression fits of the pore size trends with respect to powder reuse were not statistically significant.

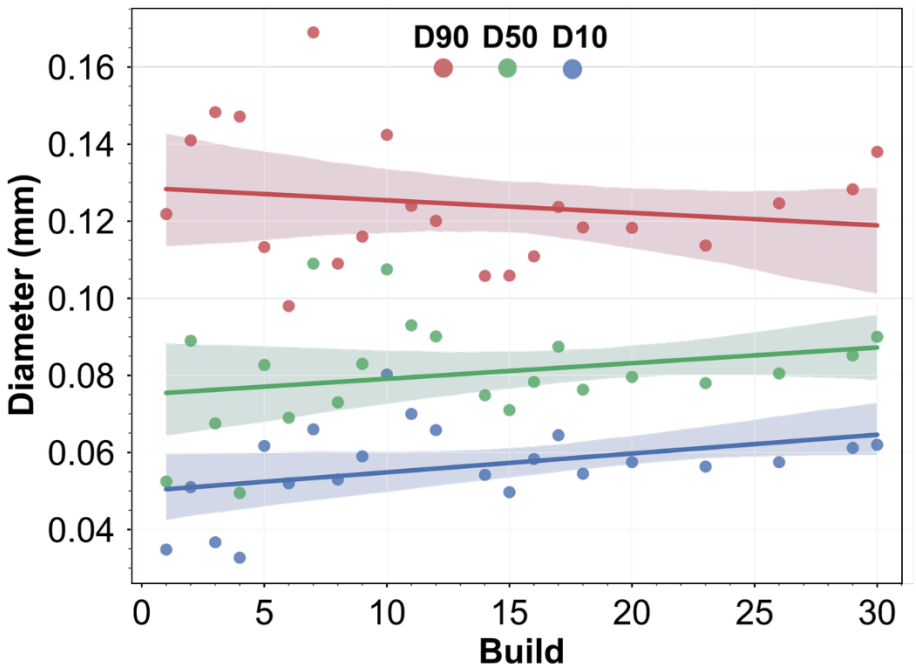

Figure 3.2. Effective diameter distribution of pores across multiple builds. The measures DXX (e.g. D10, D50, and D90) represent diameter at which XX% of the particles have that diameter or smaller. Note the size distribution with repeated builds becomes tighter and the disappearance of small pores. Linear fits are shown with 95% confidence intervals.

Apart from pore diameter, the shape of internal pores and changes with powder reuse are also important to the metal structural behavior. Pores with high aspect ratio are more likely to pose high stress concentrations due to the smaller notch root radius [68]. The sphericity of the pores is one approach to quantify this quality. A spherical pore located far from the surface has a stress concentration that is consistent with that of a cylindrical internal defect [69]. However, depending on its orientation with respect to the direction of maximum normal stress [70], an irregular-shaped pore with low sphericity has potential for posing much higher stress concentration. The size distribution of the pores was examined as a function of their sphericity and results of these estimates are presented in Figure 3.3. Specifically, the pore size distributions are shown as a function of sphericity for builds 1, 10, 20 and 30 in Figure 3.3a through 3.3d, respectively. As evident from the distributions, the smallest pores have the highest sphericity (closer to 1), whereas the large pores have low sphericity (i.e. high aspect ratio). These pores are the most likely to serve as detrimental defects to the printed metal. Low sphericity is an indication of high aspect ratio and irregularity in pore shape. Of note, sphericity measurements do not convey whether there are adjacent pores that promote multi-site damage.

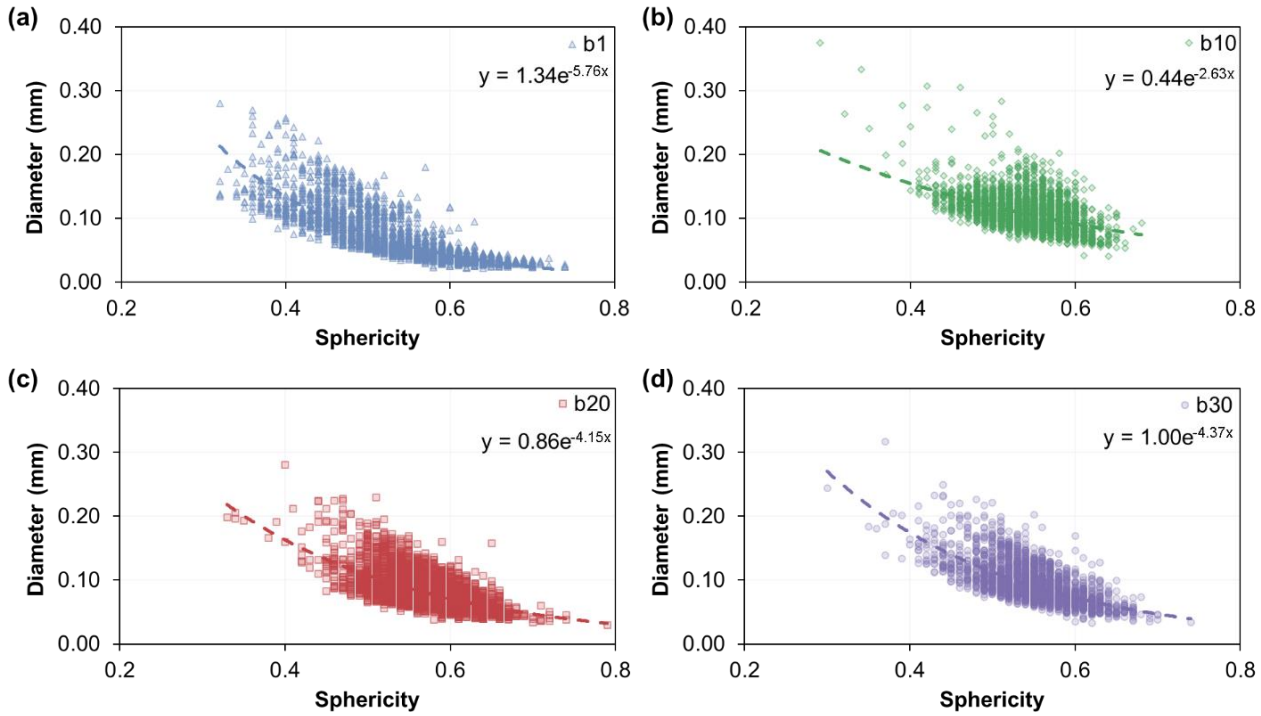

Figure 3.3. Diameter of pores as a function of sphericity for builds: **(a)** b1, **(b)** b10, **(c)** b20 and **(d)** b30, respectively. The porosity follows an inverse exponential trend between size and shape. Larger pores have lower sphericity, promoting higher stress concentration.

Another important factor is the location of the pores with relation to the component geometry and their distribution. There are two aspects of pore location in the cylindrical specimens, namely: i) the distance of the pore from the surface of the cylinder and within the plane of the build layers, and ii) the location with respect to build height. To convey these aspects of the spatial distribution, pore density maps were developed as described schematically in Figure 3.4a. The x-axis represents the radial distance of pores from the outer circumference to the centroid. The concentration of pores about the entire circumference can be obtained by superposing the pore distributions identified from all radial slices as shown in Figure 3.4b. The origin of the plot at 0.0 mm refers to the exterior surface and the edge distance represents the radial distance from the

exterior surface to the central axis of the cylindrical specimen. Similarly, the y-axis refers to the vertical distance from the build plate (i.e. build height). According to this representation, the density map represents a planar depiction of radial slices from the reconstruction that are collapsed onto a single plane (Figure 3.4b). Histograms of the pore density are shown for the radial direction and height to compliment the density maps.

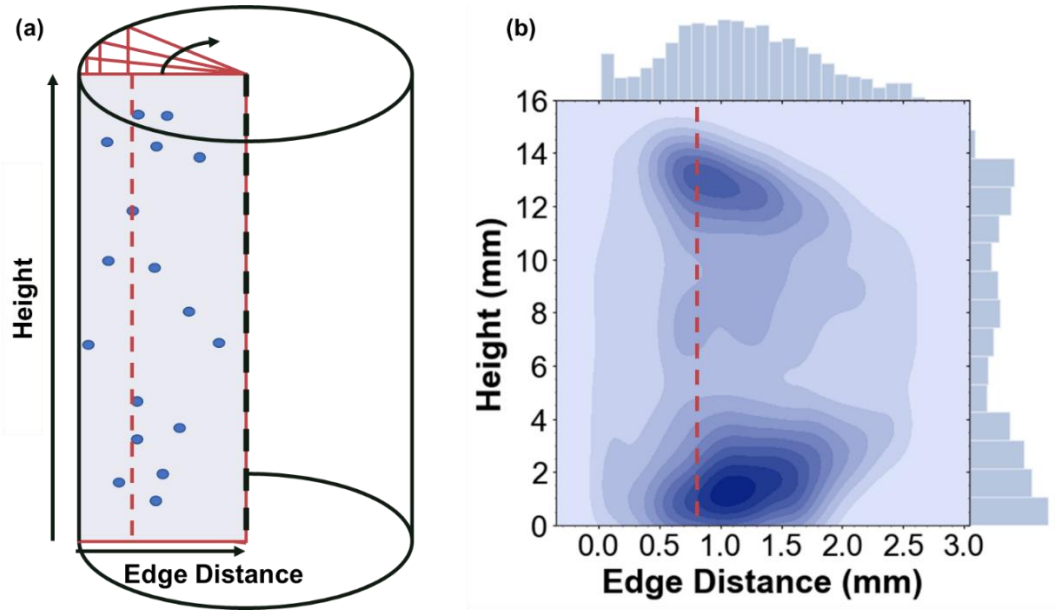

Figure 3.4. Pore distributions within the cylinders**. (a)** Schematic representation of a μCT specimen. A radial slice of the cylinder is shown with example pores. **(b)** Density plot of the pore locations as a function of height and edge distance. To build this plot a summation is taken of all radial planes with pores. The dotted red line in (a) and (b) corresponds to the edge distance with the greatest number of pores across all radial planes evaluated.

Pore density maps for the metal from representative builds are shown in Figure 3.5. Specifically, pore density maps for b1, b10, b20 and b30 are shown in Figures 3.5a through 3.5d, respectively. A height dependence is evident in the pore map for b1 (Figure 3.5a), with greatest

density near the top and bottom of the cylinder. However, this height dependence is not represented in the pore distributions of metal builds performed with reused powder. The most prominent trend among the maps is the consistency in pore distributions in the radial direction; there is a peak in pore concentration between approximately 0.5 and 1 mm radially inward from the surface of the cylinder. This is a ring of high porosity that spans the entire cylinder height. However, with increasing proximity to the central axis there is a steady decrease in the porosity. The spatial distribution in pores is clearest when the maps are restricted to the largest pores in the part (>D90). In other words, the spatial distribution of pores is independent of size variation due to consistent location for pores of large and small diameter.

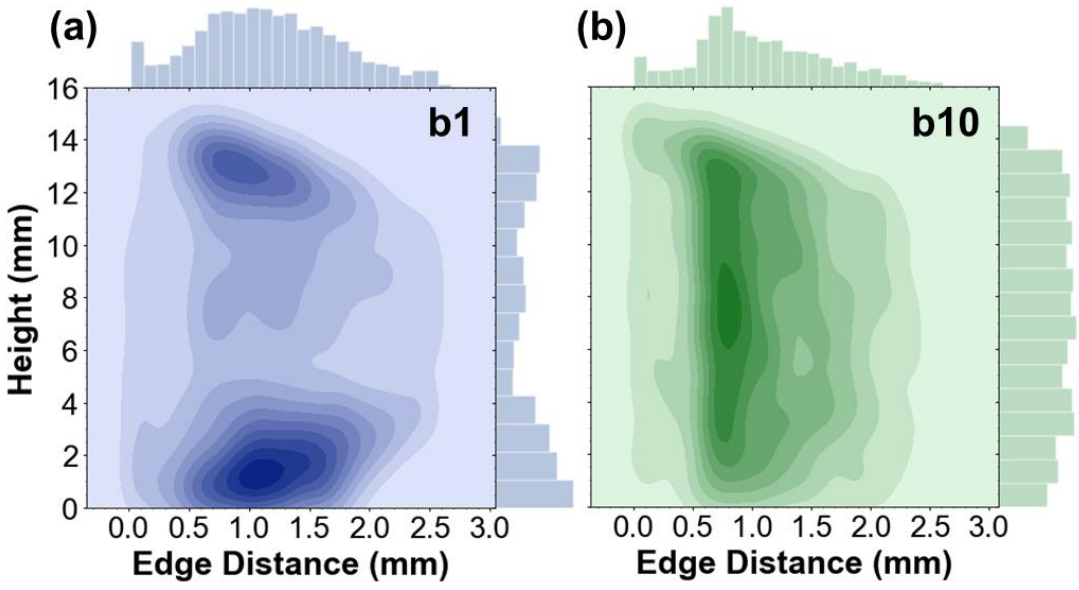

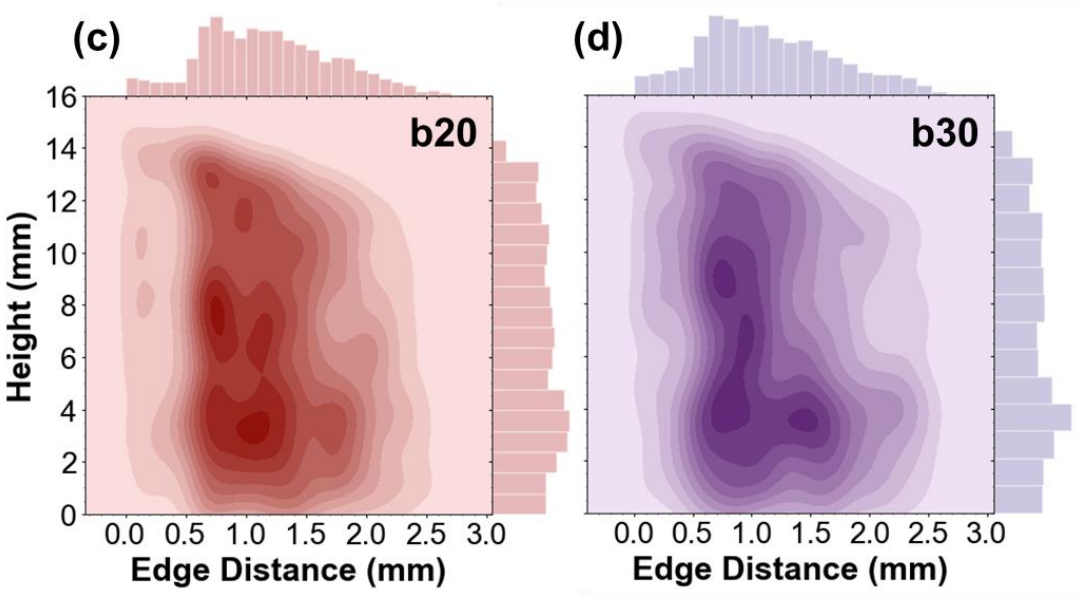

Figure 3.5. Pore density maps within the cylindrical specimens for metal of **(a)** b1, **(b)** b10, **(c)** b20 and **(d)** b30, respectively.

In addition to quantifying the pore distributions, there is equal value in understanding their geometry and other characteristics. Figure 3.6 shows representative pores observed near the central axis of specimens cross-sectioned along the longitudinal axis. Two different families of pores were identified. The first family is characterized by large effective diameters and low sphericity. These pores are most commonly oriented within the plane of the build layers and appear to result from incomplete fusion or a lack of fusion (LOF). Due to their shape, these pores would be expected to be more detrimental to the structural behavior of metal AM parts. The second family of pores involves those with smaller effective diameter and high sphericity. Both pore types are represented in the sphericity to diameter distributions presented in Figure 3.3. The data points residing in the top left of these figures constitute the first family, and those at the bottom right are of the second family.

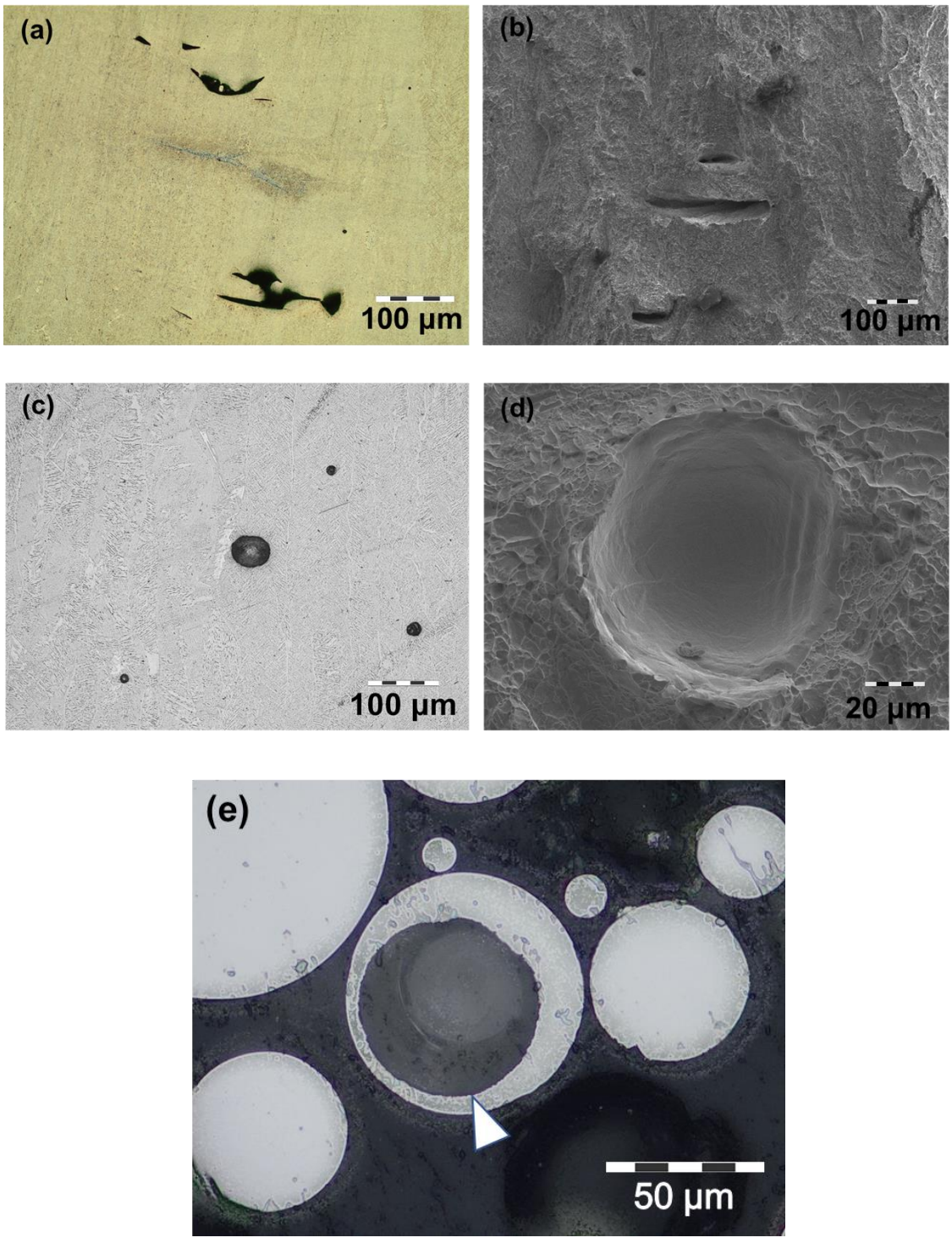

Figure 3.6. Example pores found in as-built parts. **(a)** and **(b)** show examples of "lack of fusion" (LOF) voids, elongated in the build plane and possessing sharp corners. **(c)** and **(d)** are examples

of gas entrapped voids, which are spherical and smaller than the LOF voids. **(e)** Arrow points to an example of a pore contained in virgin powder.

The tensile specimens within the build were tested to failure and results for both horizontal and vertical specimens are listed in Appendix A. The mechanical properties were evaluated as a function of various aspects of powder reuse. In addition, fractography was performed to further establish the perceived contribution of pores to the initiation of failure [67]. The fracture surfaces revealed that the large LOF voids could contribute to failure, regardless of the tensile specimen orientation with regards to build direction. The fracture surface of a representative specimen with horizontal orientation from b2 is shown in Figure 3.7.

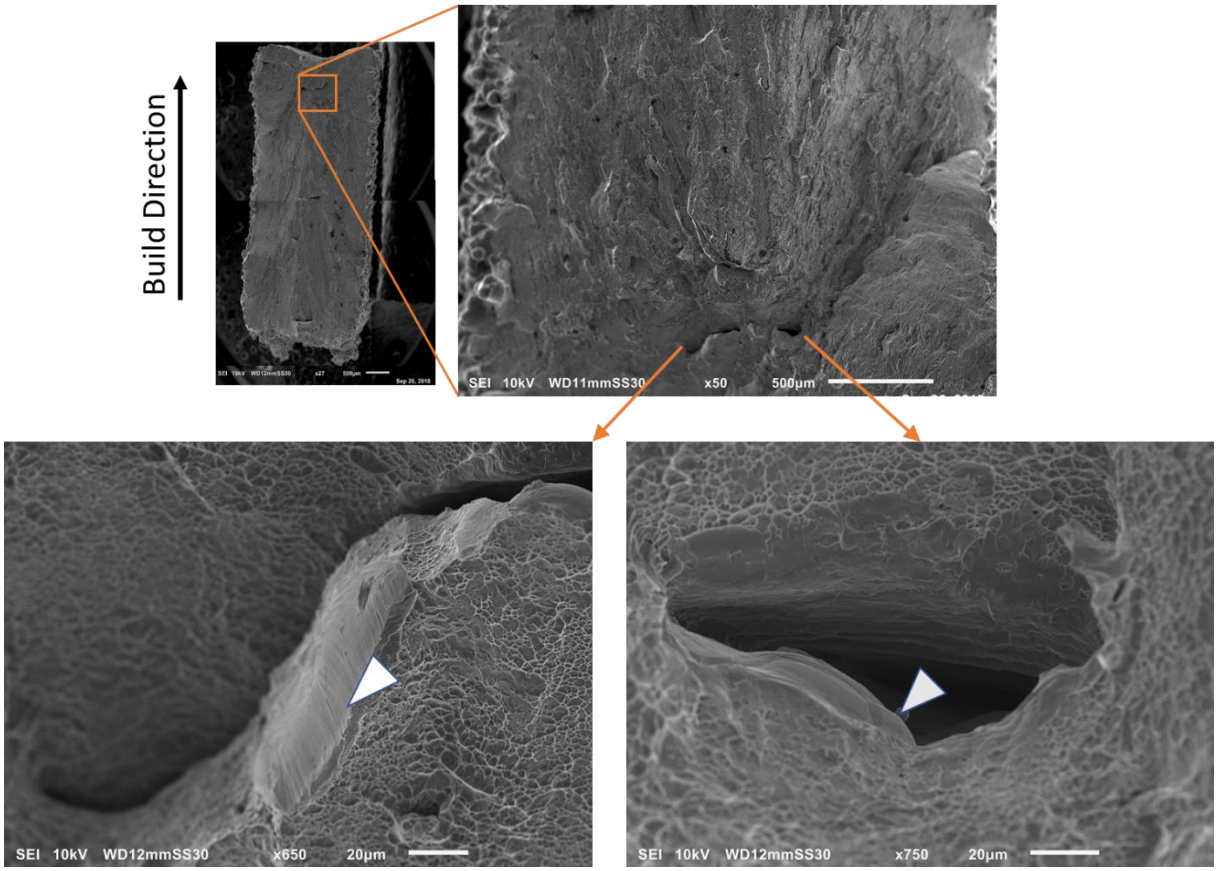

Figure 3.7. Scanning electron micrographs of the fracture surface for a horizontally oriented tensile specimen. The build direction (z-axis) is parallel to the fracture surface. Fracture of this specimen appears to have originated from large internal pores.

Two large LOF voids are apparent and in close proximity to one another. Both have a smooth interior surface suggestive of freezing of the melt pool within the specimen interior. Although these voids started in plane with a build layer as a result of incomplete fusion, they proceeded through several build layers as evident in the micrograph. The fracture surface for a representative tensile specimen with vertical orientation is shown in Figure 3.8. The fracture origin appears to be at the as-built surface that is in close proximity to large LOF voids within the interior, which is noted from the smooth surface formed by solidification. The distributed stress concentration from the as built surface and the cluster of LOF voids likely contributed to failure. These observations highlight that understanding and controlling porosity is essential to metal reliability, and that knowledge of the pore size and shape is essential to interpreting the mechanical properties and failure origins. They should be assessed in quantitative evaluations of metal produced by powder bed fusion processes.

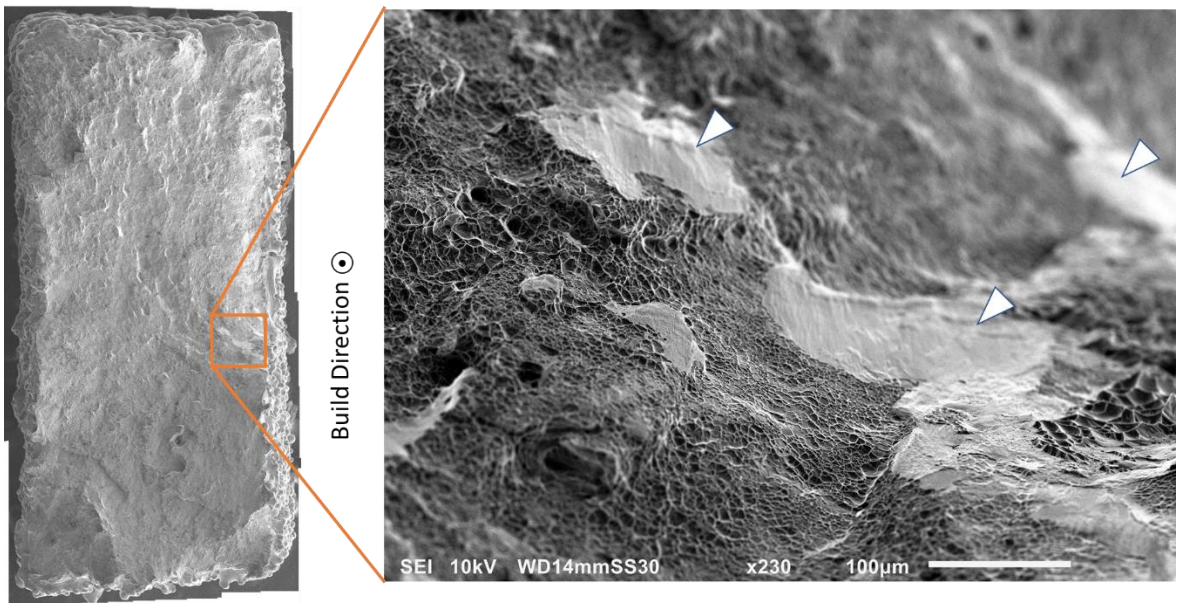

Figure 3.8. Scanning electron micrographs of the fracture surface for a vertically oriented tensile specimen. The build direction is perpendicular to the fracture surface (and plane of the figure). The origin of fracture appears at the as-built surface adjacent to three large lack of fusion voids indicated in the enlarged SEM image on the right.

3.5 DISCUSSION

As a consequence of the advances in metal AM processes over the past decade, the opportunities for industrial application are rapidly expanding. The aerospace and automotive industries envision its use for a variety of applications that include safety- and mission-critical components. For these applications, a comprehensive understanding of metal quality and its reliability will be essential. These are industries where the consumption and costs of powder feedstock are high, which increases the importance of powder reuse. And due to the potential degradation in structural integrity caused by pores, understanding the effect of powder reuse on porosity in metal AM is a necessity. However, despite the significance of this topic it has not been addressed in sufficient detail.

There was no significant change in the porosity of the printed Ti6Al4V specimens with powder reuse; the overall average by volume was 0.10±0.02%. This finding is not consistent with the increase in porosity with powder reuse reported by Gruber et al., [63] in EBM of a nickel alloy. In that study, an increase in oxidation occurred with reuse that caused the formation of oxide precipitates, which triggered the development of large pores (i.e., LOF voids). The number of these defects increased substantially in the later builds that were conducted with highly reused powder. In the present study, there was also a significant increase in oxygen contamination of the Ti6Al4V powder with reuse, increasing from roughly 0.13 wt% in b1 to 0.36 wt% in b30. In comparison, in Gruber et al. [63] the oxygen content in Inconel 718 went from 0.15 wt% to 0.31 wt% across 30 builds. Unlike Inconel 718, which forms Al_2O_3 precipitates in AM [71], Ti6Al4V does not due to the high solubility of aluminum and oxygen, tolerating up to approximately 13 wt% oxygen [72,73] or 24.5 wt% aluminum [74] in a pure titanium matrix. Even though oxide precipitates are not a concern, the brittle Ti_3Al phase develops with increasing oxygen content [73,75]. It is unclear if the Ti_3Al would increase defect generation in a similar fashion as Al_2O_3 in Inconel. Nevertheless, the levels of oxygen that induce the Ti_3Al phase would cause severe embrittlement and render the alloy unusable for industrial purposes.

According to the size and sphericity measurements there were two families of pores in the metal, including: i) those with smaller diameter ($d \leq 50$ μm) and higher sphericity (sphericity $\geq$ 0.6), and ii) the larger pores with comparatively low sphericity. Previous investigations have also characterized the porosity in AM parts and characteristics of the pores [32,76]. Cunningham et al [32] reported that the small pores in the built metal are consistent in size and shape with those in the plasma atomized powder, which could suggest that the residual pores within the particles become entrapped in the melt pool. Indeed, there are spherical pores in the powder that can be a

significant portion of the powder volume [31]. For the Ti6Al4V powder, the pores in sectioned particles (Figure 3.6e) were consistent with those in the metal with high circularity, which were evident in the sectioned surfaces and on fracture surfaces of the tensile specimens.

Whereas the largest contributor to the total pore count in the metal was the dispersion of small pores, the larger pores are more concerning. According to previous studies, the large pores can be a product of improper layering of the powder [77] and/or the incomplete melting of powder that results from poor beam parameter optimization [33,37,44,77]. Improper layering of the powder in EBM could evolve with reuse due to changes in powder morphology. Irregular shapes and damage can cause greater resistance to flow and interfere with the powder distribution process. Powder with low flowability would be expected to have greater tendency to form gaps and holes in the build layers. Nevertheless, there is contradicting reports that the powder flowability increases with reuse [19,27,28].

The second plausible cause of larger pores is beam irregularities, and inconsistent beam overlap during the scanning strategy. Tammas-Williams et al. [78] analyzed pores in Ti6Al4V resulting from EBM with different beam scan strategies. In that study a greater concentration of large lack of fusion pores was observed to develop in the contour beam region, which was attributed to the narrow beam paths and lack of overlap. However, the majority of large and irregular pores in the present study were observed to be within the interior hatching melt region. Finally, a poor temperature distribution within the melt pool could also cause LOF voids to develop between or within individual layers; improper pre-heating or maintenance of the temperature are primary contributors [44]. Yet, these issues are more likely when building with low beam power or fast scan speeds [33,44], which are not are not relevant to the present study. Therefore, there is

some inconsistency in the apparent mechanisms responsible for the development of LOF voids among the published studies. Future work appears warranted to improve the current understanding.

A primary concern in metal AM overall is the contribution of metal defects to the structural behavior of components. In the present program, only weak correlations were identified between the mechanical properties and the various measures of porosity; the metal ductility showed the most sensitivity to pores. Comparing the tensile properties of specimens with horizontal and vertical orientation (Figure 3.1a), those with vertical orientation underwent the largest decrease in ductility with increasing porosity. There was a 30% decrease in ductility of the Ti6Al4V specimens with vertical orientation over only 0.08% increase in overall porosity (from .06 % to 0.14% by volume). For commercially pure titanium, minor increases in porosity can cause large reductions in ductility. However the effects of porosity are reportedly not as substantial for Ti6Al4V [79]. The decrease in ductility with small rise in porosity is expected to result primarily from the largest pores and the stress concentration they pose [80]. According to fractographic analysis of the failed tensile specimens, LOF voids contributed to failure. Indeed, when the % elongation of the vertical tensile specimens is plotted in terms of the average effective diameter (diameter of the defect in the XY plane perpendicular to loading axis) of the three largest pores in the scanned metal, there is a distinct trend, which is shown in Figure 3.9. A similar trend has been established for extreme size pores in powder metallurgy of Ti6Al4V [81]. Of note, the measured mechanical properties and porosity are from two different sources/components in the build. That provides at least some support for the use of witness specimens or test coupon to assess the metal response of all parts in a build. Nevertheless, additional work is necessary to further establish their value in industrial practice.

In contrast to the relationship between the LOF voids and ductility for the vertical specimens, there was no distinct dependence on LOF voids evident for the horizontal specimens (Figure 3.9). For the horizontal specimens, LOF voids are generally oriented parallel to the loading direction, which mitigates the degree of stress concentration. And in the absence of changes in porosity with powder reuse, the decrease in ductility of the horizontal specimens with increasing build number was due to oxygen embrittlement [64].

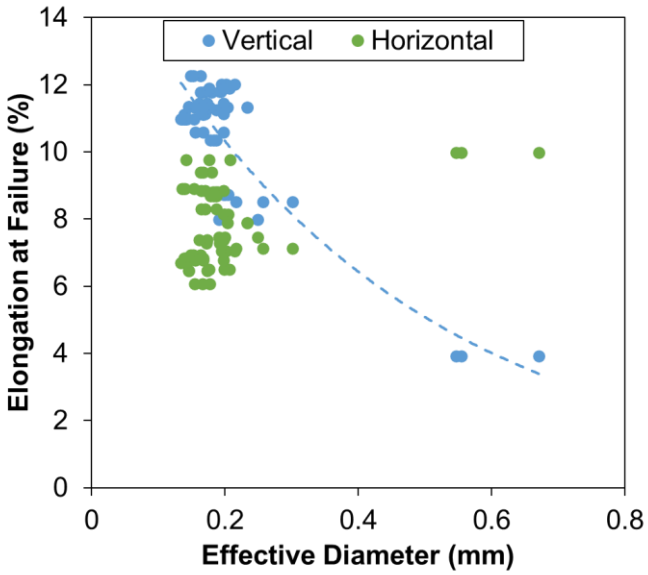

Figure 3.9. % elongation at failure for Horizontal and Vertical tensile specimens as a function of the effective diameter of a pore in the XY plane. Exponential fit line applied to Vertical specimens. % elongation was detrended regarding oxygen content to isolate the effect of porosity, i.e. the linear relationship of oxygen embrittlement was removed from the data so it no longer influences the % elongation

There was a difference in the spatial distribution of pores within the Ti6Al4V cylinders produced with virgin and reused powder. The porosity maps for the builds performed with virgin

powder (Figure 3.4a) showed that there was bimodal distribution of pores with height. Higher pore concentrations were located at the bottom and top of the cylinder. However, the builds conducted with reused powder (builds b2 and greater) showed a more uniform spatial distribution in pores with height (Figure 3.4b-d). Differences were also evident in the radial distribution of pores between the builds performed with virgin and reused powder. The radial distribution for b1 was Gaussian, whereas there is a skewed spatial distribution in pores for the builds performed with reused powder. As evident from the maps in Figure 3.4b-d, there is a peak concentration near the surface. That is followed by a decrease towards the interior and then a concentration of pores approximately 0.5 to 1.0 mm radially inward from the surface. This near-surface concentration is detrimental as it can superpose with other geometric features to amplify the magnitude of stress concentration [82]. Pores located near the surface can also interact with the surface roughness and compound the potential for near-surface failures. Removal of these pores by post-processing approaches would require substantial effort and is undesirable.

The unique radial distribution of pores is very evident in pore histograms obtained from the reconstructed μCT images. Representative results for the cylinder of b11 are shown in Figure 3.10. Specifically, perspective projections along the central axis of the cylinder including all pores in the scanned volume and (b) only pores above D90 in b11 are shown in Figure 3.10a and 3.10b, respectively. The region of peak pore density is highlighted in the red region. The normalized distribution of those pores as a function of edge distance for these two pore sets are shown in Figure 3.10c and 3.10d, respectively. Despite the application of thresholding to consider only the large pores (>D90), the reconstructed image (Figure 3.10b) and histogram (Figure 3.10d) for the pore distribution exhibit the same trends as those considering the entire pore size distribution. Specifically, the highest pore concentration is located between 0.5 to 1 mm radially from the

exterior surface. According to the pore shape and size relationships (Figure 3.3), the pores in this outer ring pose the largest stress concentration due to their irregular shape and sharp corners. Masou et al., [83] showed that a high concentration of large and/or sharp pores in the build plane can interact synergistically as a larger effective pore. Compounding effects of defects raises further concern with this near-surface ring of pores.

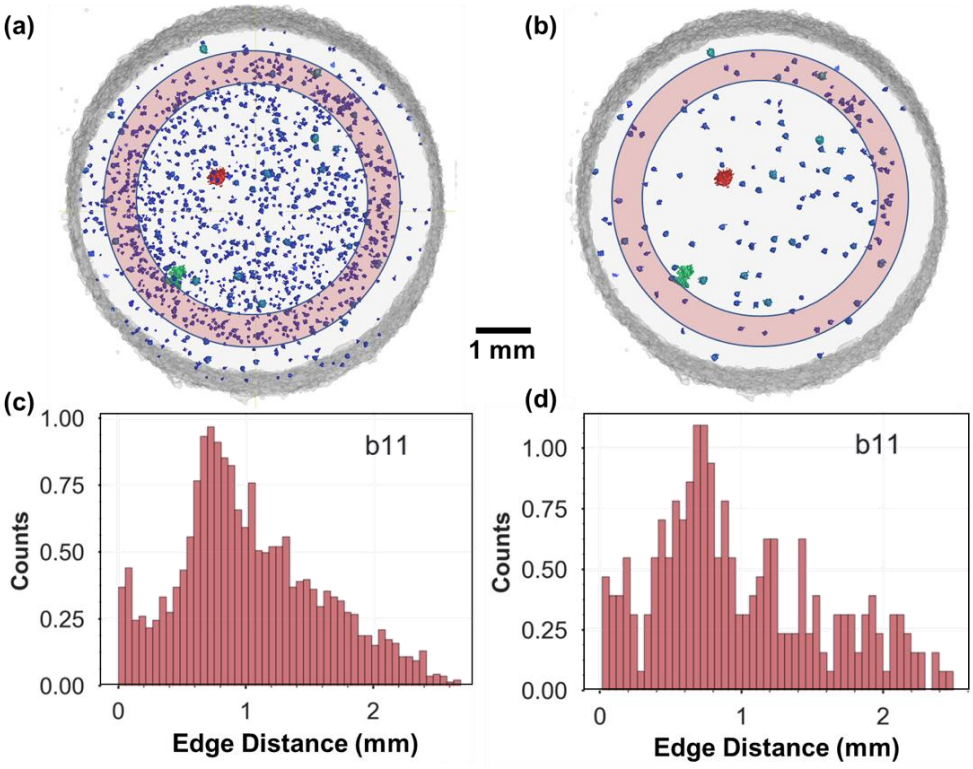

Figure 3.10. Pore distributions in μCT reconstructions. Perspective projections of **(a)** all pores in the entire scanned part volume and **(b)** only pores above D90 in b11. The highlighted red region is the range where the count peak occurs. The normalized distribution of those pores as a function of the distances from the edge of the part for these two pore sets are shown in **(c)** and **(d),** respectively. Note the higher apparent concentration of pores around 0.5-1.0 mm in these specimens.

The circumferential ring of high pore density (0.5 to1.0 mm from the cylinder edge) was identified in all the cylinders produced with reused powder. That suggests contribution from a systematic error in processing. Although powder reuse was not a consideration in the recent work of Tammas-Williams et al., [78], they also noted a similar characteristic in higher pore concentration. The region of highly concentrated pores in the cylindrical specimens (Figure 3.10) corresponds to the location where the contour beam and melt pool beam intersect. One plausible explanation is that these pores are formed by an effective cold shut that develops at the intersection of the contour beam and melt pool. Another potential explanation is that the hatching pattern does not allow sufficient overlap of the melt pool beam and contoured beam [84]. The lack of overlap would depend on focusing of the beam prior to the build and melt dynamics of those two beams [45].

One could question if radial distance is the best indicator for mapping the pore/void density since the circumferential area represented in the histograms of Figure 3.10 increases with distance from the cylinder center. The difference in reflected area in these reconstruction maps could manifest as an increasing apparent pore density with radial distance. But when the density distributions were normalized by the circumferential area represented in the reconstructions, there was only a moderate increase in the density closer to the centerline of the cylinder and no change in the location of the peak pore concentration, indicating the region between the contour and melt pool is still the most concerning. Further study should address the contributions of contour beam control and this aspect of the porosity.

Results for the measured porosity with build height are consistent with those of previously reported research [42]. Specifically, in all the builds performed with reused powder, there was no

clear trend between the pore density and build height. Admittedly, there is a limitation to the present study in regard to identifying the dependence of porosity on build height; the cylindrical specimens occupied a relatively small fraction of the build chamber, which can accommodate parts greater than 300 mm in height. That represents an exceptionally large and unexplored build space that is of concern. This topic does not appear to have been explored in detail for EBM of Ti6Al4V and warrants further investigation.

Self-organizing maps (SOM) were applied to the multidimensional porosity data to identify correlations between the various pore metrics and the structural behavior of the metal. Visualization of data using this method elucidated relationships that were not possible to interpret using traditional methods of data analysis. The primary results from application of SOMs to the porosity dataset are shown in Figure 3.11. In assessing potential correlations between porosity and the mechanical properties, there was a clear correlation between the metal ductility and pore characteristics. Pore size appeared to be the most important contributor to ductility of the Ti6Al4V. As evident from the map, the regions of low % elongation correspond to large pore diameter, which was also evident in Figure 3.9. A direct correlation was also identified between the pore sphericity and elongation at failure; spherical pores with lower stress concentration had limited effect on the ductility. Lastly, the % elongation was proportional to the free edge distance; higher ductility was characteristic of metal with pores located larger distance from the free edge. Interaction between the pore morphology and location, as well as between the edge distance and sphericity was also identified. For example, a portion of the region with moderate elongation has high sphericity (>0.6), but low edge distance (<0.5 mm) and results in low ductility.

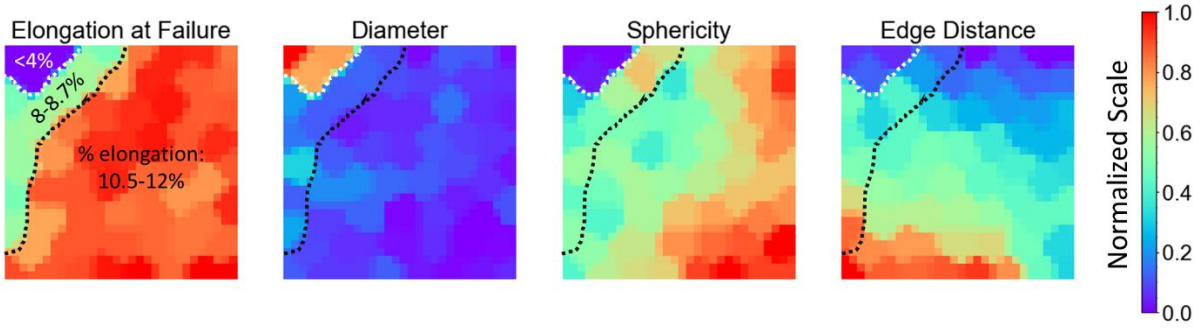

Figure 3.11. Self-organizing maps showing correlations between elongation at failure of vertical specimens and three porosity metrics; size of pores, sphericity, and distance from a free edge. All values are normalized to a 0-1 color bar scale. The white dotted line corresponds to the border for the lowest ductility build, b7 (< 4%). The region between the white and black dotted line is the group of builds (b9, b10, b11) with intermediate ductility. Labelled in the elongation at failure map is the oxygen-detrended percent elongation ranges for each region, which apply to all heat maps.

Machine learning has been applied to various aspects of AM, including in situ defect detection [85,86] and geometric tolerancing [87,88]. Visualization methods such as SOMs and other data science techniques have substantial potential in the field of materials processing and can be useful in finding relationships in high dimensional data [89]. The large number of processing parameters in metal AM is well known and is the primary source of complication. Machine learning techniques appear to offer a potent approach for understanding processing in metal AM and the parametric contributions to property variance. There is a large library of ML techniques that can be applied for this endeavor. Our future work will be concentrated in making advancements in this area.

3.6 CONCLUSIONS

In this study, the porosity in Electron Beam Melting (EBM) of Grade 5 Ti6Al4V was characterized as a function of powder reuse over 30 total build cycles. Pores in the metal were identified by µCT and complimentary post-processing analyses. Volumetric porosity remained constant with powder reuse (avg. = 0.10±0.02%) and individual pores ranged in effective diameter from roughly 20 µm to 440 µm. Similarly, the pore size distribution was mostly constant with an apparent tightening of the distribution with powder reuse, but this trend was not statistically significant. According to a combination of size and sphericity, there were two general families of pores. The large diameter pores exhibited lower sphericity and shape, and larger effective stress concentration, which agrees with previous studies on porosity in metal AM. The small pores appeared to arise from pores in the powder that are entrapped in the melt pool and the solidified build layers, whereas the large pores originated from the inconsistent melting and fusion of powder between layers. Regarding spatial trends, there was a concentration of pores approximately 0.5 to 1 mm from the outer surface of built parts, which coincides with the intersection of the contour beam and hatch melt pool. However, there was no apparent trend in pore distribution with build height and powder reuse. Self-organizing maps helped to identify that pore size, edge distance and sphericity were the most influential characteristics and most detrimental to the metal ductility. Overall, powder reuse does not appear to influence the porosity distributions resulting from EBM of Ti6Al4V, which enables greater focus on other potential contributing factors.

Chapter 4. EFFECTS OF BUILD DESIGN PARAMETERS ON ADDITIVELY MANUFACTURED TI6AL4V TENSILE PROPERTIES

4.1 SYNOPSIS

Variability in the mechanical properties of metal produced through additive manufacturing (AM) has been a topic of extreme interest. Defects, microstructure, and chemical composition are recognized as sources of variation in AM metal. Further understanding of how these factors contribute to the mechanical properties of the metal and how they can be accounted for in the build design is needed. For this investigation, multiple builds were designed and printed to determine the relative influence of part thickness, spacing, and location on tensile properties for Ti6Al4V produced by electron beam melting (EBM). Including both vertically and horizontally oriented specimens, a suite of mechanical properties were evaluated. Both the elongation at failure and tensile toughness were found to be highly correlated with part thickness. These properties for the vertical orientation were further influenced by part location, with non-linear dependence on height and a linear dependence on radial distance from the center of the build plate. The metal with horizontal orientation did not exhibit the same relationships, with only mild correlations with height and radial position. For the mechanical properties of the metal with vertical orientation, the elongation at failure and toughness were primarily dependent on characteristics of the lack of fusion defects, whereas microstructure was the dominant contributor to properties for the horizontal orientation. Visual maps representing property distributions over the build space were constructed. These tools can support the needs of design engineers and lead to more consistent part performance for AM metals.

4.2 INTRODUCTION

Adoption of metal additive manufacturing (AM) is becoming more prominent within a number of industries [4]. Its prevalence is increasing due to the unique benefits of metal AM including reduced weight through optimized topology and fewer parts, lower material waste and cost from near net shape components, and complex structures that would be prohibitively difficult with traditional manufacturing methods [14,30]. But before widespread adoption can be achieved, particularly for stress-critical applications, there are several key areas that need to be addressed. Metal AM processes are relatively complex. There are many sources for process variability to arise and there is a need to reduce variations in feedstock, part microstructure, and defects [62,90,91]. Powder bed fusion (PBF), a metal AM process where planar sections of a part are melted from a layer of pre-alloyed metal powder, may be subject to process variations due to a rather large number of factors [92]. Two energy sources are used for PBF systems, including laser (SLM) and electron beam (EBM), each of which with overlapping and unique issues [93]. Some overarching areas leading to the variation in the mechanical properties of PBF originate from beam parameters, part/build design, and powder condition. More recently, the qualification of parts produced by metal AM techniques has received significant attention [62]. However, there is still substantial progress to be made before stress critical AM parts can be certified for use. Specifically, there is still need to fully understand the property distribution throughout the build envelope and the potential confounding effects associated with the build design.

Most prominent of the build design factors is the orientation of parts. The orientation dependence of tensile and fatigue properties of Ti6Al4V results from the defect orientation and anisotropic microstructure [36,93]. The majority of AM systems used for Ti6Al4V will result in columnar prior beta grains resulting in different mechanical properties in the directions parallel

and perpendicular to the prior beta columns [59,94]. Due to alpha-rich boundary of the prior beta grains, parts with horizontal orientation (in the build plane) will exhibit lower ductility due to the alignment of the grain boundaries to the plane of the maximum normal stress [95]. In addition to microstructural anisotropy, there is also dependence on the defect orientation. For instance, lack of fusion (LOF) voids develop when insufficient or excessive heat is applied to a region of the melt pool [33,36]. In the case of EBM systems, insufficient energy is commonly a function of the rastering speed or hatch spacing [32,33]. Lack of fusion voids are typically large penny shaped defects with sharp edges that act as regions of stress concentration. They are commonly oriented at the interface of adjacent build layers and oriented in the build plan. As such, they will compromise the fatigue properties for vertically oriented parts that contain the defect perpendicular to the loading axis [82].

Another design parameter that influences mechanical properties is the part geometry. In Ti6Al4V components with small cross-sections such as in fine lattice structures, the excessive cooling rates can promote the development of martensitic microstructures [96]. Even in EBM, which operates with elevated temperatures during the entire build process, there could be residual martensitic alpha phase [60]. Aside from martensite, the microstructure of Ti6Al4V will contain a prior beta grain structure. When melting a layer of powder in PBF there is a fine low power beam that outlines the cross-section, which is followed by a high-power beam that rasters within the middle to melt the powder within the outlined region; these are deemed the contour and hatch beams, respectively. The lower beam power of contouring and the close proximity to the thermal boundary leads to the development of more random prior beta grains near the surface of parts. Within the hatching region, the higher power and greater distance to dissipate heat results in columnar prior beta grains [97]. As cross-sectional area is reduced, a greater percentage of the melt

pool will be within the contour. Increasing the ratio of contour to hatch area could be detrimental to ductility and the fatigue properties of parts built in the vertical orientation as the prior beta grains near the surface of the part will have their boundaries oriented approximately 45° to the build plane, rather than the preferential columnar texture present in the interior [17,97].

Part location is an additional design factor that influences mechanical properties in PBF. The location can be defined in terms of the three major axes (X and Y axes in plane with a build layer and the Z axis parallel to the build direction). For example, in SLM the inert gas flows along the Y axis for from the back to the front of the build plane. That gas flow causes a force propelling any matter ejected (typically referred to as spatter) from the melt pool toward the front of the build layer [98]. In EBM, the parts "float" in the build volume, i.e., the part is suspended in the powder and does not have supports attached to other parts or the build plate. Without a large heat sink to draw thermal energy away from the melted metal there can be an increase in heat accumulation in the Z-axis, which may result in a mechanical property gradient in the vertical direction.

Part proximity to each other is the last design consideration of interest that can influence part quality. The relative distance between parts in any axis could influence the dissipation of heat due to the thermal mass of the adjacent part in close proximity. For EBM, this factor will not likely influence the alpha lath dimensions due to the elevated temperature of the build chamber. However, there is a possibility of the spacing factor having some interactions with the other factors [99]. It is important to consider this factor as it is highly probable to be a consequence of part nesting and could amplify the effects of other factors.

Each of the aforementioned build design parameters have been considered in previous studies. However, it is common that the influence of these factors was isolated from the others or that the study was limited to two-factor interactions, which prevents any understanding of factor

interactions. As illustrated with the study on size and orientation effects by Barba et al. [97], factor interactions are common. However, the only study to investigate location and spacing together was performed in laser PBF of 304L stainless steel [99]. Therefore, the present study was designed to investigate the relative influence of location, size, and part proximity and the interactions between factors on the mechanical properties of Ti6Al4V produced with EBM.

4.3 Materials and Methods

The powder used in this study consisted of Grade 5 Titanium alloy (Ti6Al4V) and was acquired from the EBM manufacturer (ARCAM: Batch P1143, Part #430944). The first build, populated with vertically oriented parts, was performed with 100 kg of virgin powder. The second build of horizontally oriented parts were subsequently printed with reused powder from the vertical build. Procedures for powder reuse are outlined in Chapter 2.

A multi-factor experimental approach was adopted to investigate the effects of selected design parameters (factors) and their interactions on the microstructure and mechanical properties of a Ti6Al4V. The factors investigated include the height in the build volume, radial distance from the center of the build plate, part spacing and part thickness as the four factors, which are visually represented in Figure 4.1. Tensile samples were designed to conform to the ASTM E08M subsized specimen dimensions, with reduction in the grip length to accommodate more specimens in the build space while preventing slippage during testing.

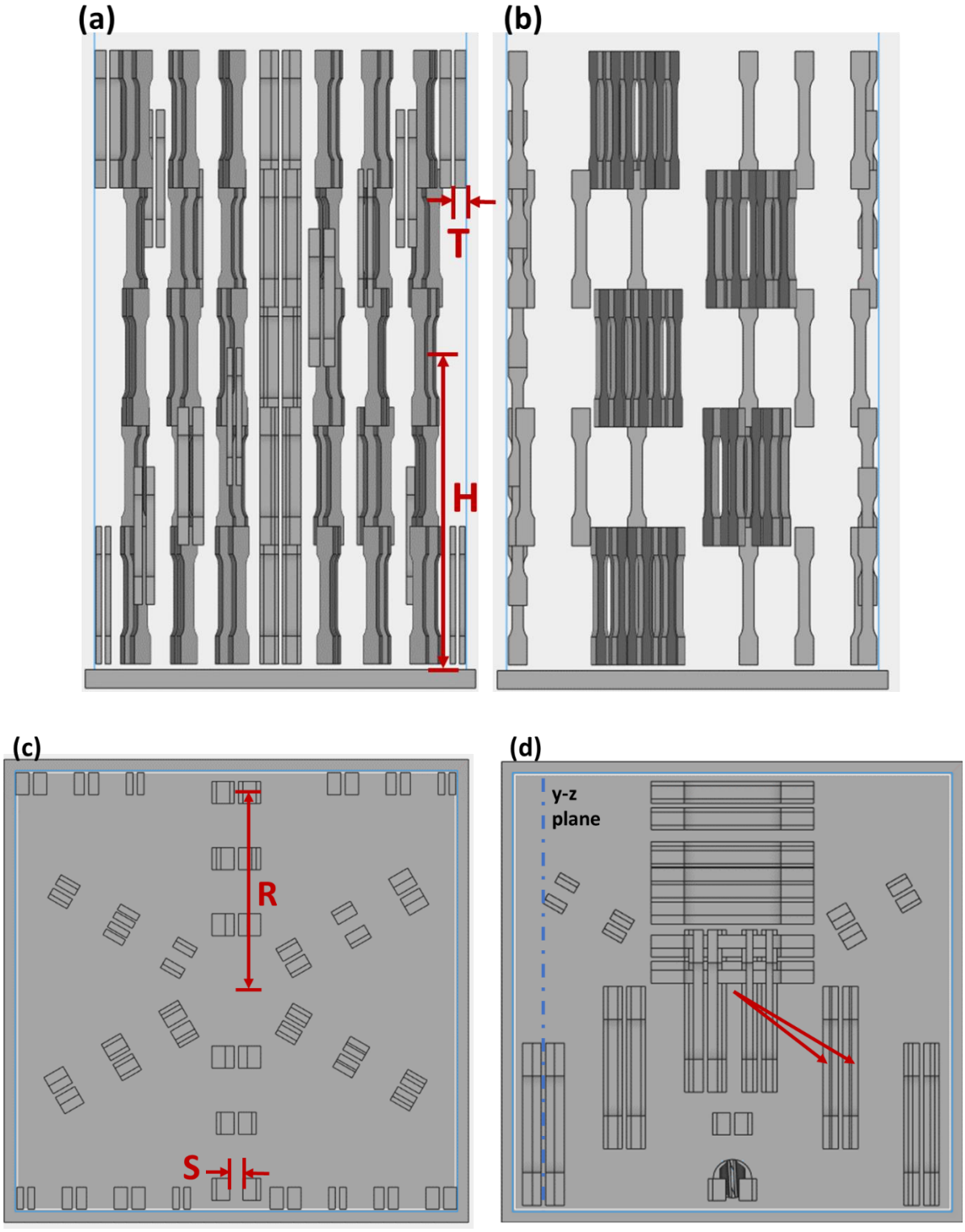

Figure 4.1. Schematic diagram of the build and parameters explored in the DOE for the vertically oriented specimen build. (a) Front, (b) right, and (c) top view. Examples of the factors are shown

as well, including height (**H**) and thickness (**T**) in (a), and spacing (**S**) and radial distance (**R**) in (c). (d) Top view of the horizontally oriented build, where the orientation of the parts is no longer along the radial planes.

Regarding the factors considered in the DOE, the height and radial distance from the center of the build volume represent factors associated with part placement in the build space. The part thickness and their spacing consider the importance of the area to volume ratio of components on the build plane and the packing factor of components in the build space, respectively. As opposed to the height and radial distance, spacing was defined with regards to distance from part surfaces rather than the center of the parts to partially decouple the influence of thickness from spacing. If defined from the part center, thicker specimens would have lower inter-part spacing. The spacing factor will establish if there are effects from the adjacent thermal mass or secondary preheat/post heat stages during the build process on the part properties. Lastly, radial distance was chosen as opposed to the use of a rectangular coordinate space to reduce variables and the number of parts necessary to understand the contributions of spacing. These factors provide a comprehensive description of the build design in EBM that is essential for a thorough understanding of part design and placement.

Two builds were performed for this investigation, one each for vertical and horizontal oriented tensile specimens. Performing builds with both orientations separately ensures that the effects of the factors on the response variables are explored thoroughly and that orientation-specific effects are identified. Extra samples were introduced to bridge the heights where there were no parts at locations of interest. Without parts for intermediate heights there would be minimal heat in these layers. When the next set of specimens is reached, there would be excessive

heating, swelling of the layers, and interference with the rake. As such, a preventative measure was introduced involving the use of extra vertically oriented specimens in both the vertical and horizontal builds. None of the extra specimens were in close proximity of the specimens of interest to avoid convolution with the part spacing factor.

Additional modifications were required for the horizontal specimen build design in comparison to that for the vertical specimens. For the vertical orientation, the longest dimension of the tensile specimen is aligned with the height, which permitted three layers to be built over the entire build height. However, the smaller in plane dimension within the build layer allowed for the pairs to be aligned with the radial line. Unfortunately, alignment with a radial line was not possible for the horizonal specimens. The horizontal tensile specimens have their longest dimension oriented in the build plane and occupy to much length to have radially aligned specimens without interference with the build boundaries. When the horizontal specimens are aligned perpendicular to the radial axis, the third and outermost set of samples is outside of the printable boundaries. In addition, in this orientation the inner most samples have overlap errors. To overcome these two complications, the low and middle thickness samples (3 and 4.5 mm) were oriented parallel to the y-z plane (y axis is to the back of the build chamber and z is the build direction) and this arrangement is shown from the top view in Figure 4.1d. With alignment to the y-z plane a larger span in radial distance can be achieved. Furthermore, the specimens were adjusted in vertical height slightly to accommodate the number of specimens required.

The vertically oriented build was conducted as a fractional factorial design with three levels for each of the four factors. This results in 27 core specimens for this build, with an extra 27 that can act as replicants due to the extra part in each pair of samples. The three levels of the build parameters for the vertical build design are listed in Table 4.1. Since the longest dimension of the

tensile samples of the horizontal specimen orientation are not in the build direction, there is more space for extra heights, and as such two extra intermediate heights were introduced. In addition, the alignment of the 3 and 4.5 mm to the y-z planes permitted a larger span of radial distances to be investigated.

Table 4.1. Factors and the levels investigated for both the vertically and horizontally oriented builds.

	Vertical			**Horizontal**				
Factor Level	Low		High	Low				High
Height (mm)	40	168	296	8	80	152	224	296
Thickness (mm)	3	4.5	6	3		4.5		6
Spacing (mm)	2	6	10	2		6		10
Radial* (mm)	30	60	90	7	38	59	77	111
# of Specimens**		54				79		

*Radial distance of the horizontal build did not consistently stay are set levels due to reorientation of the specimens away from radial plane.
**Number of specimens includes replicates from the pair of specimens.

For all builds, the beam parameters of the melt theme are shown in Table 4.2. The beam parameters were set at these default values for all builds to limit potential influence from causes outside of the build design parameters.

Table 4.2. Arcam A2X beam parameters used for the melting portion of all builds.

Melt theme	
Beam Speed	4530 mm/s
Beam Current	15 mA
Max current	20 mA
Focus offset	25 mA
Speed function	45

4.3.1 *Mechanical Properties*

Tensile testing was conducted on all specimens according to ASTM E08M in a post-machined condition. Approximately 0.4 mm was removed from each side to extend to a depth beyond the visible surface roughness. Removal of the rough surface eliminates its potential contribution to failure, thus improving determination of contributions from the underlying factors on properties. The tensile tests were performed using a commercial universal testing system (Instron: Model 5585H; Norwood, MA) under displacement control loading at a strain rate of 0.05 s^{-1}. The load displacement data was used to generate the corresponding stress-strain responses, which were used for calculation of the elastic modulus, 0.2% offset yield strength, ultimate tensile strength, and % elongation at failure. In addition, the true toughness of the specimens was estimated. Measured properties were evaluated with respect to the factors and analyzed statistically. The statistical analysis was performed using the functions of Minitab 14 (State College, PA). The data was defined as a response surface design and the main effects, linear interactions, and quadratic effects of the factors were evaluated to establish their significance and relative contributions to property variations.

4.3.2 *Microstructure*

To correlate the mechanical properties with microstructure, the gauge section of the tensile sample was investigated after tensile testing. Specifically, four areas were chosen for analysis, including two near the transition area from grips to gauge section and two located 10 mm into the gauge section from the outer locations. Once the samples were tested, the gauge section of the tensile specimen was removed from the grips and mounted in a conductive graphite-based powder with a Bueher Pneumet I hot mounting press. This produced two mounts for each tensile specimen. After mounting, each sample was polished incrementally using SiC paper with increasing mesh numbers of #240 to #800. The remaining fine polishing was performed with felt pads and DiaLube diamond suspensions of 6-micron followed by an attack polish. Before each fine polishing step, the samples were ultrasonically cleaned with deionized water. The samples were then etched by immersion with Kroll's Reagent (2% HF, 6% HNO_3, and 92% water) for 7 seconds. After etching, the prepared surfaces were examined via Optical Microscopy (OM) and Scanning Electron Microscopy (SEM); three micrographs were obtained for each area of interest.

At room temperature Ti6Al4V is a α/β titanium alloy with stable alpha and beta phases. When the melt pool solidifies in EBM printing of Ti6Al4V, it forms β grains. Once the initial beta grains cool to the beta transus, around 980°C, they initially transform into the martensitic alpha prime phase, however, since EBM materials are preheated to around 650°C the martensitic phase should transform into a lamellar alpha/beta with beta ribs within an alpha matrix [48]. During the initial cooling from the melt to the beta transus temperature, the beta grain coarsens. The prior beta width is a primary contributor to the anisotropy of AM Ti6Al4V and as such the evaluation involved measurement of prior beta grain dimensions. In order to accurately measure the α lath thickness, SEM images were taken at 2500x. Three images were obtained for each area of interest

and a 35 µm by 40 µm window of evaluation was analyzed. An image processor was used to evaluate α lath thickness according to Sears et al, [49] .

4.3.3 *MicroCT Analysis*

The porosity and its distribution within selected tensile samples were evaluated after tensile testing to failure using X-Ray Computed Microtomography (µCT). The evaluations were performed using a commercial system (X5000, North Star Imaging, Rogers, MN, USA). The scan parameters used for all specimens are listed in Table 4.3. Projections were first reconstructed in a commercial software (efX CT) that is provided by the manufacturer of the µCT scanner. This software embedded the geometric data from the geometry tool that was scanned after the specimen. Once reconstructed, the volume is then exported as a slice stack along the build height direction. The image stack was then imported to VGSTUDIO MAX (Volume Graphics Inc., Charlotte, NC, USA) for porosity calculations.

Table 4.3. X-Ray Computed Microtomography scan parameters used for all specimens scanned.

Scan Parameter	
Voltage	140 kV
Current	87 µA
Geometric zoom	17.5X
Projections	1200
Scan mode	Step
Frame average	2 frames/projection
Frames per second	1 fps
Gain maps	7

Resolution	10.97 µm
Filter	0.005 in. brass

4.3.4 *Fractography*

A fractographic analysis was performed post-failure using optical microscopy. Optical microscopy (OM) was performed on an Olympus Model SZX16 stereomicroscope for quantitative determination of the fracture area occupied by LOF defects.

4.4 RESULTS

4.4.1 *Regression Analysis*

Results from the regression analysis for the elastic modulus (E), yield strength (YS), ultimate tensile strength (UTS), and elongation at failure (%el) are shown in Figure 4.2. Specifically, the graphs present the relative percentage contribution of the main factors, their linear interactions, and quadratic factors on the yield strength and strain at failure. A pareto effects chart is useful to identify which factors are most influential and had significant effects on the dependent variable. For example, in the pareto plot shown for YS in Figure 4.2b, the relative contribution and strength of the factors is shown. Values that exceed the threshold shown by the red dashed line are significant. Considering factor interactions, H*T is the designation for the interaction effect of the height and thickness factors and has the largest and most significant influence on the YS.

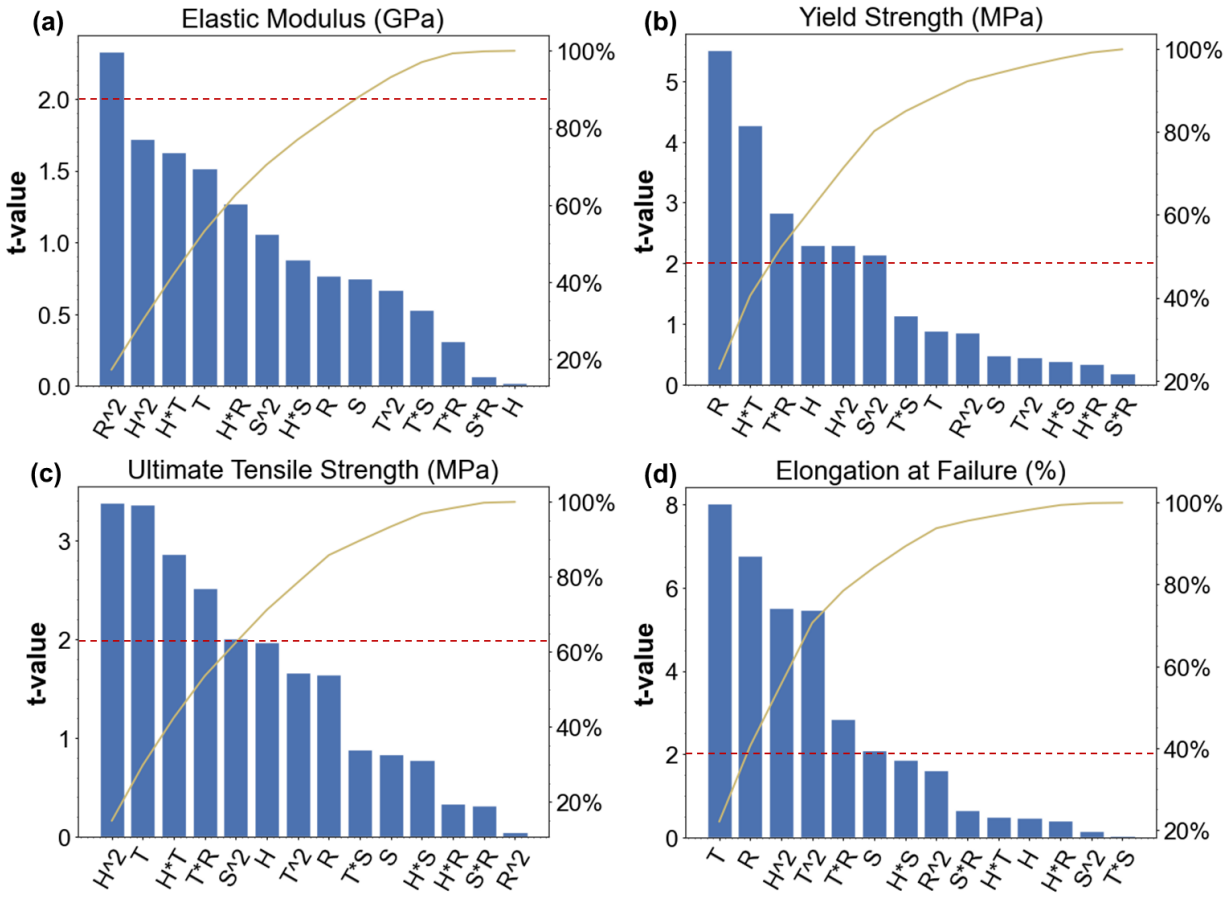

Figure 4.2. Pareto charts with cumulative percentage effects of the regression model variables for (a) Elastic Modulus, (b) Yield Strength, (c) Ultimate Tensile Strength, and (d) Elongation at Failure. The red dashed line on each chart represents the critical t-value at which the effect of the factor is statistically significant based on α=0.95.

The contribution of the main effects to the mechanical properties are shown in Figure 4.3. As evident in Figure 4.3b, the radial distance of the build from the center of the build plate was most important to the YS. The average YS increased with radial distance, with an approximate increase of nearly 4 % from the center of the build plate to the build envelope boundary. There were limited changes in the YS over the range in height, thickness and part spacing. Regarding

the %el, the effects of thickness and radial distance were most important, with the thickness exhibiting a significant non-linear relationship. In general, there is increase in %el with part thickness (Figure 4.3d), with an increase from 6.7±2.3 % to roughly 11% This response is a significant main effect with quadratic dependence on part thickness. Over the range in build parameters explored, the optimum part thickness to maximize the ductility is ~5-5.5 mm. In comparison to the effects of the other parameters, part spacing had negligible effects on nearly all the mechanical properties evaluated.

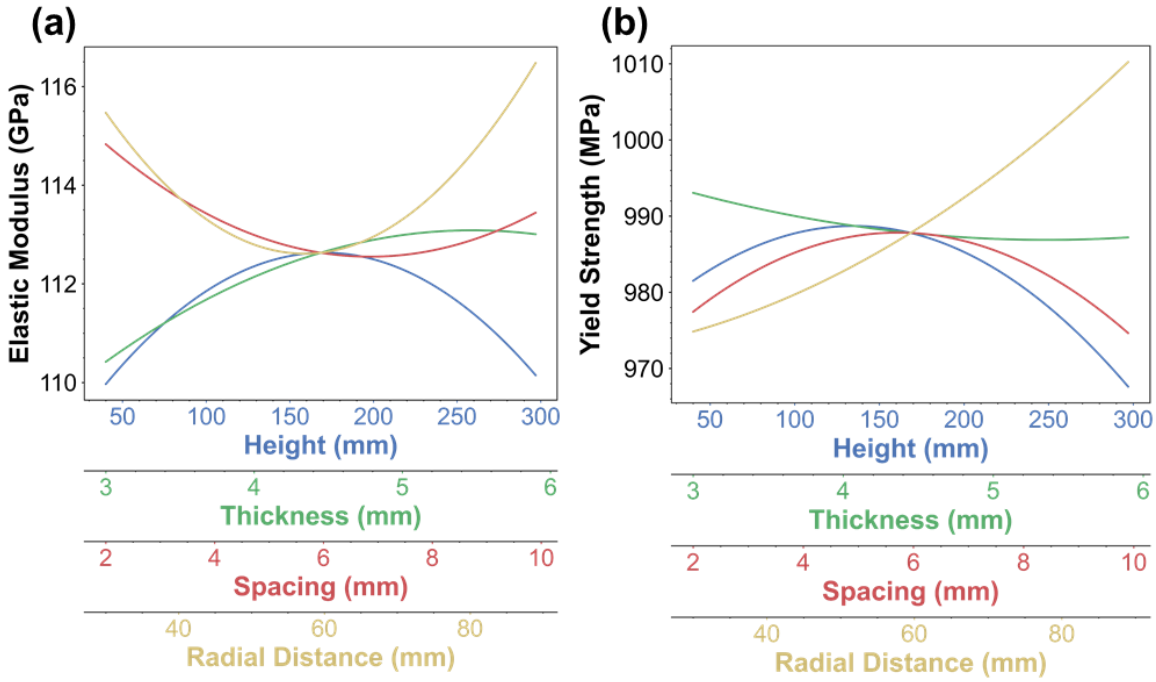

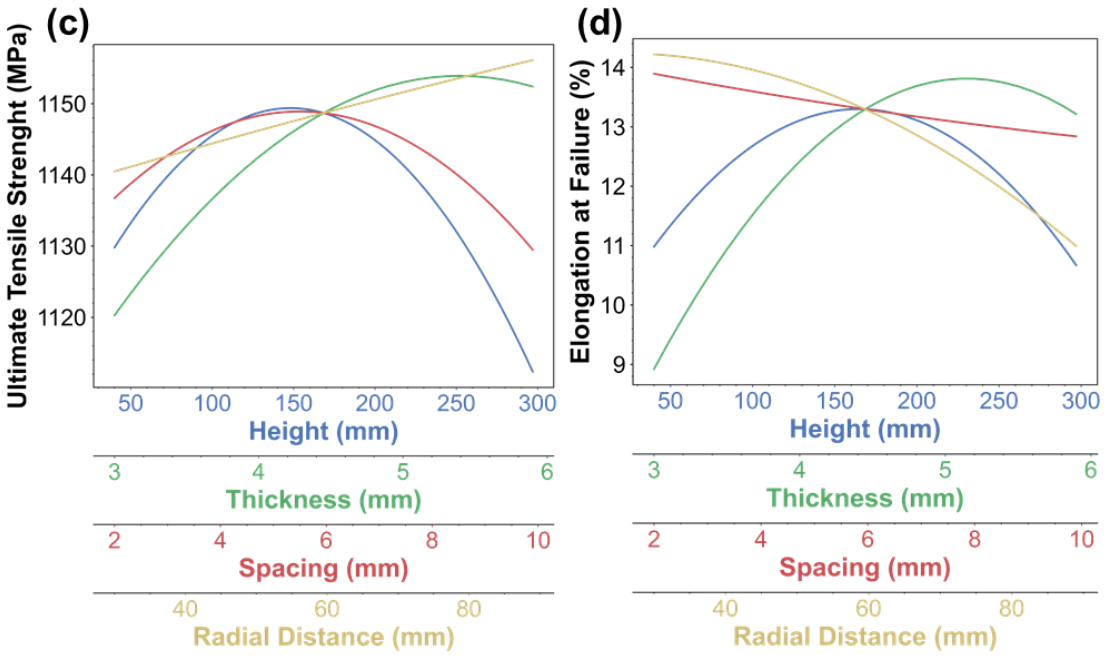

Figure 4.3. Main effect plots for each of the factors for the (a) Elastic Modulus, (b) Yield Strength, (c) Ultimate Tensile Strength, and (d) Elongation at Failure. The lines correspond to the regression model with the other factors held at their middle level.

Contour plots are useful in understanding the relative influence of main factors when varying another factor, thereby identifying which factor levels are the most appropriate to optimize the mechanical properties. Contour plots for all factor interactions for the vertical oriented specimen toughness are shown in Figure 4.4. In the contour plots it is possible to obtain general guidelines for the selection of parameters to maximize the toughness of vertically oriented components. Considering the responses involving thickness, it is clear that the toughness increases with part thickness regardless of what other factors are involved, with a peak toughness achieved with thickness between 5 and 6 mm. Based on data from the vertical build there appears to be an optimal height to maximize toughness, which is between 80 and 160 mm. This is consistent with the maximum toughness in the interaction of height with the other factors. Part spacing did not

have a strong effect on the toughness. Nevertheless, the contour plots demonstrate that the largest toughness was obtained with the lowest spacing. The contour plots also convey the benefit of placing parts closer to the center of the build plate to maximize toughness. Nevertheless, at sufficiently low thickness, the radial position does not have substantial influence on the part toughness. Overall, data from the vertically oriented build indicates that the maximum toughness can be achieved with thick parts located near the center and bottom of the build volume and with small distances between adjacent parts (i.e., high packing density of parts).

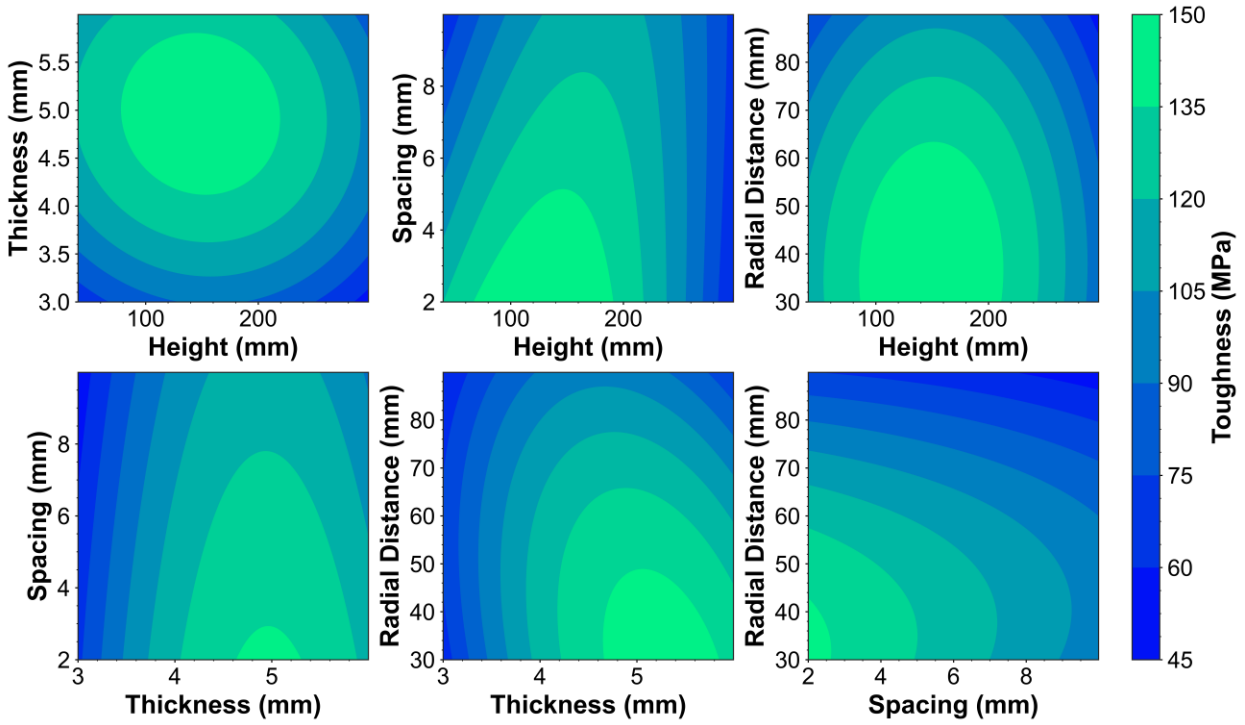

Figure 4.4. Contour plots for the metal toughness based on two factor interactions. For each plot, the other two factors that are not labeled on the x- or y-axis are held at the middle level. For example, in the top left contour plot spacing is held at 6 mm and radial distance is held at 60 mm

Figure 4.5 presents a comparison of the main and quadratic effects on the metal toughness in the two build orientations. Toughness is selected as the response of interest when comparing vertical and horizontal parts as it is a key performance metric for titanium alloys in aerospace applications and it depends on both the strength and ductility of the metal. Differences in the main effects on toughness are apparent for the two orientations of specimens, particularly in the effects of height. Height serves as significant main and quadratic effect on the toughness for the vertical orientation, whereas height has non-significant effect for the metal with horizontal orientation. Thickness exhibits a similar trend for both orientations, i.e. a large increase between the low and middle levels and a parabolic taper to the high level. The quadratic effect of thickness on toughness is more pronounced in the vertical orientation than the horizontal orientation. Also evident in Figure 4.5, spacing influences the two orientations equally. The effects of radial distance are difficult to compare between the two build orientations as the range in this factor is very different for the two orientations; the vertical specimens spanned 30-90 mm, whereas the horizontal specimens spanned 7-111 mm. The horizontal build had specimens that were nearly at the center axis of the build chamber (Fig. 4.1d and Table 4.1). Nevertheless, the results provide an understanding of the effects from radial placement over the available build envelope for both orientations of metal. For the toughness, there were no significant effects from radial distance on the metal with horizontal orientation.

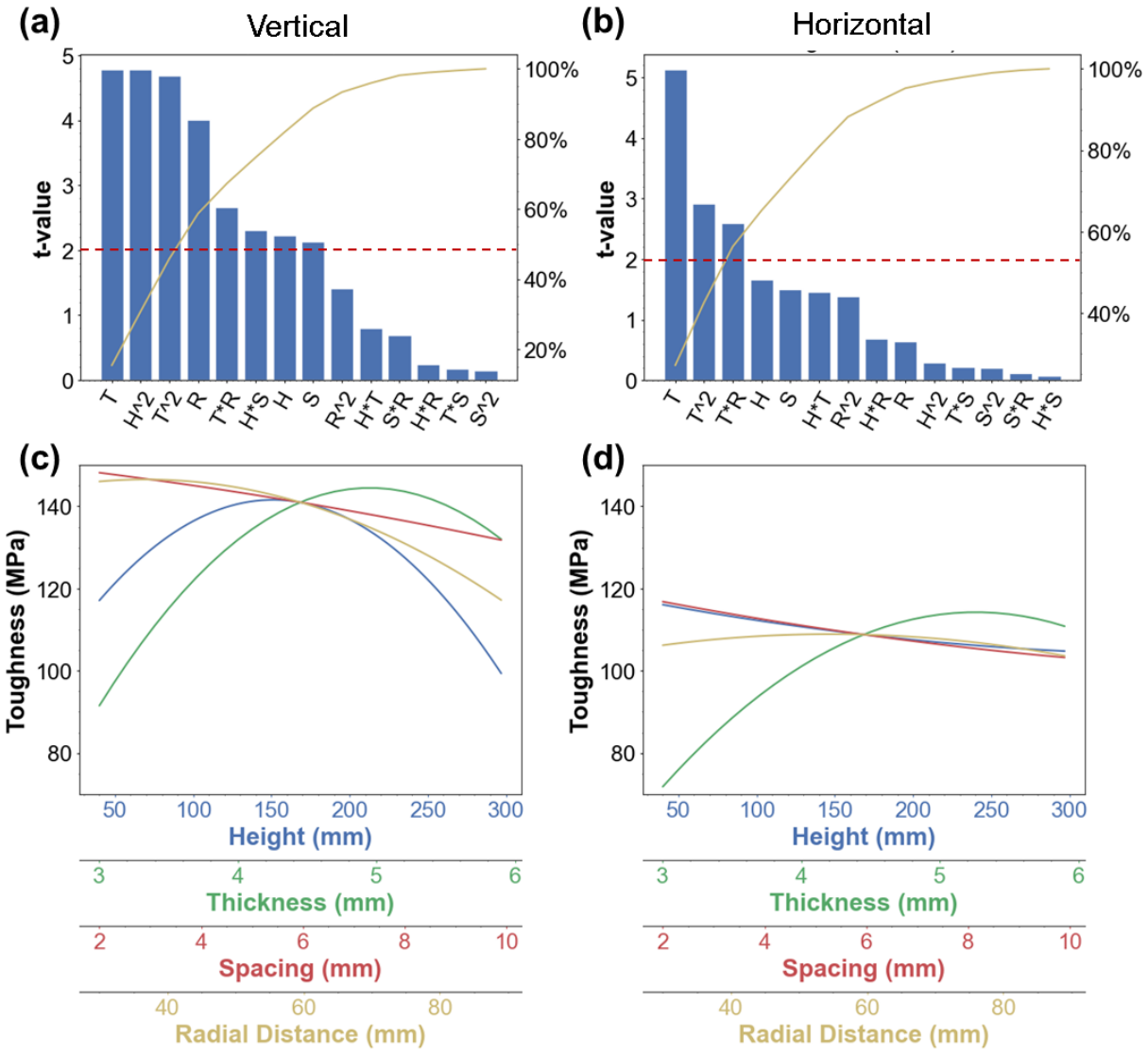

Figure 4.5. Comparison of the regression models derived from the vertical and horizontal builds. (a) and (b) are the pareto charts for relative influence of regression model components for vertical and horizontal, respectively. (c) and (d) are the main effect plots for vertical and horizontal, respectively. Thickness was the most significant parameter for both orientations.

4.4.2 *Microstructure*

Metallographic analysis showed that the microstructure was dependent on the build design parameters. For alpha lath thickness, Figure 4.6 shows micrographs of two exemplary microstructures. Specifically, Figure 4.6a and 4.6b present metal with fine alpha lath and coarse alpha laths, respectively. The alpha lath thickness ranged from 0.34 to 0.69 µm across all specimens assessed in both orientations.

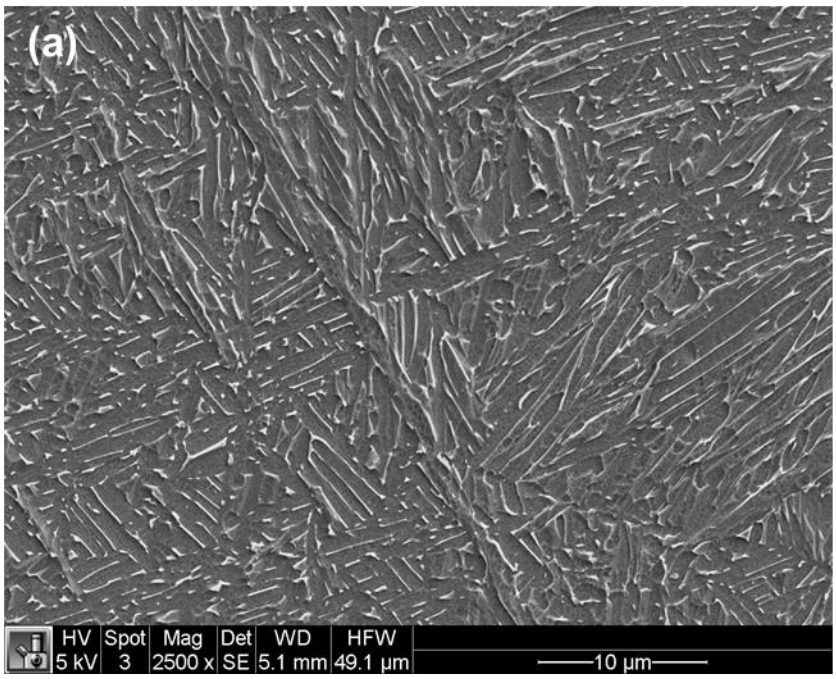

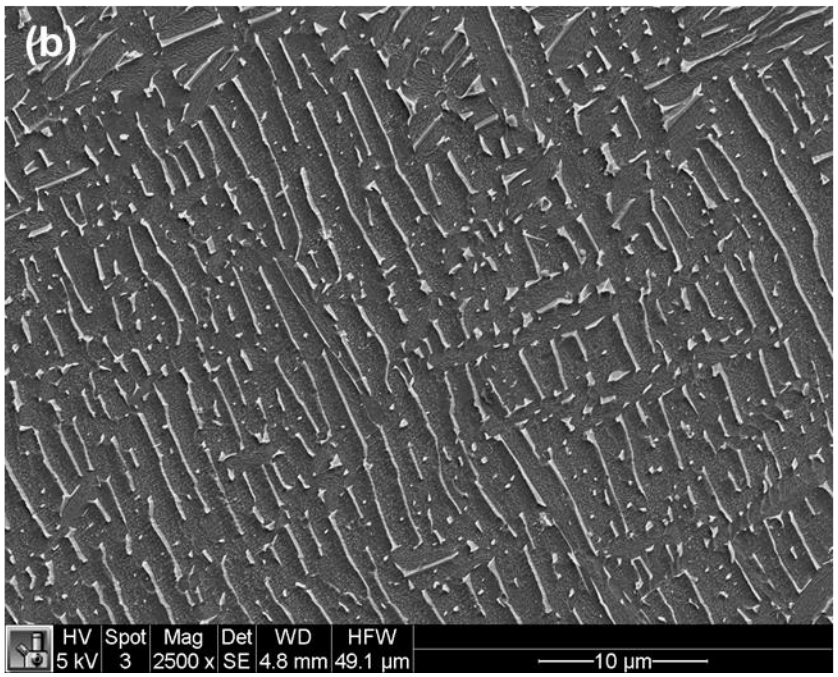

Figure 4.6. SEM images of Ti6Al4V microstructure. Dark grey regions are the alpha phase and light grey is the beta phase. (a) Representative fine alpha lath structure found in samples with high yield strength. Factor levels (H; Height, T; Thickness, S; Spacing, and R; Radial Distance) are listed to the right of the micrographs, along with alpha lath thickness (α_t) and yield strength (σ_{ys}). (b) Representative coarse alpha lath microstructure for samples that have lower yield strength.

Utilizing multiple regression with the alpha lath data, the relative impact of the design parameters is presented in Figure 4.7. For vertical specimens (Figure 4.7a), the strongest trends were related to the height and radial distance factors, indicated by the large range covered by the two factors. Height resulted in an inverse quadratic trend with a maximum near the middle level, whereas there was a near linear decrease in alpha lath from the center of the build to the exterior of the build plane with radial distance. Thickness appears to have a positive correlation with alpha

lath thickness, where a linear increase in alpha lath thickness with thickness is present. Spacing appears to exhibit a minor positive quadratic effect on the microstructure of the metal in the vertical orientation.

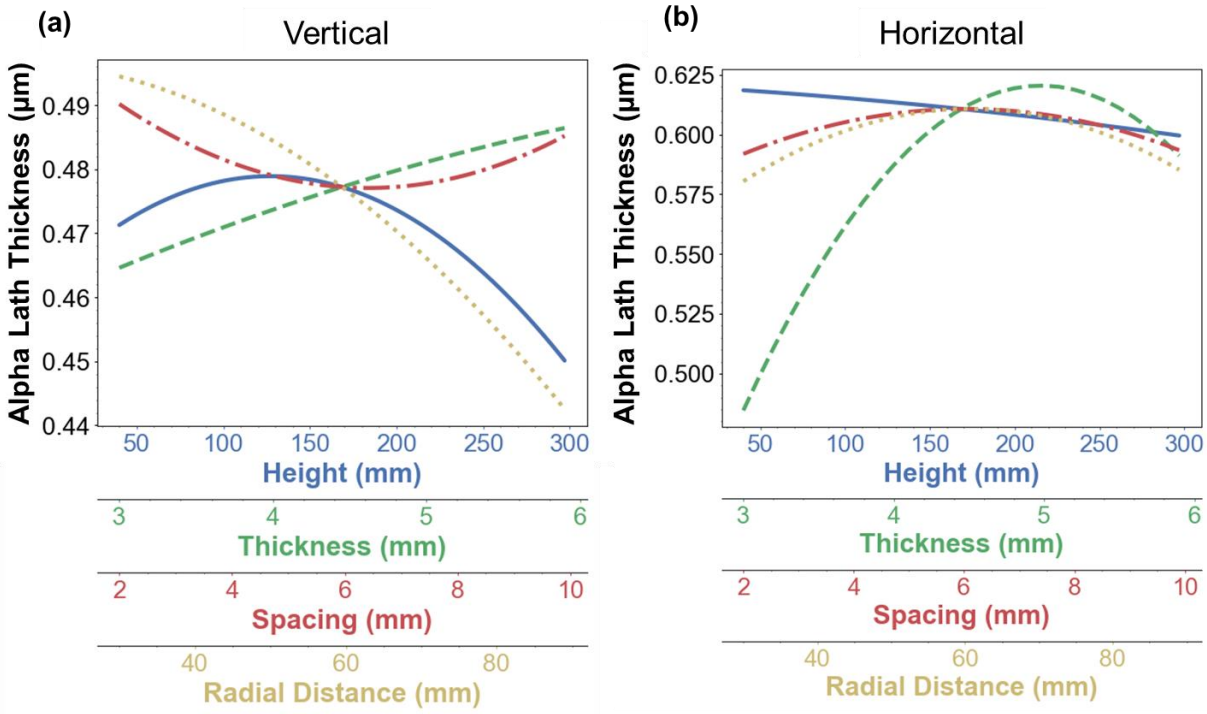

Figure 4.7. Main effect plots for the multiple regression models of the alpha lath thickness for the (a) vertical and (b) horizontal oriented builds.

In comparison, the alpha lath thickness for the horizontal build (Figure 4.7b) was influenced by thickness more than for the vertical orientation, with thicker specimens having significantly greater alpha lath thickness. The effects of radial distance for the horizontal orientation exhibit a quadratic trend with specimens near the center and edge of the build plane having the finest alpha laths. The influence of height is reflected by a linear decrease in alpha lath

thickness with increasing distance from the build plate. Finally, the effects of spacing is not significant on the alpha lath thickness.

4.4.3 *Defect Analysis*

Several representative specimens from the vertical build were scanned using µCT. The purpose of this effort was to assess the porosity in terms of volume fraction, size distribution of pores, their location and morphology. A reconstructed model for a 6 mm thick specimen is shown in Figure 4.8a. The specimens were subjected to tensile testing prior to scanning, which allowed the two halves of the gauge section to fit in the span of the detector and achieve higher scan resolution. Sixteen specimens were evaluated, corresponding to the low, mid, and high levels for all of the vertical build factors except for radial distance, which included only the low and high levels. The trends were modeled using second degree polynomials, except for the radial distance.

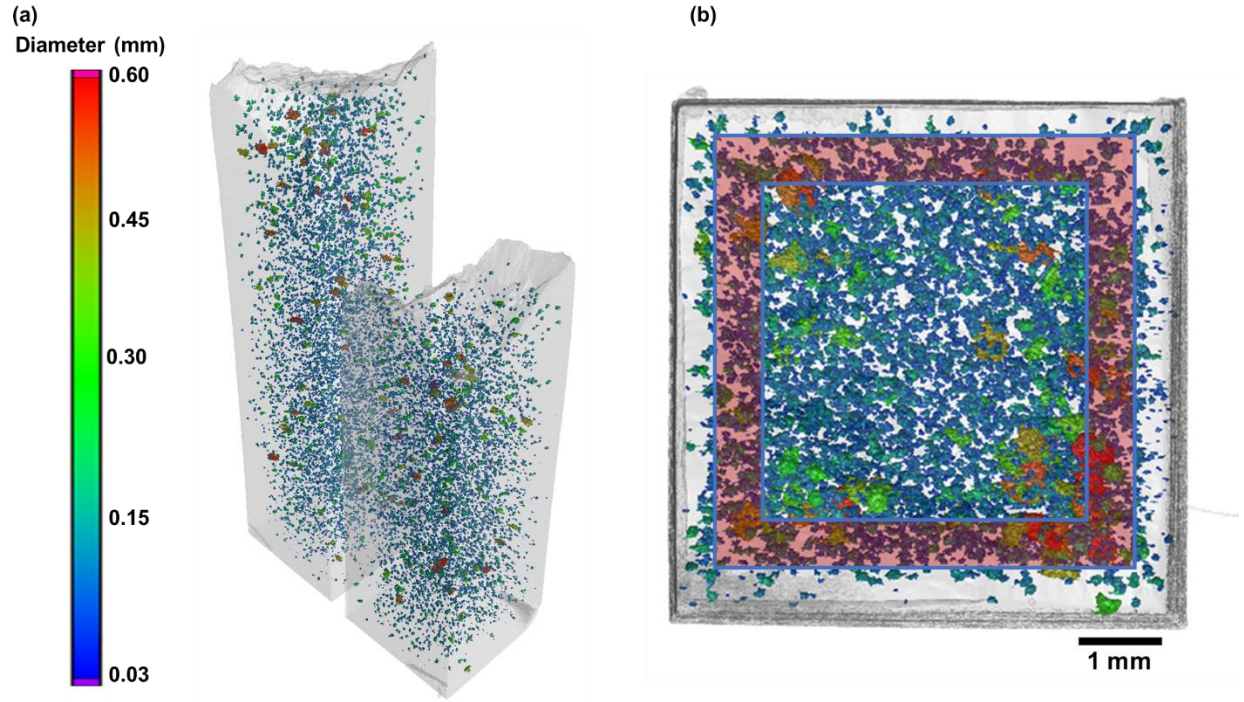

Figure 4.8. 3D reconstruction of a 6 mm thick vertically oriented specimen after tensile testing. The color bar indicates the diameter of the pores shown in the (a) oblique view and (b) top-down parallel view. The red translucent box in (b) indicates the region at which the peak density of pores is located.

Volumetric porosity is a common metric designated for determining the overall porosity within metal AM parts. The highest porosity was 0.84 % and identified in a 6 mm thick specimen, which is approximately 4X the lowest value of volumetric porosity in the 3 mm thick vertical tensile specimens (0.20 %). The average volumetric porosity for all the 6 mm thick specimens evaluated (0.54±0.14 %) was significantly higher than that of the 3 mm specimens (0.24±0.05 %).

With regards to the spatial distribution of pores, the probability density plots in Figure 4.9 show that the pores within the gauge sections of the vertical build exhibited dependence on part thickness. Edge distance is defined as the distance from the center of a pore to the closest free surface. The thin specimens (3 mm thickness) exhibited no consistent trend in pore distribution with edge distance, though there appears to be a strong peak density of pores 0.25 mm from the surface of the part (Figure 4.9a). For the 4.5 (Figure 4.9b) and 6 mm (Figure 4.9c) thickness, there is a large increase in pore density radially inward from the free edge of the part, with peak density around 0.3 – 0.8 mm, followed by a steady decrease toward the center axis of the part.

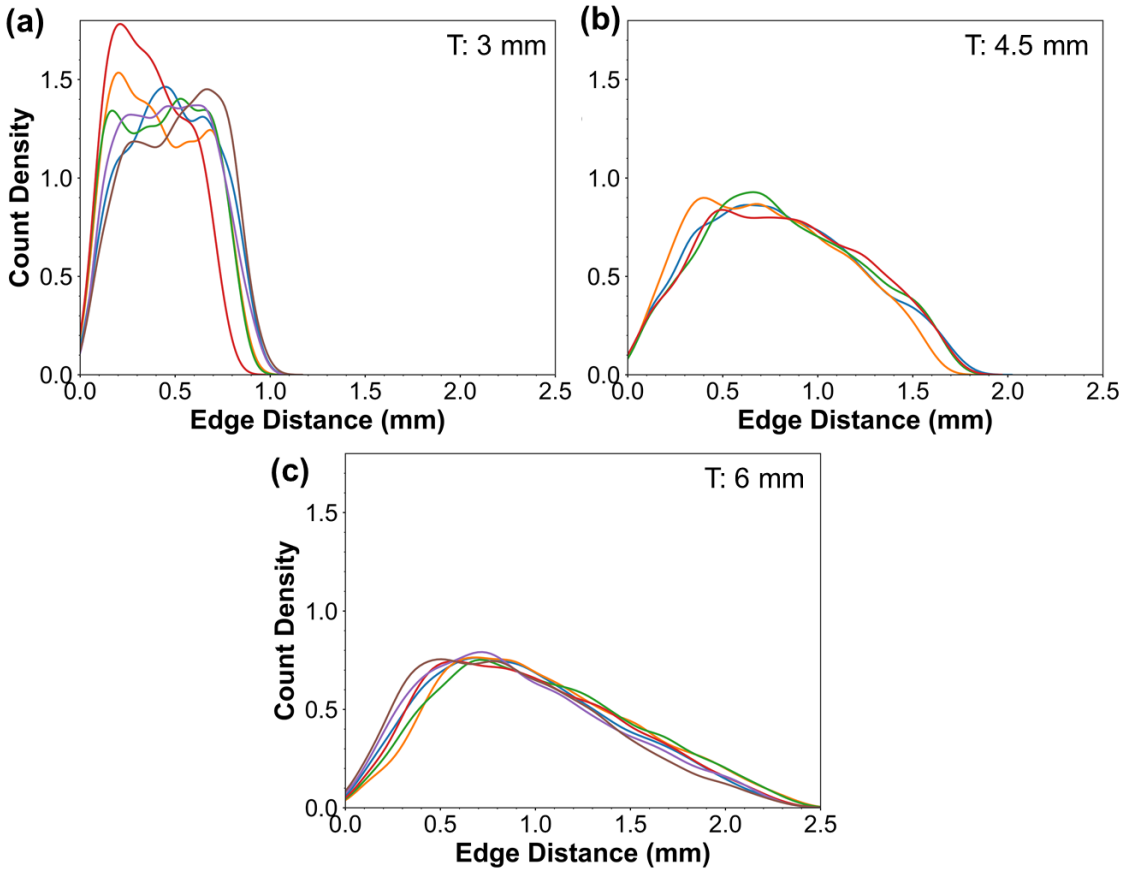

Figure 4.9. Kernel density plots of the radial locations of pores for vertically oriented specimens that were scanned with X-Ray µCT. Specimens are grouped by the thickness factor: (a) 3 mm, (b) 4.5 mm, (c) 6 mm.

Regarding the main factor effects on porosity, there are strong correlations between the parameters and the largest pores, as shown in Figure 4.10. In regard to the influence of height, there is a strong quadratic effect with largest pores located towards the bottom and top of the build envelop. The effects of all other parameters on the pore size were linear, with increases in the size of the largest pores with increasing thickness and increasing radial distance. The effects of spacing were also linear, however the effect of spacing was not significant regression model.

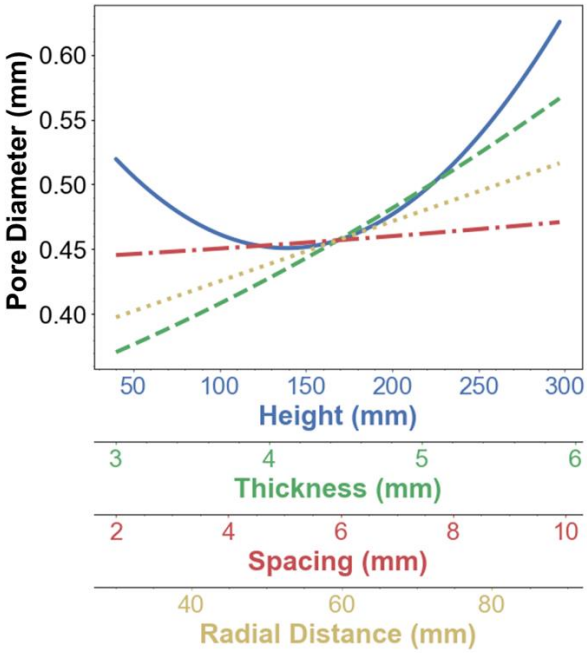

Figure 4.10. The effect of the (a) Height, (b) Thickness, (c) Spacing, and (d) Radial Distance on the largest pores defined by diameter in the vertically oriented specimens.

4.5 DISCUSSION

For metal AM processes to advance, a more thorough understanding of the influence of beam characteristics, feedstock material, and build space parameters on the metal quality is needed [11,14,100]. The present investigation was focused on the contribution of build space parameters to metal quality in EBM. Considered in this effort were the location, size, and relative spacing of the parts as they are relevant considerations to both the design and manufacturing process.

Part position within the build space was identified to be a significant factor to the mechanical properties of the metal. Starting with height, the distance of the parts from the build plate had a significant effect on the metal for the vertical orientation only. That translates to

variations in microstructure within a part as a function of height and cross-sectional area of the component or differences in the same part when placed at different heights in the same build [18,101]. The height dependence is a result of reduced cooling rate for material further from the build plate, which has also been identified in SLM of titanium [102] and with other materials [103]. For the mechanical properties of the vertical specimen orientation there is an inverse parabolic dependence on height. However, the analysis of the microstructure for the vertical orientation shows a negative parabolic trend across the same range in build height, i.e., a coarsened alpha lath structure near the intermediate height in comparison to the metal below and above. That is not consistent with the trend expected for the mechanical properties as strength generally decreases with increasing alpha lath thickness [104,105]. Fractographic analysis of the fracture surfaces, such as Figure 4.11, showed that large LOF voids can occur within these specimens. Occupying a substantial portion of the cross-sectional area (up to 6.5 %), these LOF defects reduce the load bearing material and consequently reduced the measured yield strength. Larger defects at the low and high height levels is responsible for the decrease in yield strength and overshadows the influence of the fine alpha laths at these same height levels. In comparison to the parametric effect for the vertical orientation, the porosity has negligible effects on the mechanical properties for the horizontal orientation and there is no significant effect of height on the mechanical properties for this orientation.

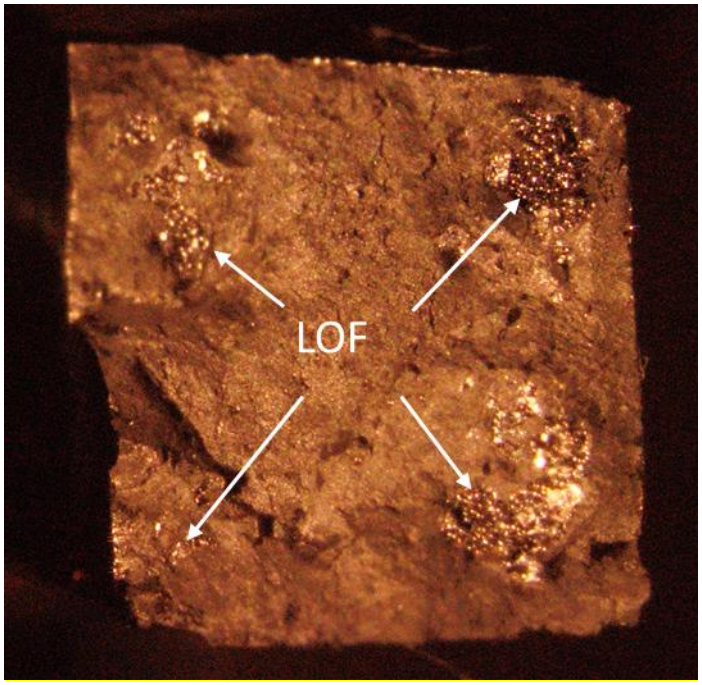

Figure 4.11. Stereomicrograph of an exemplar vertically oriented specimen with lack of fusion (LOF) defects indicated.

The next factor of consideration is the radial distance, which had significant effect on the mechanical properties. Specifically, the elongation at failure and toughness of the metal with vertical orientation decreased significantly with increasing radial distances. However, both the YS and UTS increased significantly with radial distance. Due to the contribution of grain boundary strengthening, the fine alpha lath thickness increased the YS [106] of the metal with radial distance, following the Hall-Petch relationship:

$$\sigma_{YS} = \sigma_0 + k_Y / d^{0.5} \tag{4.1}$$

where σ_0 and k_Y are material constants representing the initial stress to instigate dislocation slip and strengthening coefficient, respectively. For alpha-beta titanium alloys like Ti6Al4V, the effective grain size parameter (d) is the alpha lath thickness.

Comparing results of the present research to reported data from other studies, the experimental data conforms to the Hall-Petch relationships for AM of Ti6Al4V (Figure 4.11). Admittedly, there is considerable spread in the data obtained from the experimental studies. For example, a recent study attempting to establish correlations between the microstructure and mechanical properties of SLM Ti6Al4V showed a Hall-Petch relationship that was not consistent with the reported trends [107]. The samples in that study were heat treated for stress relief and decomposition of the martensitic alpha prime phase in the microstructure, clarifying that the discrepancy in the data is not caused from residual martensite.

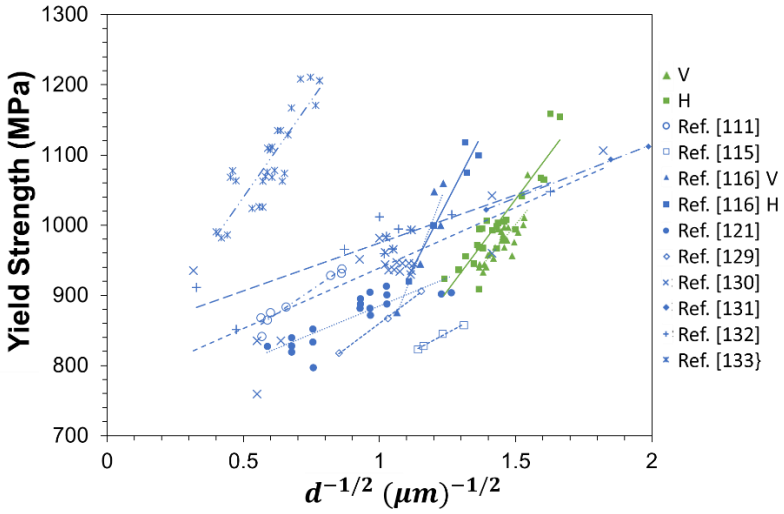

Figure 4.12. Hall-Petch relationships comparing literature data against the data from this investigation (green data points) [60,94,97,104,107–111].

For parts located near the edge of the build envelope, the wall of the build chamber serves as a heat sink. They are also further from the center of the build plate. These two heat fluxes produce an increased cooling rate with increasing radial distance, which directly contributes to the radial dependence in the microstructure. Indeed, the strength variation with

radial distance should coincide with a decrease in the alpha lath thickness [104], which is a result of the faster cooling rates with radial distance. That causes the reduction in alpha lath thickness with radial distance as shown in Figure 4.7a. Based on the reported thermal gradient in an investigation involving EBM, it was found that a strong radial thermal gradient (Δ = 70 °C) is possible [112], which can lead to mechanical property changes with radial distance [113], which were found in the present data.

Part thickness also had a significant effect on the mechanical properties for both build orientations. At least for the vertical orientation, this dependence appears related to the internal porosity and its distribution. For this orientation the large lack of fusion pores are oriented in the build plane and perpendicular to the loading direction. While near the surface of the sample there are few pores, the density of pores increases to a maximum approximately 0.3-0.8 mm away from the edge. Many of these pores have large diameter, as evident in Figure 4.9b (pores highlighted as orange and red). A high concentration of pores in close proximity to one another can act as a distributed stress concentration [83] further exacerbating the issue of porosity in a single layer. Also, pores located close to the surface of the part have higher effective stress concentration due to the free surface interaction and their synergism with surface-related notches [82]. Of note, there is greater volumetric porosity with increasing specimen thickness. For Ti6Al4V and other metals built with AM processes, the ductility decreases with increasing volumetric porosity [114,115]. The detrimental effect of porosity density to the %el is further established in Figure 4.12b. Fractographic inspection supported calculation of the fracture surface area that is comprised of defects, which showed a linear relationship with %el. While the percentage of pore area is a strong predictor of reduced strength and ductility, there is a need for a metric that correlates well with uCT data. One metric that shown to correlate with the %el is the diameter of extreme size pores

[116], which are the largest pores residing in the material. As expected, there was a decrease in %el with increasing size of the largest pores in the printed metal. The size of pore was normalized by the specimen thickness to account for the reduced cross-sectional area; the specimen width was constant).

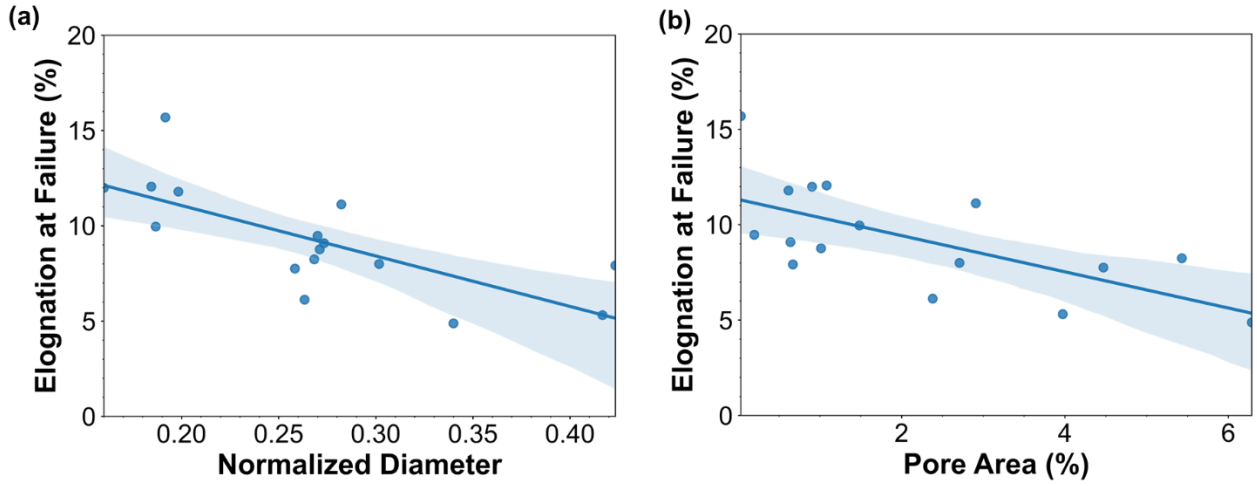

Figure 4.13. Elongation at failure as a function of both the (a) normalized diameter of pores found through µCT, and (b) percent area that pores occupied on the fracture surface of vertically oriented specimens. A linear fit is applied with a confidence interval of 95% for the shaded area.

Regarding the importance of component spacing in the build space, there was limited effect of this parameter on most performance metrics for both the vertical and horizontal part orientation. That finding is consistent with previous reports for AM of steel [99]. A closer proximity of components could serve as adjacent thermal masses that result in slower cooling rates and prolonged time at elevated temperature that cause alpha lath coarsening [117]. However, the partially sintered powder is a poor conductor of heat and may not effectively transfer heat between adjacent parts that are at elevated temperatures.

A 3D spatial property map for toughness of the metal with vertical oriented components is shown in Figure 4.13. This map is presented for largest component thickness and smallest spacing. A map of this type can serve as an effective tool that supports discussions between design and manufacturing engineers concerning build layout and part properties. Following the color gradient, it is easy to determine where within the build chamber to place parts for maximum tensile toughness. As evident from this property map, the optimal placement of components would be in the center of the build plane (radial distance) and near the center along the build direction (height). Conversely, the components should not be built in in the top corners of the build volume.

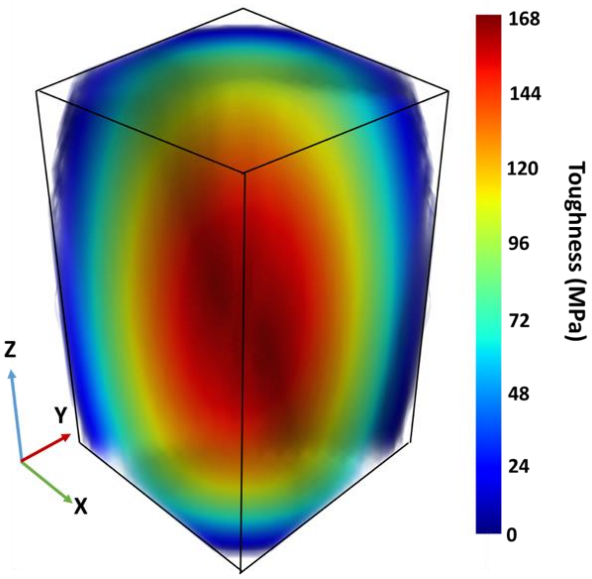

Figure 4.14. 3D spatial map for toughness of vertical oriented parts, with the black box indicating the full build volume. Thickness is held at 6 mm and spacing held at 2 mm.

Despite the value of the property map, further improvement of the experimental design could increase the accuracy of the model and its applicability. For example, the builds were designed to encompass many variables and required a compromise on factors that would support

modelling the response over the build volume. Part spacing was included as a factor, but there was limited effect of this parameter in the responses. It could be removed in a subsequent build to involve more radial spacing or height levels. Furthermore, due to the limitation of using only three levels for height and radial distance, the models required an interpolation of data over a large distance of the build space. The property map in Figure 4.13 exemplifies this issue associated with insufficient data to support extrapolation of the model. The corners of the build volume have negligible toughness according to the model, which is a result of not having sufficient data for those regions. Having metal placed at the most extreme positions of the build space could provide the necessary data for the regression model to accurately reflect the toughness in these regions. Future studies should consider encompassing more of the build volume, and with more specimens, to map the space more thoroughly. Clearly, further diligence is needed to ensure that variations in model responses are not introduced from higher part density, interconnected parts, different support structures, etc. Nevertheless, models of this type can provide the foundation for optimizing the design and manufacturing of Ti6Al4V parts obtained by EBM.

4.6 CONCLUSIONS

To address an area of the AM process by EBM that is often neglected, a design of experiments was performed to investigate the influence of part design and build space parameters on the microstructure and mechanical behavior of Grade 5 Ti6Al4V. The influence of height (distance from the build plate), part thickness, part spacing, and radial distance of parts from the center of the build plate were investigated. Two separate sets of experiments were performed for the vertical and horizontal part orientations in the build space. An evaluation of the metal microstructure and

defects was performed on selected parts and for various factor levels to understand the process-to-performance relationships. The findings showed:

1. In general, the part thickness and radial distance from the center of the build plate had the most significant effects on the strength, elongation at failure and resulting toughness responses. These two factors are important because they control the part cooling rate and the heat accumulated during the post heating phase of the build. The part spacing was found to have limited effect on the mechanical responses.

2. Defects in the vertical specimens consisting of lack of fusion (LOF) voids were a key factor contribution to the distribution in mechanical properties observed. Large LOF defects were present in all samples scanned with μCT and were detrimental to both the elongation at failure and toughness.

3. Using the models developed from data of both orientation builds, an understanding of the parametric conditions were identified for maximizing the mechanical properties of the metal. This information, along with the visual guides can be used for smart Design for Electron Beam Melting (DFEBM) AM.

Chapter 5. VARIABILITY OF FATIGUE PERFORMANCE DUE TO BUILD DESIGN PARAMETERS IN ADDITIVELY MANUFACTURED TI6AL4V

5.1 SYNOPSIS

Fatigue strength is an important mechanical property for additively manufactured (AM) Ti6Al4V. Utilizing a design of experiments (DOE) approach, the effect of several design parameters on fatigue life were investigated that encompassed part geometry and location within the build envelope. The effects of the build design parameters were investigated for both the as-built and machined surface conditions. In both conditions the fatigue life decreased significantly with decreasing part thickness and increasing radial distance. Location along the build direction (height) had no significant effect on the machined condition. The as-built surface posed stress concentrations that facilitated fatigue cracking and failure at a significantly lower cycles than parts with a machined surface condition. For the as-built condition cracks always initiated at the surface, whereas a mix of origins were identified for the machined condition, including clusters of internal lack of fusion (LOF) defects, LOF defects exposed to the surface, and rogue defects, which were extreme pores present in small thickness parts occupying >10% of the cross-sectional area. Pore characteristics, such as size, location in a part, and morphology were determined by x-ray micro-computed tomography (XCT). Incorporating porosity into the regression models resulting in more accurate prediction of the fatigue life. Results showed that the best fatigue performance can be obtained when the parts are printed with sufficient thickness and near the center of the build plane to avoid detrimental porosity. Further improvement is achieved by machining the surface to a depth

that does not expose underlying porosity. These guidelines are critical for industrial users to understand to produce high quality metal for mission-critical fatigue applications.

5.2 INTRODUCTION

Ti6Al4V is an alpha-beta alloy that is considered the workhorse titanium alloy of the aerospace industry. Commonly employed in applications where loading is cyclic, the fatigue performance is a quality of critical importance for this alloy. Conventional manufacturing methods, specifically wrought forming, is concerned the standard for achieving exceptional fatigue performance for this alloy. Considering the progressive advancement of additively manufacturing (AM) in aerospace the fatigue performance of AM parts of Ti6Al4V has become a topic of concern. The importance of fatigue and potential contribution of intrinsic defects resulting from AM processing of Ti6Al4V has motivated extensive research into the subject. In fact, reviews of high cycle fatigue (HCF) life for powder bed fusion (PBF) are becoming available [36,118–122].

There are specific factors of concern in PBF that could affect the fatigue performance of components, including their orientation in the build and surface finish [36]. The surface finish of AM parts, particularly the rough surfaces associated with PBF, is particularly detrimental. Sharp notches inherent of the surface, due to unmelted and irregularly spread powder, leads to premature fatigue crack initiation on the surface [83,123,124]. Thus, machining of the surface to eliminate the notch effects is seen to significantly improve cycles to failure in AM of Ti6Al4V.

Component orientation is the second major factor contributing to the fatigue performance of AM components. Components with vertical orientation are generally considered inferior to those with horizontal orientation [36,119]. The underlying cause for orientation dependence in fatigue performance are microstructure, defects and their distributions [36]. Internal defects are

detrimental to fatigue life due to their stress concentration and are more problematic in parts printed with vertical orientation (along the build direction). The major axis lack of fusion (LOF) voids in AM parts is typically within the build plane, which results in the largest dimension oriented perpendicular to the axis and maximum normal stress. The largest pores (largest in the metal volume) tend to be a result of incomplete fusion between layers [33]. As such, the stress concentration posed by these pores is of greater importance than other microstructural features and leads to the discrepancy between vertical and horizontally printed parts [119]. Internal defects are a significant concern motivating research and the development of predictive models capable of relating the defect characteristics to the fatigue properties [69,125–127]. While the physical size of these voids is commonly considered to be the dominant attribute [128], there are other characteristics that should be considered. Namely, shape [82], the location relative to the surface [69,129], and location relative to other pores/defects [83] are relevant. Each of the aforementioned characteristics can influence the stress concentration posed by a pore.

Key to developing high quality metal with AM is understanding the property variability and which process parameters that potentially compromise the performance. Extending beyond machine parameters, build design parameters are an often-ignored parameter space that must be considered. For instance, part placement within the build space and its geometry were found to have significant effects on the mechanical properties in quasi-static tension loading. Similarly, these build design parameters are expected to have comparable effects on the HCF response due to trends in porosity across factor levels. However, few studies have investigated the effects of build design parameters on the fatigue performance of Ti6Al4V or other metals. In a study concerning the fatigue response of Ti6Al4V and the contribution of specimen thickness it was reported that fatigue life increased with component thickness [130]. This dependence was due to

the less detrimental surface defects on the thicker specimens, which reduced the incidence of crack initiation from the surface. Furthermore, the alpha lath thickness increased with part thickness, which also increased the crack growth resistance [118]. A related study reported a similar trend with geometry and the as-built fatigue life, noting a higher surface roughness with reduction in component thickness [123]. Neither of these aforementioned studies considered the effects of component geometry in the machined state, or after post-processing surface treatment. Components intended for critical applications will typically receive surface treatments to mitigate the effects of the surface. Hence, there is need to further investigate build design effects, such as geometry and location on fatigue performance of EBM of Ti6Al4V.

5.3 Materials and Methods

5.3.1 *Powder Feedstock*

The powder used in this study consisted of Grade 5 Titanium alloy (Ti6Al4V), acquired from the EBM manufacturer (ARCAM: Batch P1143, Part #430944). The powder has undergone a couple build cycles for the tensile specimen builds discussed in Chapter 4. Following procedures for powder reuse outlined in Chapter 2, the powder was first used to evaluate the metal fatigue properties in the as-built and machined condition. All builds in this investigation were printed in succession to minimize sources of variability related to machine degradation, powder contamination or other factors.

5.3.2 *Build Design*

A multi-factor experimental approach was adopted to investigate the effects of selected design parameters and their interactions on the microstructure and fatigue properties of Ti6Al4V. Three factors were investigated including part height in the build volume, radial distance from the center of the build plate, and part thickness, which are visually represented in Figure 5.1.

Regarding the build design parameters associated with location, height refers to the location of the thinnest cross-section of the gauge section along the build direction. Radial distance is the location of the central axis of the specimen relative to the center of the build space in the X-Y plane (build plane). Radial distance was selected, as opposed to X and Y position, to reduce the dimensionality of the parameter space investigated. A reduction of the number of factors improves the statistical power of the data. Finally, the component thickness was also considered, which corresponds to the diameter of the thinnest area of the gauge section.

Factor levels used for the DOE of metal evaluated in the “as-built” condition are listed in Table 5.1. A preliminary study was necessary to develop an understanding of the range in fatigue life responses that result from the parameter space explored. The height factor was chosen to be limited to a single level in this preliminary study since it was the least influential factor of the three that were evaluated in the study involving monotonic loading. The other two design factors have three levels to allow for polynomial regression and potential optimization of the parameters.

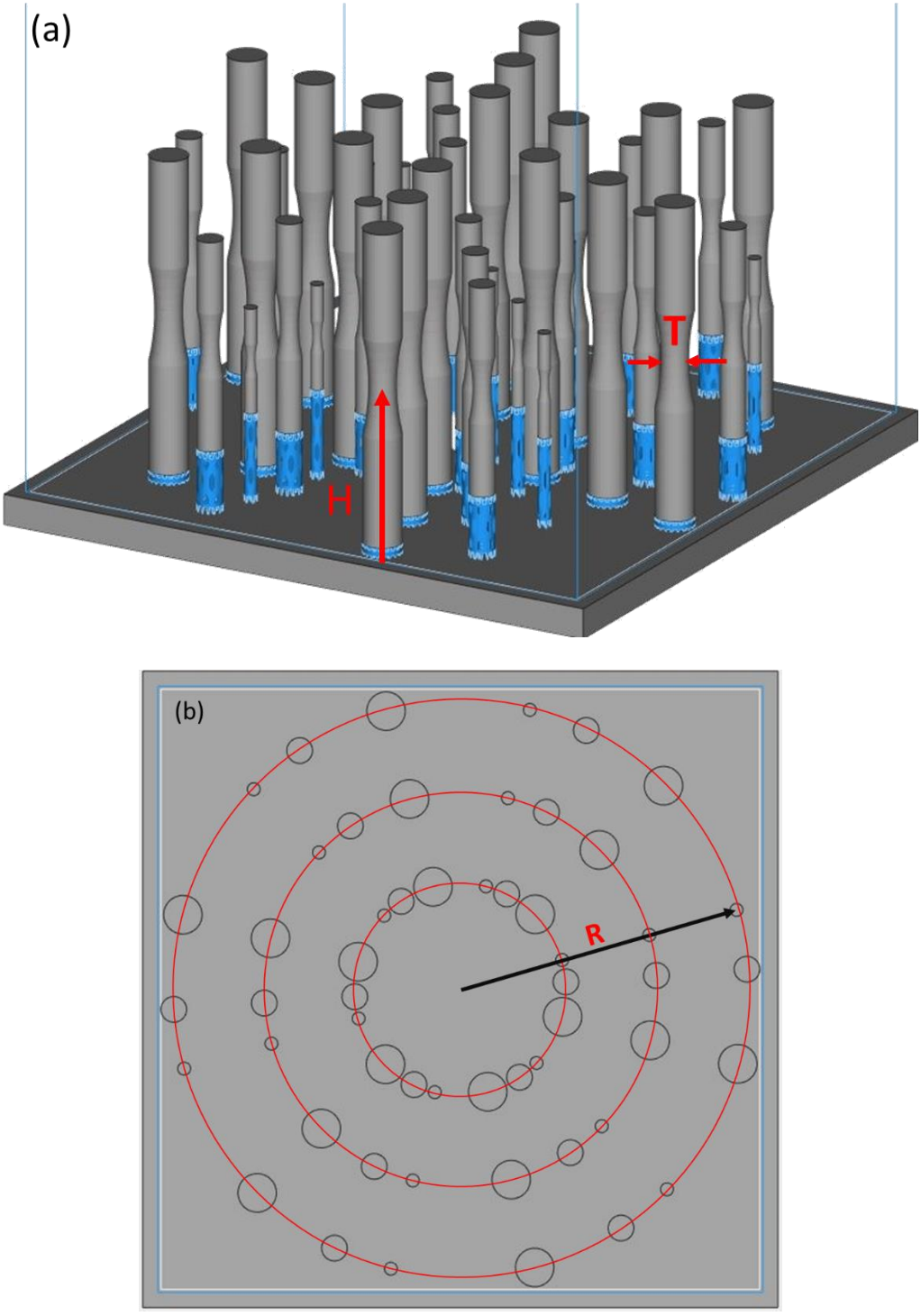

Figure 5.1. Build design for the preliminary investigation. **(a)** Oblique view of the build design for the as-built fatigue study. Only one height (H) level was printed for this preliminary

investigation. Thickness (T) of the parts is the diameter of the thinnest part of the gauge section. **(b)** Top view of the build with red rings indicating the three radial distance (R) levels.

The height, radial distance, and thickness were selected for the preliminary DOE and a second DOE that included an evaluation of the fatigue performance of the metal after post-build machining. The build design adopted for this second DOE is shown in Figure 5.2. In contrast to the preliminary DOE involving fatigue performance in the as-built condition, a full complement of part height was included across the build, which resulted in a full factorial DOE with 3 factors. Full factorial designs with 3 levels allow for every combination of factors to be investigated with polynomial regression fits. The non-linear responses reflected in the curve fit can help to identify optimal settings for the selected parameters.

Table 5.1. DOE factor levels of the three build design parameters. Red numbers indicate factor levels that only exist in the machined DOE.

Level	Height (mm)	Radial Distance (mm)	Thickness (mm)
Low	56	35	3
Mid	156	65	6
High	256	95	9

Part proximity, also considered part packing density, was not included as a factor of importance in the DOE due to results of the prior work concerning the results from monotonic loading. In that effort it was found to have no effect on the mechanical properties. Altogether, the factors considered in this investigation provide a comprehensive description of the build design

parameters in EBM, which is essential to develop a thorough understanding of the importance of component design and its placement on the fatigue performance.

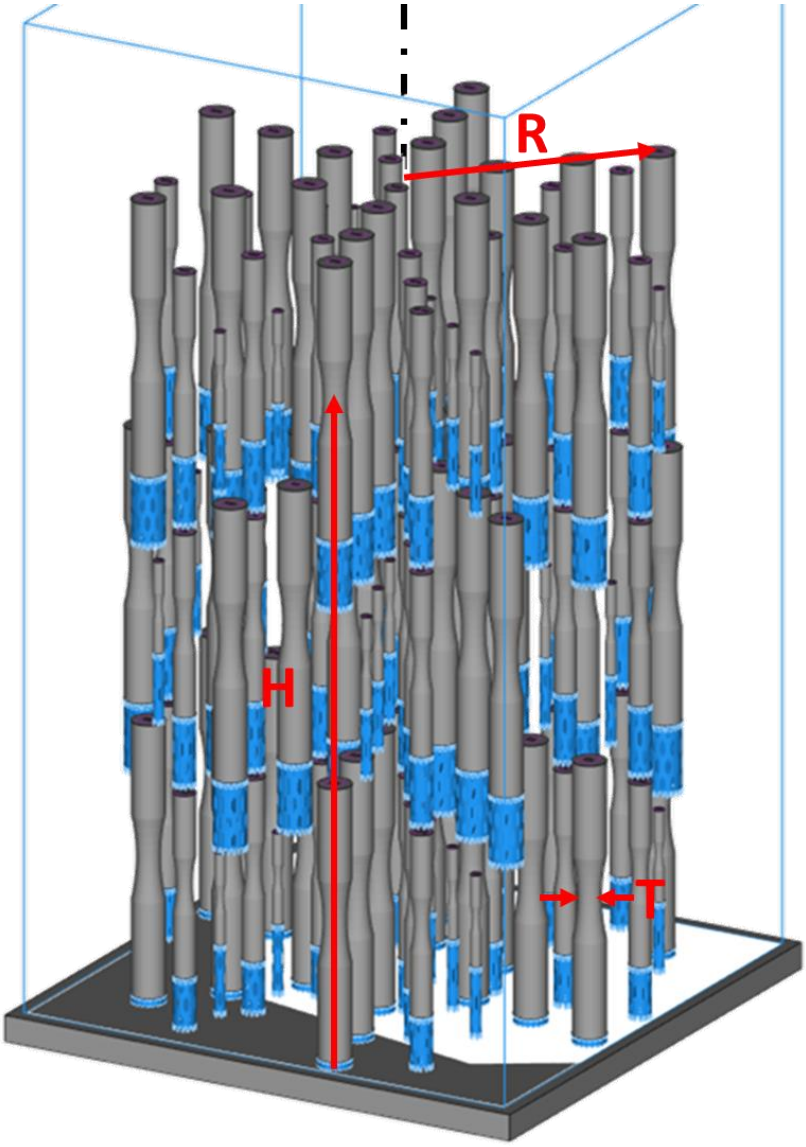

Figure 5.2. Oblique view of the build of fatigue specimens. Illustrated with the red arrows are the three design parameters: Height (**H**): distance from the base plate to centroid of a part, Radial distance (**R**): distance from the middle of the build plane (central axis represented by dashed

black line) to centroid of a part, and Thickness (**T**): diameter of the thinnest portion of the gauge section of a part.

5.3.3 *Printing and Design Restrictions*

For all builds, the beam parameters used in the melt theme are the same default parameters used for the builds in the previous chapters. The beam parameters were set at the default values for all builds to ensure that there was no influence from other build factors aside from the build design parameters.

Part orientation is an important factor to consider in metal AM due to the anisotropic nature of the microstructure in terms of grain orientation and void orientation, as previously described. Despite this concern, only the vertical orientation (along the build direction) was considered in this study of fatigue properties. This orientation was the only feasible option from a buildability perspective, and, more importantly, the vertical orientation is expected to exhibit inferior fatigue life [36,131]. Using a horizontal orientation with specimens parallel to the build plane would result in part overlap and out of bounds issues as discussed in Chapter 4. Accounting for variability in the metal with build orientation enables determination of the lower bound for the fatigue life. However, the primary orientation of defects (both surface and subsurface) in EBM are within the build plane, which will be the limiting factor for fatigue life of the vertical orientation. Furthermore, packing specimens within the desired locations in the build envelope according to the DOE precludes them from being oriented off axis from the build direction. Furthermore, most components will experience multiaxial stress states with at least a portion of the volume having stresses aligned with the vertical orientation, i.e., perpendicular to the most prominent defects in

EBM. Thus, the vertical orientation is the best choice for considering the fatigue performance of metal from EBM.

For the DOE performed with metal in the machined condition, it was not possible to produce enough specimens in a single build to have sufficient sample population as required for full factorial at the four stress levels of the fatigue testing. Therefore, a second build was performed with the exact same build design and printing conditions to mitigate inter-build variation. This second build was conducted immediately following the first build to minimize potential effects of machine condition or powder degradation.

5.3.4 *Surface Treatment*

Net-shape machining was performed on a portion of the parts that were evaluated in the "machined condition". The machining was performed to remove effects from the surface roughness on the fatigue life. All parts were processed by turning operations by a component service provider with appropriate settings for titanium to avoid microstructural changes or residual stresses at the surface. The first build was machined at the University of Washington Dept. of Chemistry Machine Shop. Due to excessive work and lead time, the second build was machined at an external machine shop (Limited Productions Inc., Bellevue, WA). Approximately 0.35 mm was removed from the external diameter from the entire length of the samples. This results in a 0.7 mm decrease from the printed dimension, e.g. the 9 mm samples became ~8.3 mm.

5.3.5 *Fatigue Testing*

Fatigue testing was conducted on all the as-build and machined specimens according to ASTM E466. The fatigue tests were performed using a commercial hydraulic universal testing

system (Instron: Model 8520; Norwood, MA) under constant amplitude load control with a stress ratio (R) of 0.1 and frequency of 20 Hz. The total number of cycles to failure were recorded for stress levels that were chosen based on previously published literature to encompass a large range of the high cycle fatigue (HCF) regime below runout (10^7 cycles), as illustrated in Figure 5.3. Due to the limited number of specimens in the DOE with metal in the as-built condition, only two stress levels were used to ensure that enough specimens were available to capture the statistical scatter in the fatigue life response for each specimen size and location.

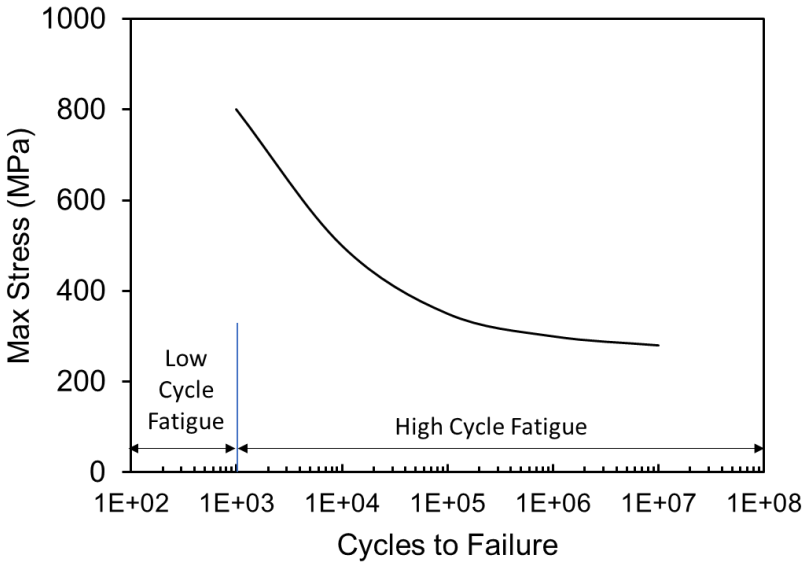

Figure 5.3. Schematic S-N diagram for Ti6Al4V built from data in the MMPDS-16 for mill annealed Ti6Al4V plate at R=0.1.

For testing the fatigue specimens of the as-built condition, maximum stress levels of 250 and 550 MPa were selected. These two levels are well with in the HCF regime and allowed for fitting of the Basquin power law relationship. Similarly, for testing the fatigue specimens of the machined DOE, maximum stress levels 400, 600, 800 and 1000 MPa were selected. A stress-life

(S-N) diagram was constructed with the fatigue responses and the Basquin model (Eq. 5.1) was fit to the data according to

$$S = AN_f^B \tag{5.1}$$

where S is the stress level (can be the max stress, stress amplitude, or effective stress), A and B are curve fitting constants, and N_f is the number of cycles to failure. The stress life distributions were evaluated with respect to the factors and analyzed statistically through multiple linear regression. The statistical analysis was performed using Minitab 14 (State College, PA).

For comparison of results with the literature, the maximum stress was converted to effective stress using an equation developed by Li et al. [120] to correct data from studies that did not test at a stress ratio of 0.1. Converting to effective stress with Eq. 5.2 is shown to be acceptable for -0.5<R<0.5 [Ref?].

$$S_{eff} = S_{max}\left(\frac{1-R}{2}\right)^{0.28} \tag{5.2}$$

5.3.6 *Defect Analysis*

Prior to fatigue testing, the porosity and its distribution within selected fatigue samples were evaluated using X-Ray Computed Microtomography (μCT). The evaluations were performed using a commercial system (X5000, North Star Imaging, Rogers, MN, USA). The scan parameters used for all specimens are listed in Table 5.2. Projections were first reconstructed in a commercial software (efX CT) that is provided by the manufacturer of the μCT scanner. This software embedded the geometric data from the geometry tool that was scanned after the specimen. Once

reconstructed, the volume is then exported as a slice stack along the build height direction. The image stack was then imported to VGSTUDIO MAX (Volume Graphics Inc., Charlotte, NC, USA) for evaluation of the porosity.

Table 5.2. Parameters used for scanning as-built fatigue samples.

Scan Parameter	**As-built**	**Machined**
Voltage	160 kV	220 kV
Current	60 µA	75 µA
Geometric zoom	23.33X	11.82X
Projections	1200	5400
Scan mode	Step	Step
Frame average	2 frames/projection	2 frames/projection
Frames per second	1 fps	2 fps
Gain maps	7	7
Resolution	8.162 µm	16.49 µm
Filter	0.005 in. brass	0.005 in. brass

Based on results of the fatigue study with the as-built specimens, it was identified that an increased sample size was needed for defect analysis. Therefore, XCT analysis was conducted on >50 % of the machined specimens spanning all combinations of the factor levels. In order to accommodate the increase in specimens requiring XCT scanning, multiple samples were scanned simultaneously to reduce the cumulative scan time and associated costs of the analysis. Placing an array of multiple samples in the scan region of interest lead to changes to the scan parameters from

those listed in Table 5.2. Firstly, the x-ray source voltage was increased to penetrate the extra material from having multiple specimens in line with the source and detector. Secondly, the geometric zoom was reduced to fit all the extra specimens into the detector window of view. Subsequently, these scans for the machined specimens have a spatial resolution of 16.49 μm, in comparison to 8.16 μm for the as-built specimens. Finally, placing more specimens in a single scan enabled longer scans with higher number of projections, while still maintaining a significant reduction in the time required per specimen. Using more projections improved the angular resolution of the scan planes and the grayscale accuracy for voxels further from the central axis of the part stage.

5.3.7 *Fractorgraphy*

A fractographic analysis of the fatigue specimens was performed post-failure using a combination of optical and scanning electron microscopy. Optical microscopy (OM) was performed on an Olympus Model SZX16 stereomicroscope for origin determination and qualitative mapping of the fracture surface. Scanning electron microscopy (SEM) was performed on a Philips Model XL-30 using the secondary electron detector to determine finer features of the fracture surface and perform quantitative measurements of the fatigue fracture features.

5.4 RESULTS

5.4.1 *Fatigue Life*

Results from the fatigue testing in the current study are presented with fatigue data reported in the literature for Ti6Al4V in Figure 5.4. There is a relatively large degree of scatter in the

reported data for metal evaluated in both the machined and as-built conditions. Nevertheless, the data of the present study falls within the cluster of data for the as-built condition, and for the machined condition. There is a subtle difference in the slope of the Basquin model fit with respect to that of the literature for the machined condition, which will be addressed.

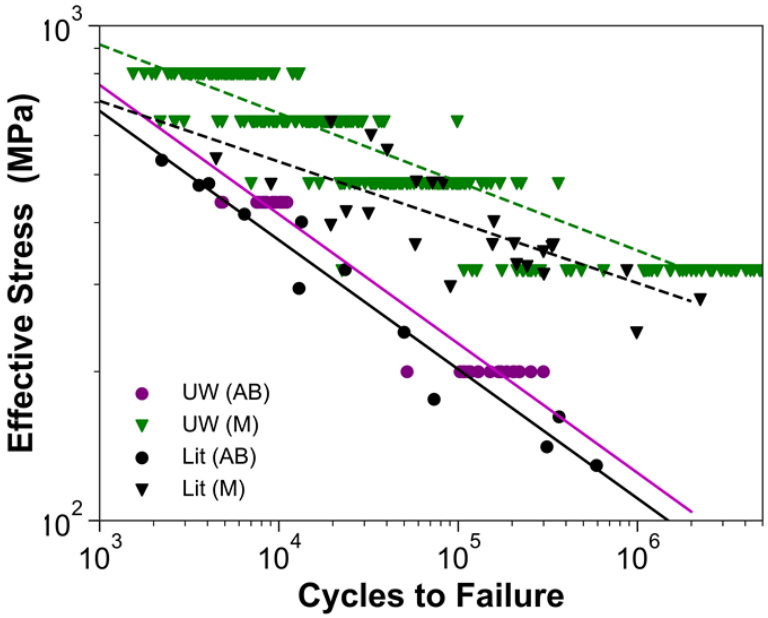

Figure 5.4. S-N diagram with comparison of fatigue life present study against EBM literature data for vertically oriented specimens only [36].

Further scrutiny of the S-N data according to the factor levels enables an identification of the main effects on the fatigue life distributions. Figure 5.5a and 5.5b show the S-N data restricted to the three levels of radial distance and thickness, respectively. According to these figures, there is a substantial reduction in the fatigue life of the metal for the lowest thickness level, and a minor decrease in the fatigue life with increasing radial distance from 35 mm to 95 mm from the center of the build plate.

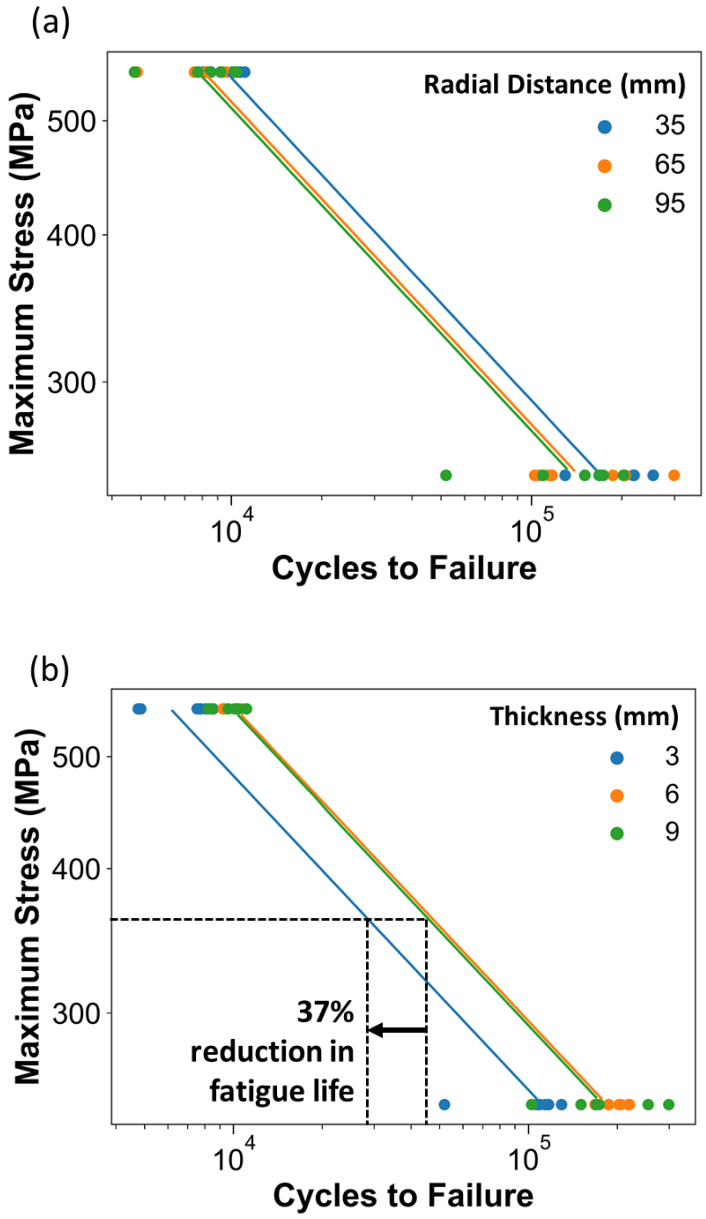

Figure 5.5. S-N diagrams (log-log scale) of data from the DOE with metal in the as-built condition and with Basquin model fits. Shown are effects of the **(a)** radial distance and **(b)** thickness factor levels

The effects of the three primary factors on the fatigue performance of the metal subject to machining are shown in Figure 5.6. Specifically, the effects of height, radial distance and thickness are shown in Figure 5.6a, 5.6b and 5.6c, respectively. Regarding the influence of height (Figure 5.6a), there is no significant difference between the fatigue life responses for this factor at any of the stress levels. The results for radial distance (Figure 5.6b) demonstrated a substantial decrease in the fatigue life resulted with an increase in radial distance. Finally, the effect of thickness (Figure 5.6c) on the fatigue is similar to that for the as-built condition; specimens with low thickness (3 mm) had considerably lower fatigue life for all the stress levels evaluated.

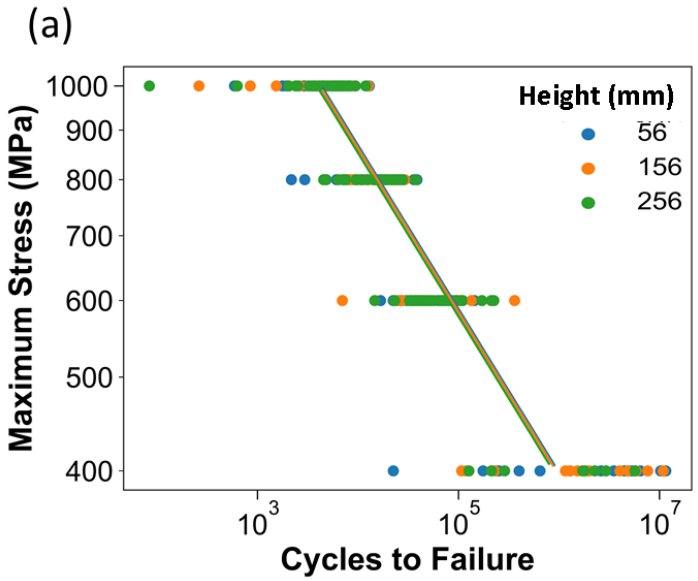

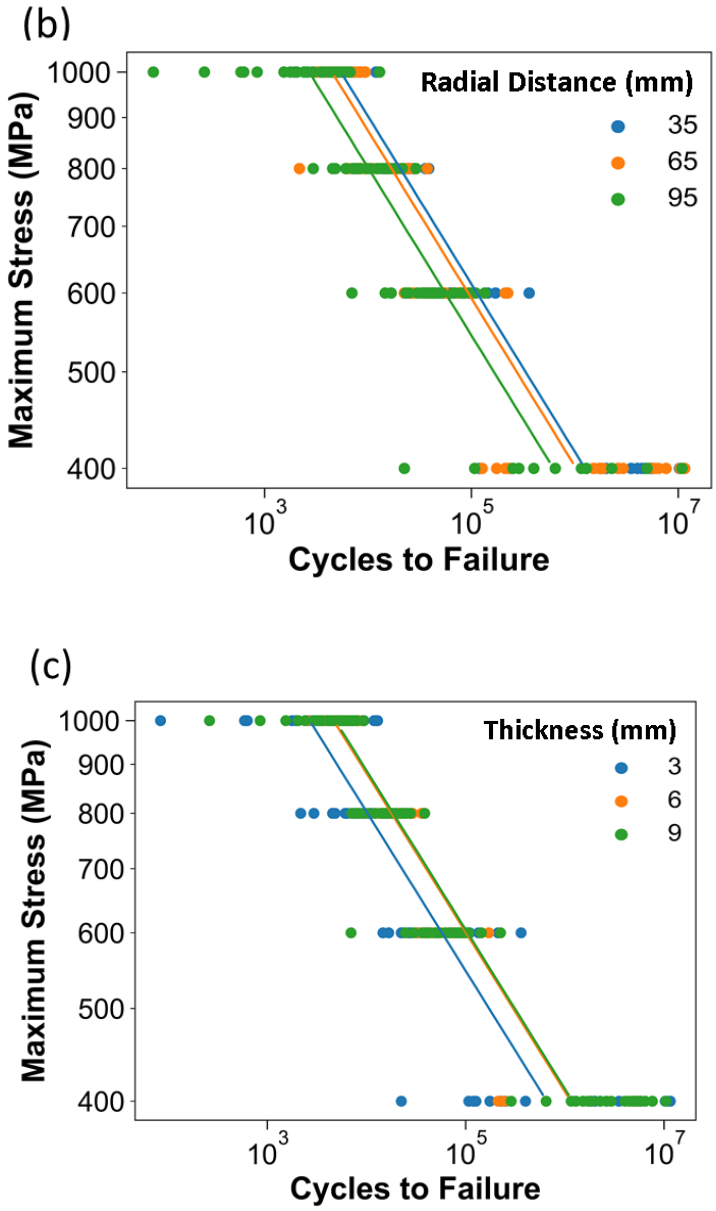

Figure 5.6. S-N diagrams (log-log scale) of data from the DOE with machined condition and with Basquin model fits. Shown are the influence of **(a)** height, **(b)** radial distance and **(c)** thickness factor levels.

5.4.2 *Porosity Distribution*

In general, the most important characteristic to the severity of pores is their size. Size can be defined in several ways based on one-, two-, and three-dimensional metrics. The pore or void volume is the first approach, but it provides limited understanding of the stress concentration posed by its geometry. A volumetrically large pore could be oriented along the length and located at the center of the specimen, which would pose limited concentration of stress and have limited effect on the cyclic behavior of the part. The next treatment could involve the effective pore diameter defined by a circumscribed sphere, i.e. the smallest sphere that can fully encompass the pore. While more representative of the propensity for stress concentration than the volume definition, it is not effective at describing the effect of elongated pores oriented parallel or perpendicular to the loading direction. The largest pores in EBM Ti6Al4V are typically lack of fusion (LOF) voids that exhibit their largest dimension in-plane. As such, descriptions that are based on diameter may underestimate the stress concentration. In addition, infrequent “rogue” defects that span many build layers can limit the applicability of the pore diameter definition. Originally proposed by Murakami [132] and applied to small defects in metallic materials [128], the root area of the pore is now one of the more prevalent methods used in AM [82,129,131] for characterizing size and assessing the potential severity. An illustration concerning how the pore area is extracted by projecting the pore onto the X-Y plane and then taking the square root of the area is shown in Figure 5.7a.

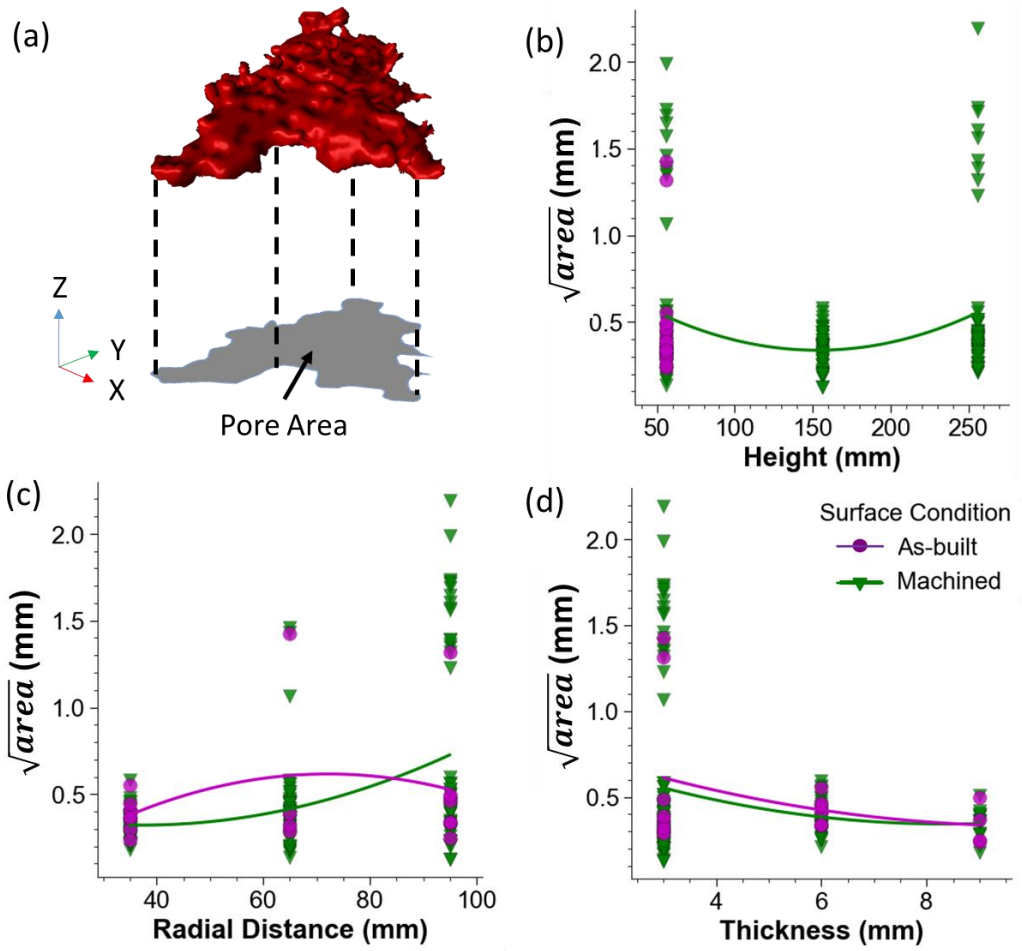

Figure 5.7. Pore size distribution in the metal of the DOEs. **(a)** The area of the pore (*A*) is defined as the area projected onto the plane perpendicular to the principal locating direction, which is the build plane (X-Y) for vertically oriented specimens. **(b)** and **(c)** show the maximum √*area* of all pores found in the gauge section of the specimens scanned with XCT as a function of the two main factors.

The largest pore, characterized by √*area*, for each scanned specimen are plotted against the DOE factors in Figure 5.7b-d. The importance of height on the pore size distribution of the metal in the as-built and machined condition are presented in Figure 5.7b. For metal evaluated in the as-built condition of the preliminary DOE, the height parameter was restricted to a single

level, i.e., the lowest height. However, for the machined condition the specimens were printed at all three height levels. As evident in Figure 5.7b, there is an inverse quadratic effect between the build height factor and the $\sqrt{area}$. In some samples there are exceptionally large internal pores that are rogue defects, which are not indicative of LOF type voids. However, at the middle level height (156 mm) no samples scanned with XCT contained these large rogue defects.

The pore size distribution is shown in terms of radial distance in Figure 5.7c. There is an inverse quadratic trend for the as-built samples; the minimum pore size is located at the smallest radial distance (i.e. center of the build space). The machined specimens also exhibited a quadratic trend, but with concave distribution with radial distance. The metal with smallest pore size was located at the smallest radial distance, and with size distribution that is consistent with that of the as-built specimens. The discrepancy in trends for the as-built and machined groups may be attributed to the differences in sample size between the two groups, and smaller specimen count in the as-built condition. For the as-built condition, only a single specimen contained a rogue defect, which was at the largest radial distance; it is important to note that the sampling scheme for the as-built samples potentially missed these specimens. For the machined condition, only a few samples did not contain these defects, which were located at the high-level radial position. Of all samples with 3 mm thickness in the machined condition and with largest radial distance, 44% contained rogue defects.

The relationship between part thickness and pore size is shown in Figure 5.7d. As evident in this figure, the smallest pore size was found in specimen with largest thickness. Interestingly, the specimens with low level thickness (3 mm) demonstrated the largest pores overall and a bimodal distribution. There is a group of specimens with large pores (rogue defect) that occupies a significant portion of a build layer in a part and extends several layers (Figure 5.8). If the rogue

defects are eliminated from the data set the median largest pore size for 3 mm thickness parts would be lower than that for the specimens with 6 mm thickness.

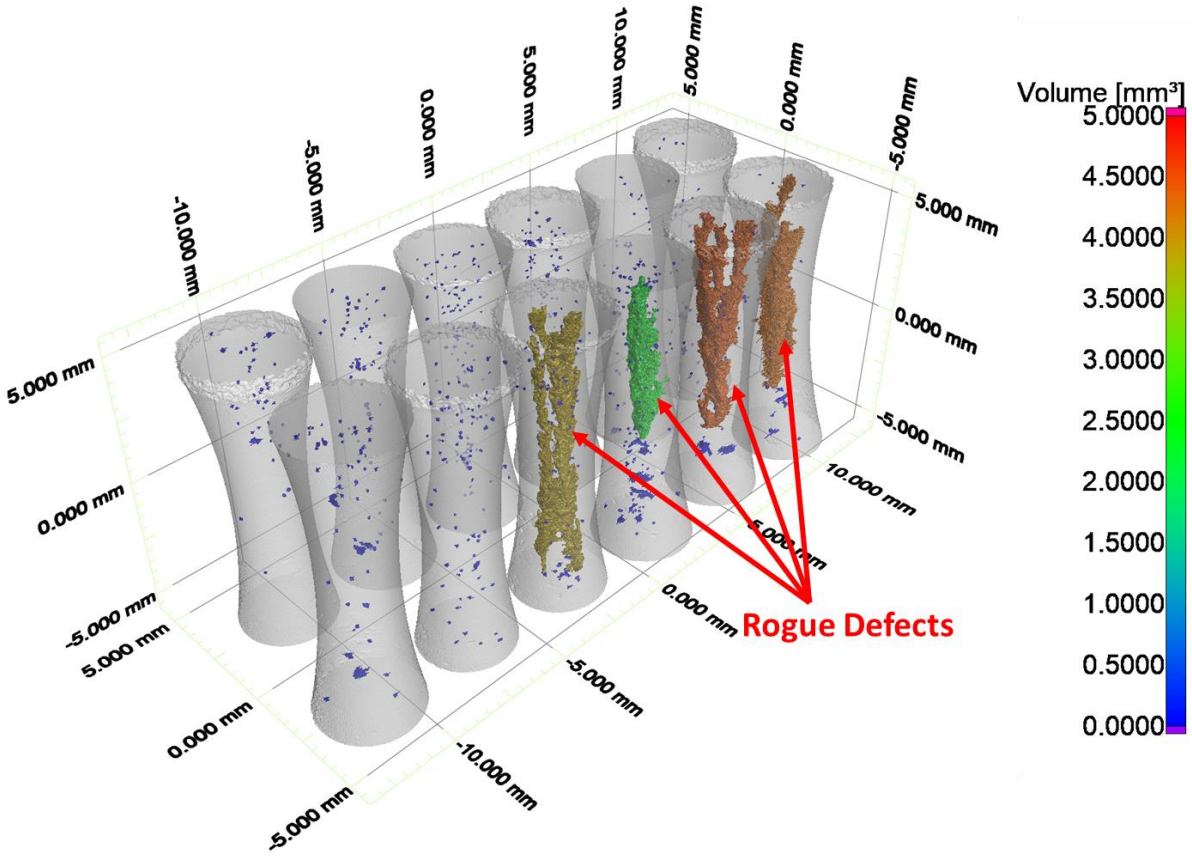

Figure 5.8. XCT 3-D models of low level (3 mm) thickness machined samples with pores with diameters above 0.1 mm shown. Examples of "rogue" defects that span significant z-height in a part are indicated with red arrows. Diameter is defined as the diameter of the minimum encompassing sphere, which would be the longest linear dimension of the pore.

Size is not the only characteristic of pores/voids that contributes to its severity and the effective stress concentration factor that it poses. The pore location relative to the free surface of a part is also important as it can influence the magnitude of stress concentration. It also takes less

time for inherent damage near the surface to develop into a crack and begin cyclic growth. With this in mind, it was necessary to quantify the location of pores from the free surface in the plane perpendicular to the loading direction. To support this effort, the edge distance of voids from the free surface was defined as the shortest radial distance from the pore surface to the part surface as shown in Figure 5.9a. Histograms were constructed to assess the pore distribution as a function of edge distance, which provide a measure of pore concentrations in terms of the cumulative radial position. A local maximum in pore density was noted near the surface of the specimens (<0.2 mm from the surface) in the as-built condition, which is visible for the 3 mm thick specimens in Figure 5.9b, and to a lesser extent for the 6 mm thick specimens in Figure 5.9c. However, a local maximum was not evident in the histogram for the 9 mm thick specimens (Figure 5.9d). Regardless of thickness, the maximum pore concentration was evident at an edge distance of approximately 0.7-1.1 mm from the free surface of the specimens. However, after machining the near-surface peak in the pore density histograms is not present, indicating that these near-surface pores were removed, or they became exposed at the surface.

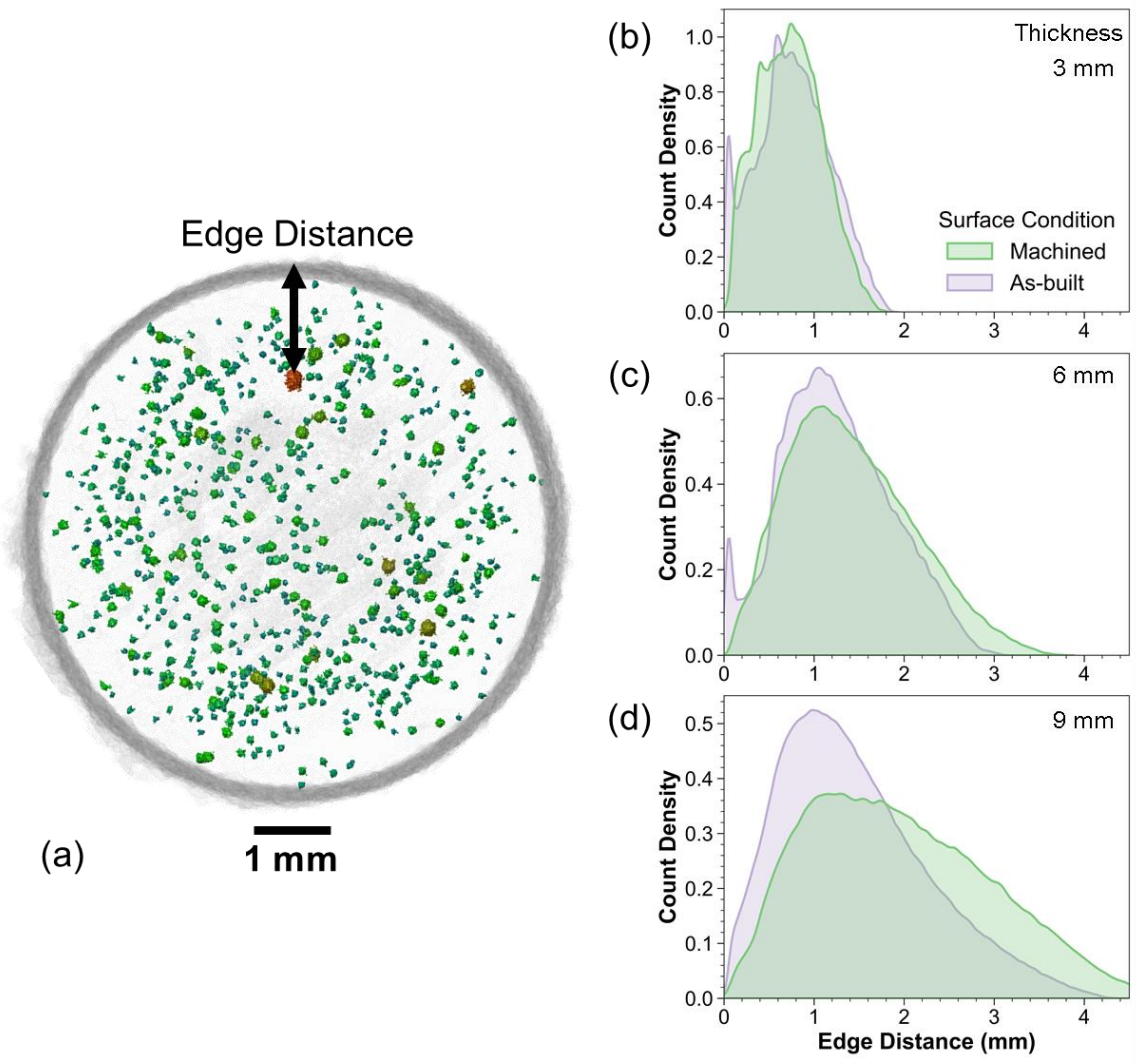

Figure 5.9. Pore distribution as a function of edge distance. Edge distance is defined as the distance of the surface of a pore to the free surface of the specimen and is visually represented in the top view projection in **(a)**. Count density plots for the three thickness levels (3, 6, and 9 mm) are shown in **(b)**, **(c),** and **(d)**; respectively, and indicate that the highest density of porosity is located at a ring around 0.7-1.1 mm from the surface.

The final metric for describing the pore geometry is morphology, which can be described in terms of its sphericity, aspect ratio, and radius of curvature. Each of these parameters is

potentially relevant to the stress concentration and its contribution to the fatigue response. Sphericity is a measure of how closely a 3-D object (i.e. pore) resembles a sphere through a ratio of surface area of the object to the surface area of a sphere with equivalent volume as shown in Figure 5.10a. Sphericity is defined as

$$Sphericity = \frac{SA_{sphere}}{SA_{pore}} = \frac{\pi^{\frac{1}{3}}(6V_{pore})^{\frac{2}{3}}}{SA_{pore}} \tag{5.3}$$

Where *SA* is the surface area and *V* is the volume. Sphericity will always be a ratio that is between 0 and 1 because spheres are a special case with minimum surface area for a given volume. As a pore shape becomes more irregular, the surface area will increase and result in a lower sphericity ratio.

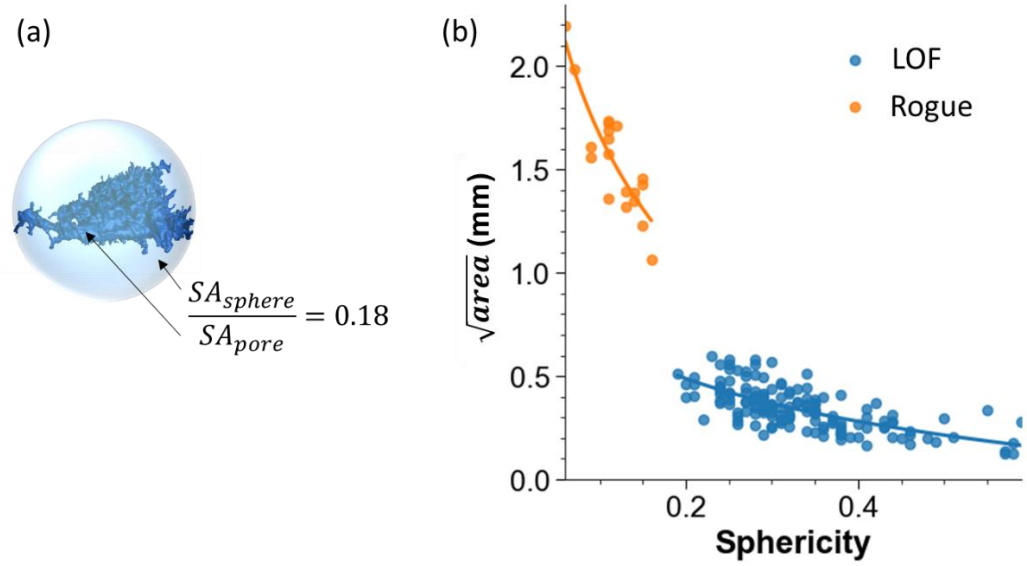

Figure 5.10. Sphericity of internal pores and voids. **(a)** Example of a LOF defect and the resulting sphericity calculation, Eq. 5.3. **(b)** Size of a pore, using the $\sqrt{area}$ metric, as a function of sphericity with separation of the rogue and LOF defects.

As evident in Figure 5.10b, rogue defects and LOF voids exhibit an exponential relationship with sphericity, which was found previously in Chapter 3. In other words, there is a decrease in the sphericity of the pores/voids with increasing size, which is of substantial concern. Pores with lower sphericity would be expected to exhibit greater stress concentration as a result of more irregular shape with long sharp branches that act as sites for crack initiation.

5.4.3 *Fractography*

An evaluation of the fracture surfaces of exemplary fatigue specimens was conducted to determine the origin of flaw that served as the sites for fatigue cracks initiation. Based on the excessively large rogue defects present in some samples, it was expected that fatigue failure would originate from these defects. However, surprisingly, they did not generally serve as the sites for crack initiation. A micrograph of the fracture surface for an as-built specimen with rogue defect is shown in Figure 5.11a. Despite the presence of a rogue defect that occupied up to 10 % of the fracture surface area, all of the failure origins were found to be at the specimen surface.

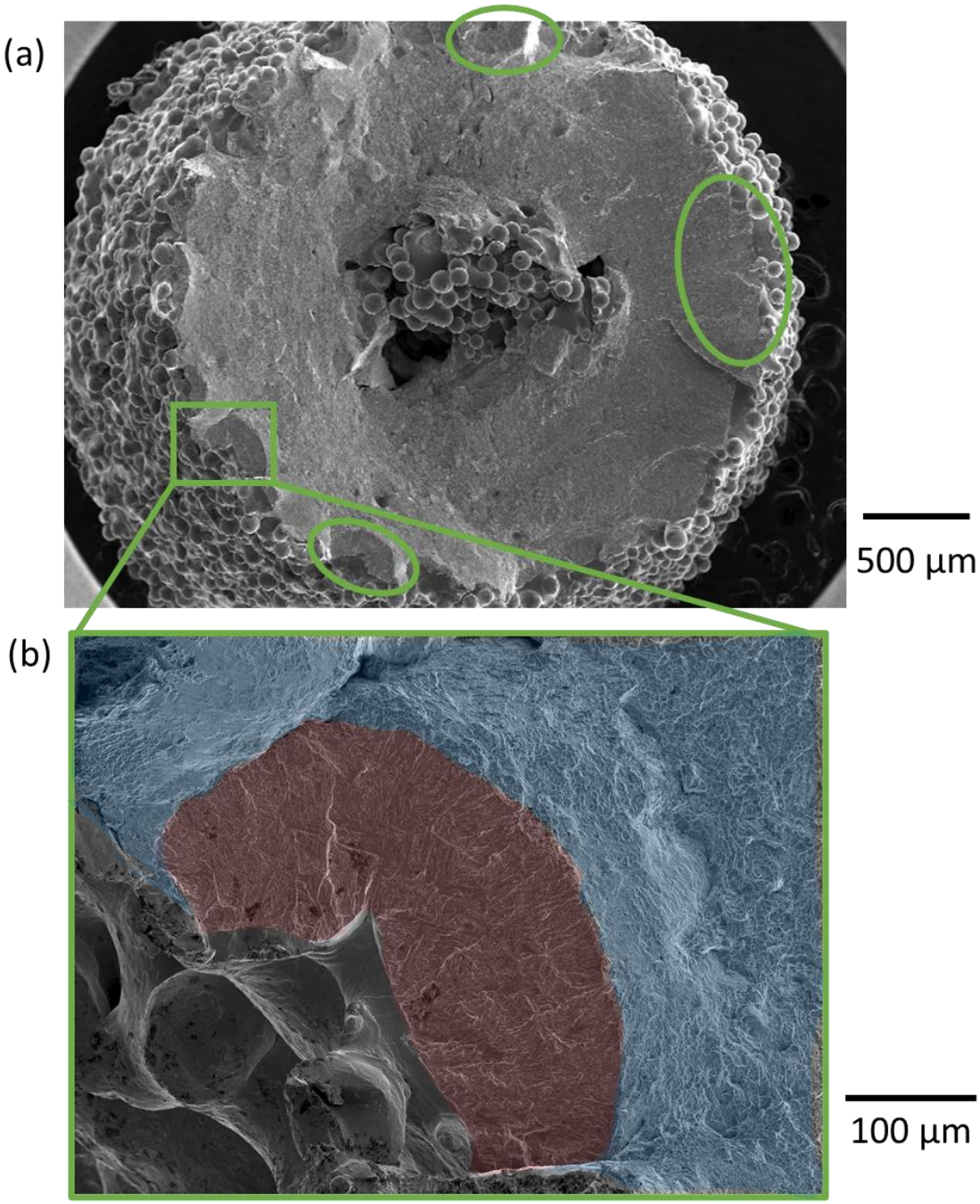

Figure 5.11. Fractographs of an exemplary as-built specimen with thickness of 3 mm (low level). **(a)** Low magnification SEM view. Circled in green are a few of the origins along the surface. No apparent initiation was found along the edge of the large pore at the center of the specimen. **(b)** Higher resolution micrograph indicating fatigue crack initiation from the surface. Red: Stage II fatigue crack propagation zone. Blue: Stage III fast fracture

For the specimens evaluated in the as-built condition, the origins of fatigue failure were frequently identified to be surface flaws, such as that shown in Figure 5.11b. Some stable crack growth is visible (red region) and distinguished by the transition between a diffuse fracture mirror and the transition from radial lines to hackle extending perpendicular to the loading axis. These details indicate that the crack initiated at the surface and underwent progressive growth under the cyclic loading. Once a sufficient number of cracks initiated from the surface and progressed to a critical size, fast fracture (blue region) ensued, characterized by the stereotypical dimpling of ductile titanium under monotonic loading.

The initiation of fatigue cracks was only identified to occur from the surface of the specimens, regardless of the severity of defects or the build design factors. Specimens with high level (Figure 5.12a) and low-level of thickness (Figure 5.12b) both exhibited crack initiation from the surface. Based on observations of the fracture surfaces, the smaller samples exhibited a larger number of origins.

(a)

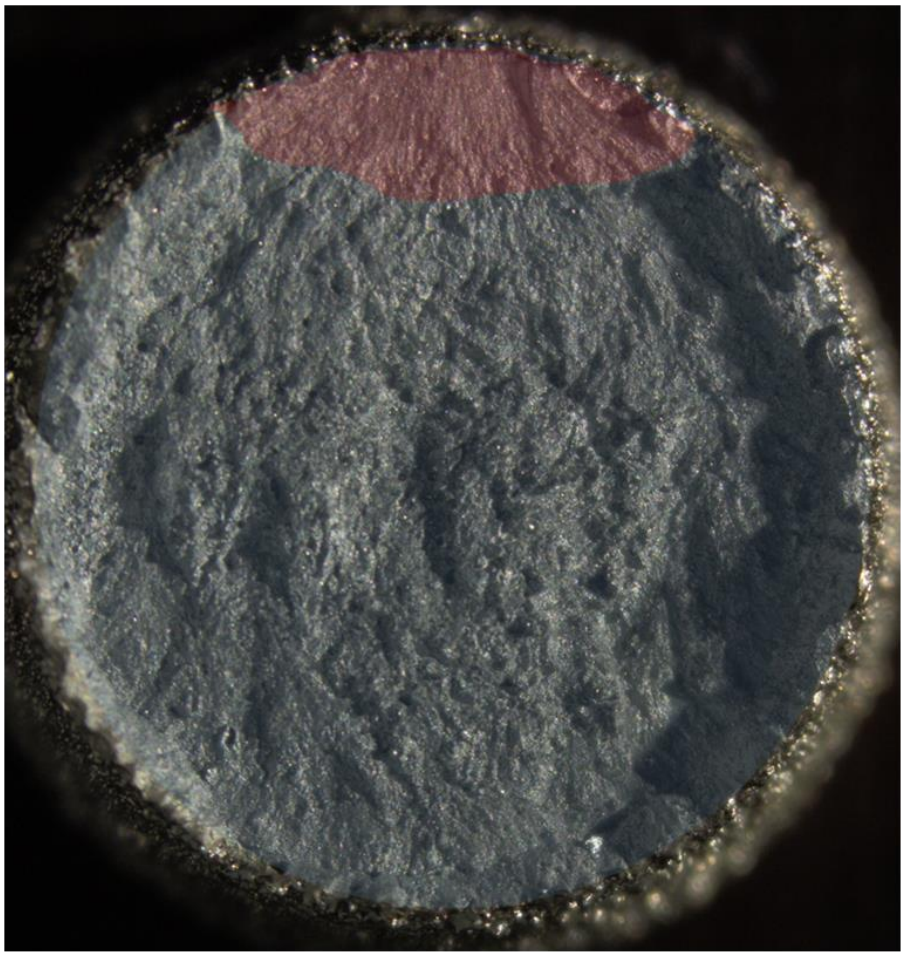

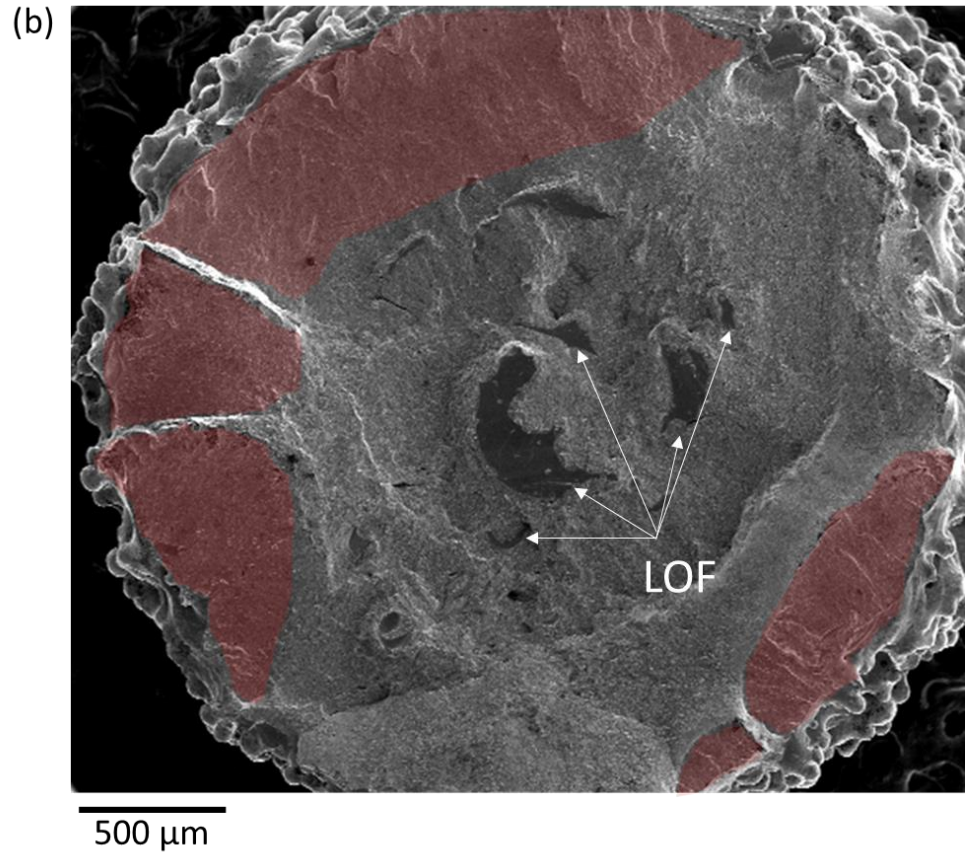

Figure 5.12. Fractography for a 9 mm thick specimen. **(a)** OM fractograph. Several origin sites are located at the top of the fracture surface. Highlighted in red is the estimated Stage II region of crack propagation, with the Stage III fast fracture portion highlighted in blue. **(b)** SEM fractograph of a 3 mm thick specimen with crack propagation zones highlighted in red (not inclusive of all regions of crack growth). Indicated in the center of the fracture surface are several LOF defects.

Removal of the as-built surface texture by machining did not change the origins of fatigue fracture. Several specimens exhibited surface origins or evidence that the surface contributed to the fatigue fracture. As previously noted, this is expected to result from the

exposure of sub-surface LOF defects at the surface by the post-process machining as shown in Figure 5.13.

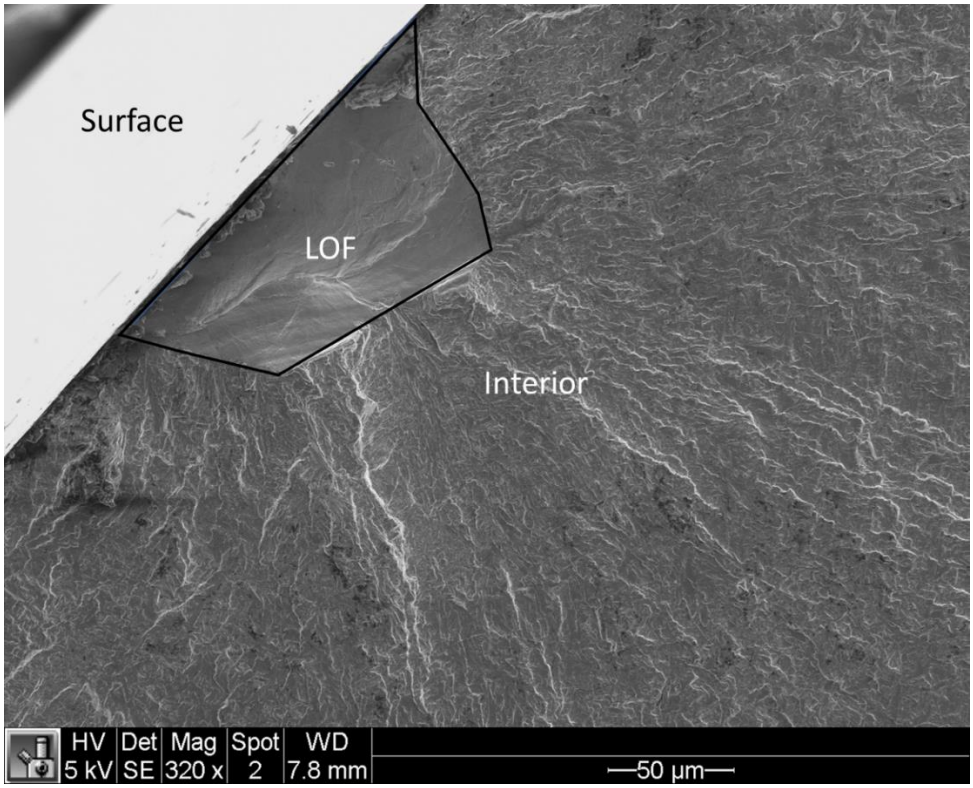

Figure 5.13. Example of a LOF defect that was exposed to the surface after machining.

Representative origins of fatigue failure evident in the fracture surface of machined fatigue specimen are shown in Figure 5.14. In Figure 5.14a, a low porosity sample is shown that exhibits at least two dominant origins at the surface, as highlighted with the arrows. A second example is shown in Figure 5.14b, which is a relatively complex fatigue fracture surface for a specimen with interior rogue defect consisting of many large interconnecting LOF voids. Despite the size and irregularity of this central rogue defect, failure involved multiple origins. Apart from

cracks extending from the central defect, there are several that originate at the machined surface and appear to involve voids that were exposed by material removal.

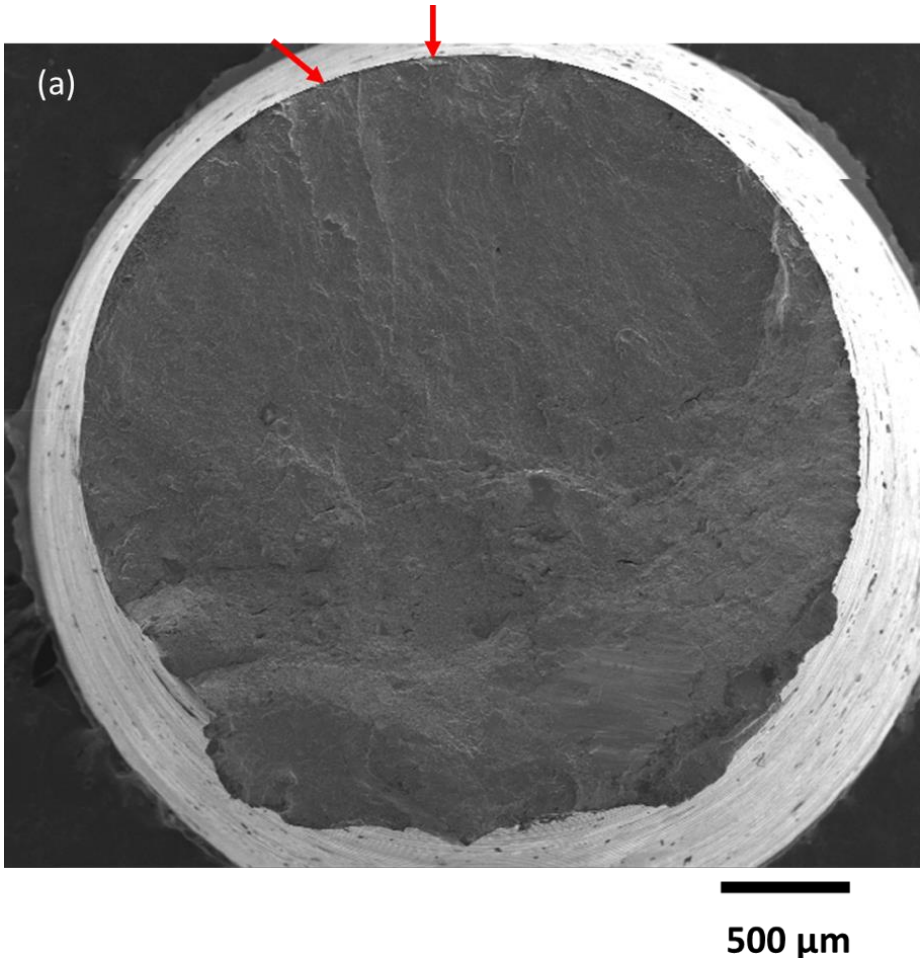

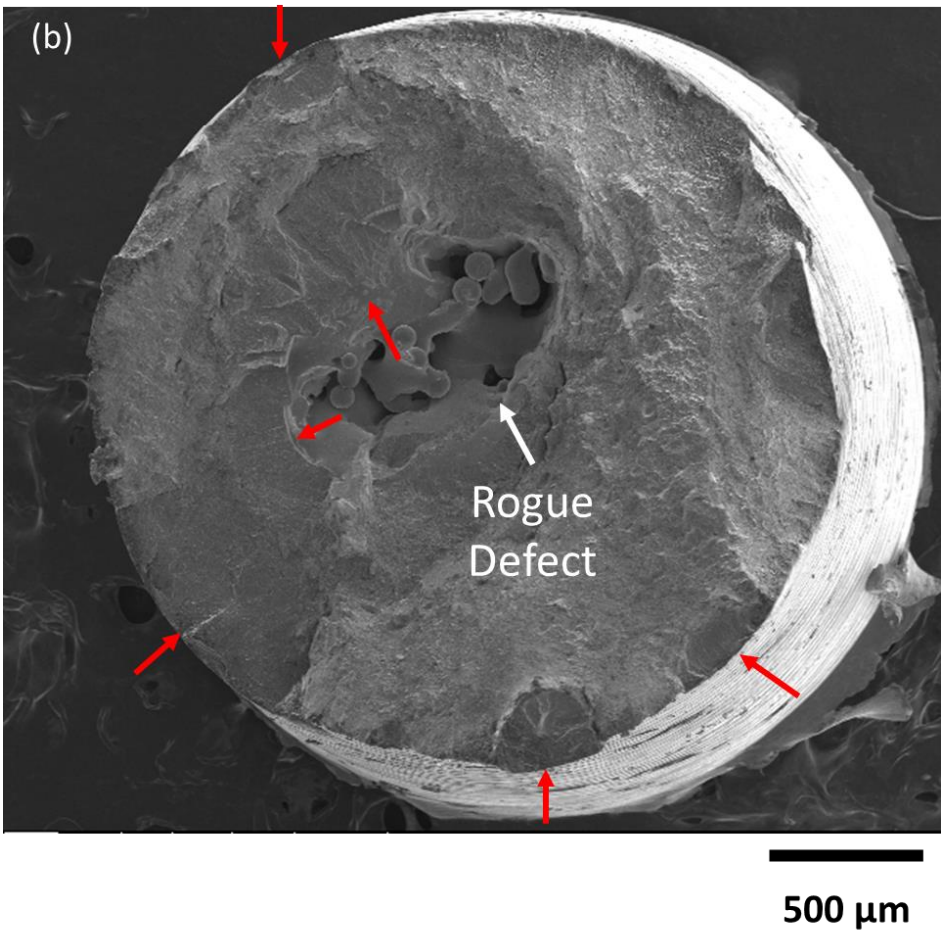

Figure 5.14. SEM fractographs for two machined 3 mm thickness specimens. **(a)** Low porosity sample that had two dominant origins, which appear to be exposed LOF defects. **(b)** Many origins exist with several defects at the surface, which caused dispersed initiation, despite the massive rogue defect at the center of the specimen.

5.5 DISCUSSION

5.5.1 *Fatigue Life*

Based on the S-N diagrams in Figure 5.4, the fatigue data from the present investigation lied well within the range of fatigue data reported in the literature for EBM of Ti6Al4V. There was scatter

in the experimental data that was attributed to the range in design parameters, which was also exhibited in the reported data. A large portion of the scatter in data from the literature is associated with differences in surface condition and specimen orientation; post-build machining and the horizontal specimen orientation (aligned to the build plane) were associated with superior fatigue life. When the reported fatigue data is restricted to the vertical orientation, the Basquin models developed from the experimental DOE data for the as-built condition or machined condition are in close agreement. Nevertheless, there are limitations to the data in these published studies, as few list the beam parameters used, machine used, or powder age [36,120,133]. Hence, it is difficult to comment on all of the potential sources to differences in the fatigue life distributions.

Traditional manufacturing processes for Ti6Al4V components in aerospace include either casting or wrought forming. The goal for metal AM is to reach an equivalent performance to that achieved by wrought forming. Therefore, it is relevant to compare fatigue data of the DOE with that from cast and wrought form sources as shown in Figure 5.15. Results from metal evaluated in the as-built condition fall within the region of fatigue life data reported for casting as presented in the ASM Handbook [134]. However, results for the machined condition are at the bottom edge of the reported fatigue life data for wrought form metal, also from the ASM Handbook. Furthermore, a portion of the machined data falls within the region of cast metal, which corresponds to the EBM specimens with rogue defects. Assuming that process control would eliminate metal with those defects, then the fatigue life responses for the machined condition are comparable to that of Ti6Al4V traditionally manufactured by wrought forming and in the annealed condition. Further improvements could be garnered by employing a post-process treatment such as solution heat treating and aging (STA) or hot isostatic pressing (HIP) [36,104].

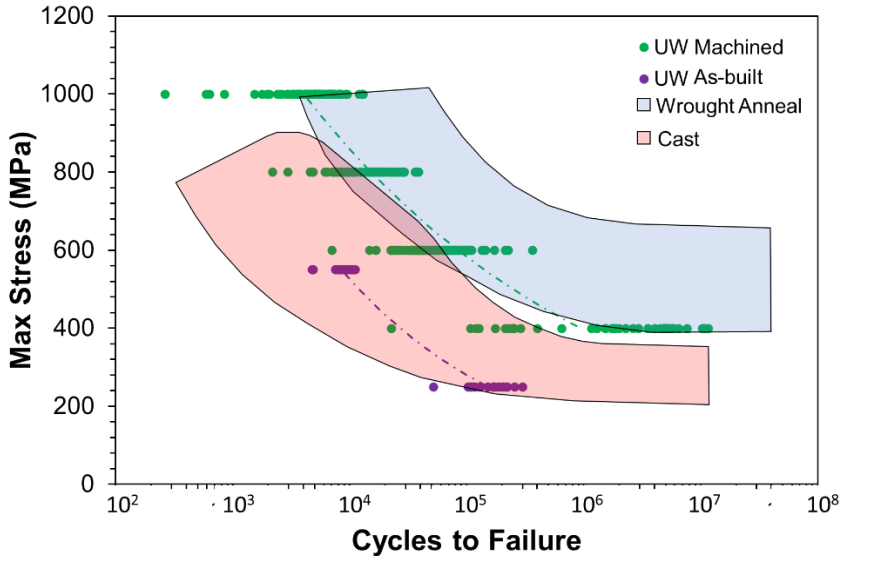

Figure 5.15. S-N diagram comparing the data generated during the fatigue DOE study in both the as-built and machined states against fatigue life range for two traditional Ti6Al4V materials. Data range for wrought and cast fatigue life are extracted from the ASM Handbook [134].

Build design parameters were found to have a significant effect on the fatigue properties of the printed specimens in both the as-built and machined condition. Of the factors evaluated, the most significant effect was attributed to part thickness. There was nearly 40% reduction in the as-built fatigue life of the specimens with 3 mm thickness with respect to those with 6 mm thickness. Similarly, for the machined condition, the fatigue life decreased with decreasing thickness, with average reduction of approximately 45 % across the three stress levels. Some specimens exhibited subsurface LOF voids and surface defects that worked synergistically as the origin of failure, while others had only LOF or surface defects. Le et al. [125] investigated the effects of part size (thickness) on the fatigue life of SLM Ti6Al4V and reported that machined specimens can have many different complementary failure origins that expand scatter in the fatigue responses.

Specimens with the smallest thickness (3 mm) had lower fatigue life due to two primary factors. First, the 3 mm diameter was the only size that exhibited rogue defects. These exceptionally large defects were located at the core of some of the 3 mm specimens and served as dominant origins in several cases. When not the origin, these large interior voids reduced the effective load-bearing cross-section that increased the true applied stress level. Secondly, after crack initiation, the stress intensity caused by a crack in a small cross-section will be larger than in a larger specimen due to boundary effects; the crack will propagate more quickly, thereby resulting in lower propagation life [135,136]. Another factor to consider is the increased surface roughness of printed parts with thinner nominal dimensions [130]. Although the surface roughness was not measured on the as-built samples in the present study, it has been shown in related studies that the increased roughness of thin specimens was sufficient to reduce the fatigue life [123,130].

Radial distance was the most influential factor to the fatigue life, which decreased with increasing radial distance for both the as-built and machined conditions. Results for the machined condition are shown in Figure 5.16. Unlike the underlying effect from part thickness, the effects of radial distance were not related to rogue defects. The effects of radial distance across the thickness at stress levels of 1000 and 600 MPa are shown in Figure 5.16a and 5.16b, respectively. As evident from this figure, there is a reduction in fatigue life with decreasing thickness for both stress levels.

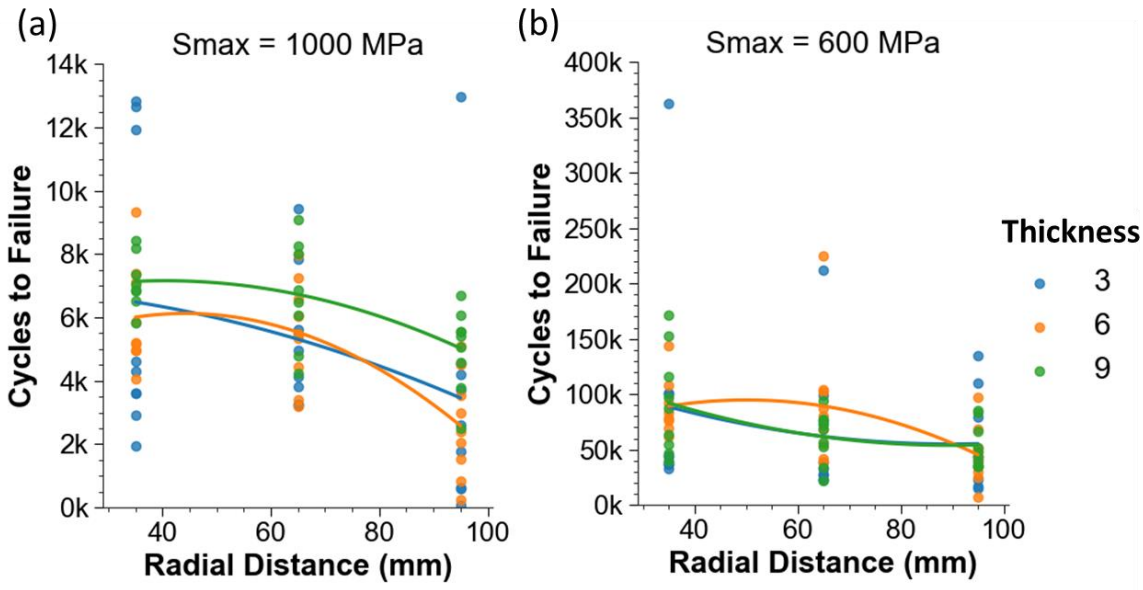

Figure 5.16. Cycles to failure of machined specimens as a function of radial distance for each thickness level, **(a)** 1000 and **(b)** 600 MPa max stress levels.

There are several potential explanations for the lower fatigue life of the specimens built with larger radial distance. First, the electron beam exits from the column hundreds of millimeters above the build layer. The beam will have an increasing angle of incidence with the powder bed as the distance from the center of the build plate increases, which coincides with greater radial distance. Energy absorption from the e-beam into the metal powder will decrease with the larger incident angle [137] and the meltpool geometry could become shallower due to the decreased energy and distribution of electrons [138]. This could also cause LOF defects because they generate as a function of low absorbed energy and reduced penetration [33]. Another possibility is the greater potential for powder spreading irregularities at the outermost radial distance. If underdosing powder, the powder spread to the opposite edge of the fetching side could be sparse or incomplete. Low density powder layers result in defects since an inadequate amount of material is available to be melted [77]. However, insufficient powder

spread is unlikely in this investigation since it occurred over three separate builds. Each build requires rake position calibration during which the operator ensures powder fully covers the build plate. Furthermore, the ARCAM A2X has a feedback loop system to automatically adjust the rake position to compensate for low powder dosing.

Build height is the third potential factor, which had no significant effects on the fatigue life distribution. Interestingly, there was a clear inverse quadratic trend between defect size and height as seen in Figure 5.7b. Nevertheless, the smaller defect size at the middle height level was not sufficient to influence the fatigue life, regardless of the various stress levels evaluated.

5.5.2 *Porosity Analysis*

Identifying measures to quantify the severity of pores/voids to the fatigue response is equally important to understanding their distribution. However, the severity of pores/voids is a complicated metric to define. Their physical size has been considered by many to be the dominant factor contributing to the fatigue life of AM metals, whereas others incorporate additional characteristics into the description of defect severity. Stress concentration factors and stress intensity factors are two metrics that can be applied to pores/voids, whether they are internal or at the surface. Stress concentration factors are the appropriate metric to use for most pore and void geometries. According to the classical definition, stress intensity factors can only be applied to cracks that exhibit an infinitesimally small crack-tip radius of curvature.

Several studies that have pursued an evaluation of defect severity for AM metals have applied both stress intensity and stress concentration definitions. The most prevalent of the treatments applied a modified linear elastic fracture mechanics (LEFM) approach to inclusions and pores in metals [128]. According to LEFM, the stress intensity factor for a planar crack with circular geometry in an infinite plate is described by:

$$K = FS\sqrt{\pi a} \tag{5.4}$$

where, *K* is the stress intensity factor, *F* is the geometric factor, *S* is the global applied stress that is perpendicular to the crack plane, and *a* is the radius of the crack [135]. A modified version was proposed by Murakami and Endo [132] to micro-scale defects, where the *a* is replaced with $\sqrt{area}$ (Eq. 5.5); the "area" is the projected area of the defect onto the plane perpendicular to the direction of loading, akin the crack length, as shown in Figure 5.7. Including this modification, the stress intensity of LOF voids is described by:

$$K = FS\sqrt{\pi\sqrt{area}} \tag{5.5}.$$

According to this quantitative description of the contribution of pore/void size, it would be expected that the trend in fatigue life of the specimens would be inversely related to the defect size based on the increase in apparent stress intensity. Indeed, the as-built and machined specimens with 3 mm thickness that contained rogue defects demonstrated the worst fatigue performance. However, for the as-built specimens the rogue defects did not serve as the origin of failure. For the as-built condition the fractographic markings showed that the origins of failure were located at the surface (Figure 5.11). Hence, there was a detrimental effect from the internal defects, but it was not the apparent stress intensity of these defects that caused a reduction in fatigue life.

There are three ways that the rogue defects caused a reduction in the fatigue life of the metal in the as-built condition. First, by occupying a substantial portion (>10 %) of the cross-section, they amplified the axial stress (>11 %) due to the reduced cross-sectional area, which was not accounted for in the estimated cyclic stress. Secondly, the geometry of these defects causes an internal stress concentration that further increases the localized stress. And thirdly, after fatigue

crack initiation from the various surface origins, the growth rate was increased due to the higher stress and stress intensity [81,116]. Thus, a combination of factors was responsible for the reduction in fatigue life of the specimens with lowest thickness (3 mm) in relation to the other two levels. These factors would also apply to structure components with small cross sections.

For the machined specimens there were fewer surface defects to serve as the initiation sites for fatigue cracks. As a result, the machined specimens exhibited longer life and initiation more frequently occurred from origins within the interior. Rogue defects were not the only source of fatigue crack initiation. Many of the machined specimens had one or multiple dominate LOF voids as shown in Figure 5.17. Fractograhic evaluation of the machined specimens showed that fracture is often facilitated by synergistic interaction of many LOF voids that exist on multiple planes. These are multi-site fracture origins in which cracks propagate until they bridge between multiple planes. As shown for the specimen in Figure 5.18, there is a cluster of LOF voids in the upper right quadrant of the fracture surface, which served as a distributed origin. Cracks propagated independently from these defects until they were able to interconnect.

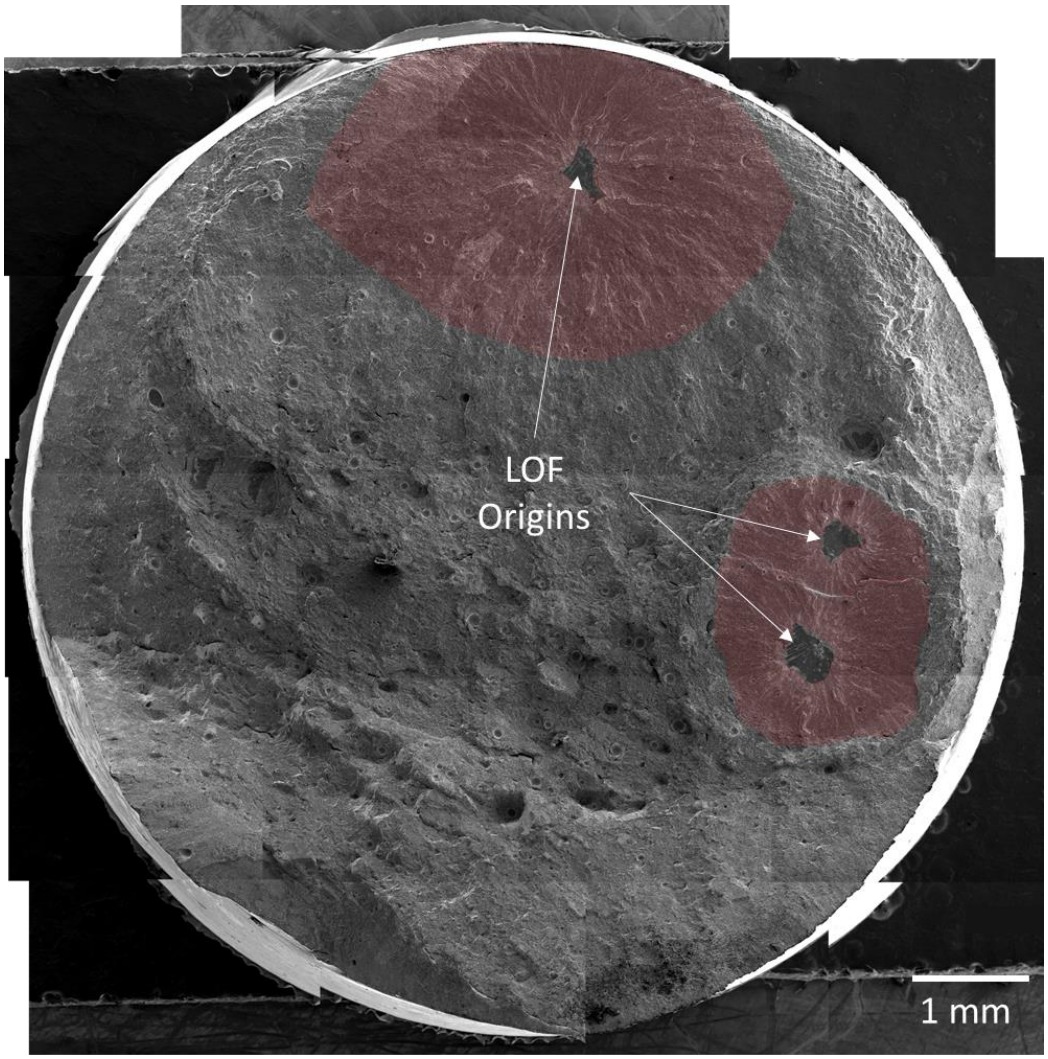

Figure 5.17. Composite SEM fractography of a machined 9 mm thickness part that was subjected to a max stress of 600 MPa. Red regions are areas of fracture crack growth emanating from the LOF defects indicated by white arrows.

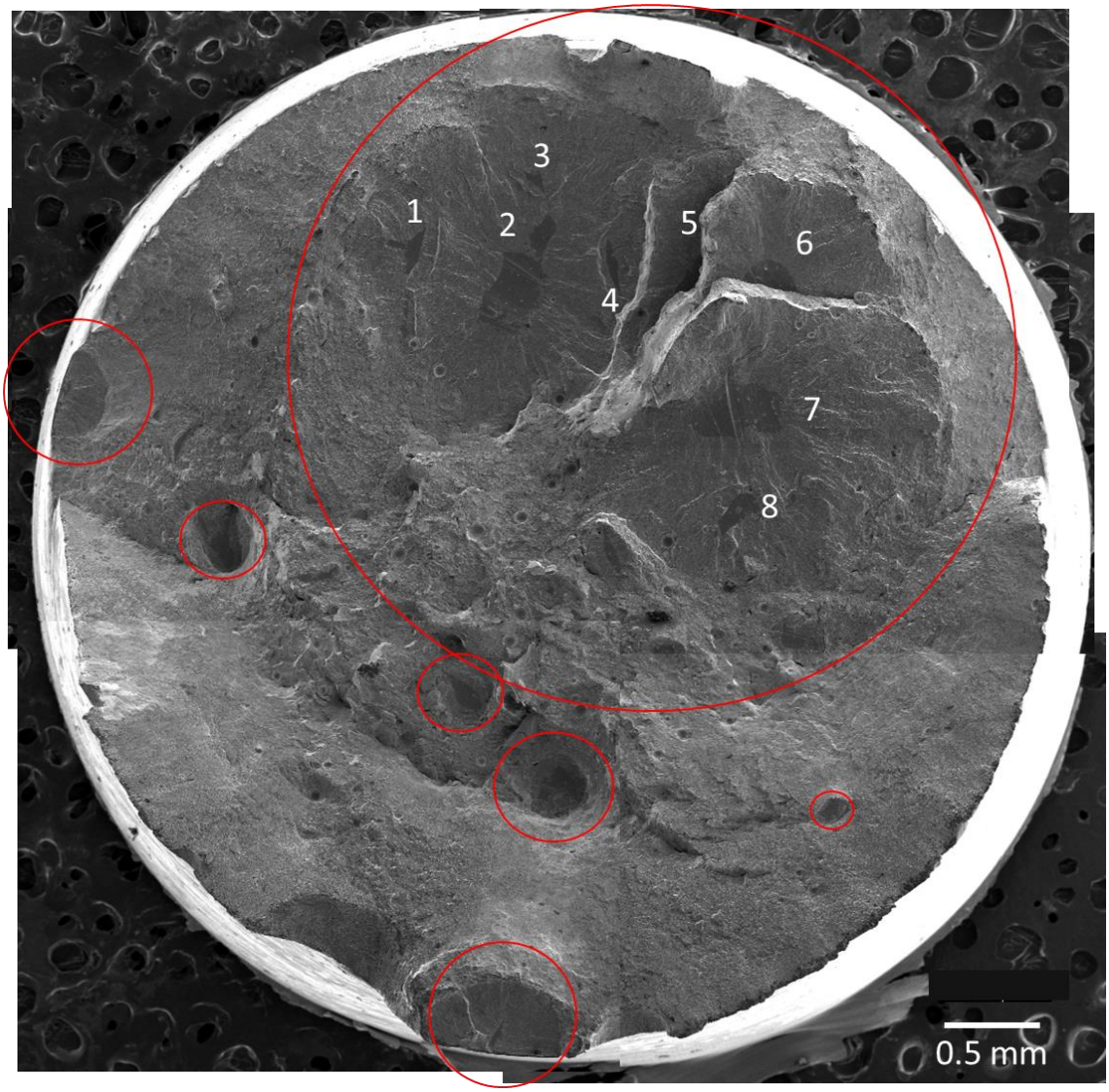

Figure 5.18. Composite SEM fractography of a machined 6 mm thick specimen that was subjected to a max stress of 1000 MPa. Circled in red are the apparent origins, all stemming from enclosed or surface exposed LOF void. All dominant origins within the large cluster of voids located in the upper right quadrant are numbered.

Although several studies have applied the $\sqrt{area}$ treatment of pores to assess the mechanical behavior of AM metal [82,125,129], there are limitations to this approach. Murakami

et al. have extensively investigated the effects of small defects in metallic materials on the fatigue performance, including application of the $\sqrt{area}$ definition [139–141]. They have acknowledge the limitations of the $\sqrt{area}$ parameter [83] especially for very irregular pores, and worked to expand upon the original description [132]. Indeed, the defects produced by EBM can be complex and accounting for the projected area alone on the plane of maximum normal stress is potentially an oversimplification. The Murakami equation (Eqn. 5.5) does not capture the effects of potentially detrimental attributes of the pores, such as location, geometry, and clusters [69,82,83,126]. Further improvements are necessary to obtain a model that can accurately predict fatigue life from defect distributions.

Finite element analysis of micro-scale defects has shown that the stress concentration of internal voids will increase substantially as they approach the surface of the component [69,82]. Defects located near the surface, deemed “near-surface” defects, can pose stress concentrations that are multiple times greater than internal defects located far from the free-surface boundaries. There is a sharp increase in stress concentration when the ratio of distance between the defect and part surface to the pore diameter decreases below 1 [82]. Furthermore, the magnitude of stress concentration grows asymptotically as the distance ratio approaches 0. Thus, post-process machining that is applied to improve surface quality can inadvertently transition internal pores to “near-surface” defects and have detrimental consequences.

To determine the relative contributions of pore characteristics, linear regression was applied to the XCT porosity and fatigue data. A power law relationship was found between the defects and cycles to failure in the present data, corroborating findings from other researchers [82]. A log transformation of the power law equation results in a linear relationship and allows for application of linear regression A semi-empirical equation for the fatigue life in terms of the

Basquin model and three pore characteristics that reflect the size, location, and morphology is given by

$$\begin{aligned} log_{10}(Nf) = \ & 21.89 - 6.20(log_{10}(S_{max})) \\ & - 0.29(log_{10}(\sqrt{area})) \\ & + 0.40(log_{10}(Sphericity)) \\ & + 0.11(log_{10}(Edge\ Distance)) \end{aligned} \quad (5.6).$$

As evident from the fit coefficients, the stress level (S_{max}) accounts for the major portion of the fatigue life response in the model. Addition of the pore characteristics enhance the model to encompass portions of the data that are influenced by these parametric effects. A comparison of the experimental fatigue life responses with the Basquin model is shown in Figure 5.19a. The degradation in fatigue life caused by the rogue defects is evident. By including porosity into the fatigue life relationship, the degradation caused by the rogue defects is apparent. As evident in Figure 5.19b, the specimens with rogue defects are more consistent with the regression fit and exhibit a similar effect to having a specimen at a higher stress level. In general, these extreme defects posed a greater maximum cyclic stress and stress amplitude that reduces the fatigue life. Based on the model, the effective increase in stress caused by these defects is approximately 200 MPa, which is not acceptable. Even for the specimens with only LOF defects, the data is spread along the regression line, implying that the stress concentration posed by the largest pores in these specimens causes an amplification of the applied stress level.

Utilizing XCT data to model or manage the influence of porosity/voids on the fatigue life response appears promising. However, there are currently limitations to this approach. One

concern is that surface defects are generally not captured in these evaluations of porosity since post-process rendering only characterizes defects that are enclosed by material. In addition, all specimens had contributing surface origins, which are not included in the regression model and possibly contribute to the variability in the data. A notch root radius calculation could be used to estimate the maximum stress concentration of the surface or identify voids with sharp tips that should be treated as a stress intensity. Yet, that requires an inspection technique with resolution capable of capturing the notch root radius. Another concern is that the quantitative descriptions of porosity are generally limited by the way the metrics can be assessed. For instance, the proximity between pores could contribute to the fatigue life [82,83]. The current algorithm for quantifying the proximity of pores in 3D space is based on the distance of minimal encompassing spheres. The limitation is that the distance is the nearest vectorial distance and not defined with respect to the component or build coordinate directions. As such, this proximity metric has limitations in assessing the defect severity and was neglected in the current model. A description for the proximity of pores within the same plane (i.e. plane of maximum normal stress), or within adjacent build layers are more relevant [83]. Therefore, complementary work focused on defect geometry, defect interactions and their contribution to the fatigue performance of EBM and other AM metals could be valuable.

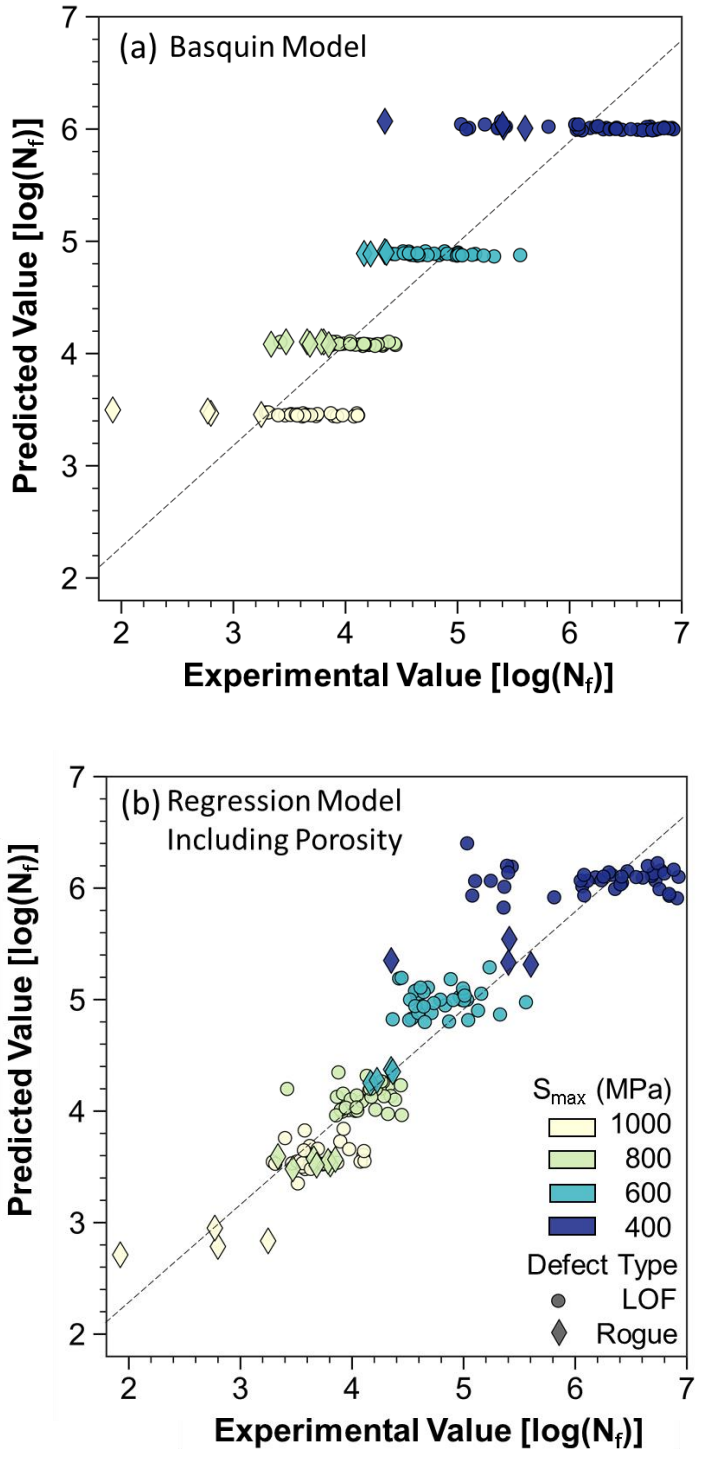

Figure 5.19. Comparison of predicted values against experimental values for (a) the Basquin model and (b) the linear regression model that accounts for porosity characteristics (Eqn. 5.6).

Based on their potential to pose large stress concentrations, the high density of near-surface pores in the EBM printed metal (Figure 5.9) is a concern. Machining to a sufficient depth to eliminate the stress concentration inherent of the surface texture is necessary and can improve the fatigue life substantially as shown in Figure 5.4. However, a region of high pore density lies below the surface texture that could become exposed by machining as shown in Figure 5.20. If the subsurface porosity cannot be avoided through processing conditions, post-process machining to remove the surface roughness but not expose any LOF voids could be applied to maximize the fatigue resistance. Based on the random nature of pore distributions, this may not be possible without the exposing some LOF voids that become surface defects with much larger stress concentrations. Again, if the subsurface porosity cannot be eliminated during the build, then machining should be performed to the depth that minimizes the near-surface stress concentrations. That approach requires that the internal pore distribution of components is known prior to post-process machining to choose the appropriate depth of material removal. Using the group of fatigue specimens as an example, the recommended depth of machining is shown in Figure 5.20.

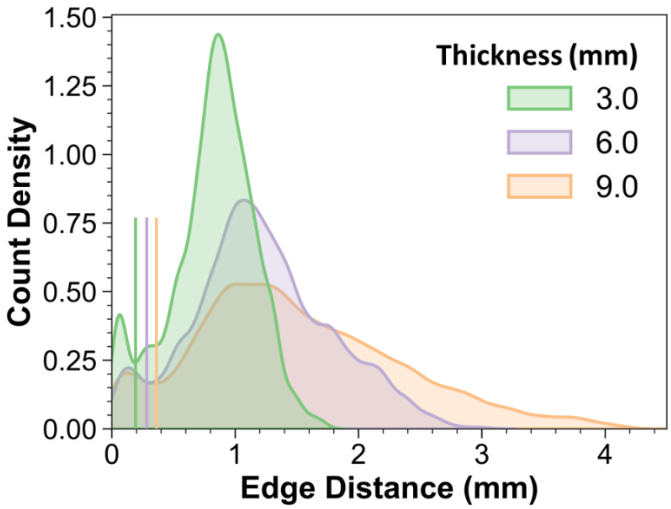

Figure 5.20. Count density plot as a function of edge distance for as-built specimens (pores restricted to $\sqrt{area} > 0.1$ mm). The three vertical lines indicate the local minimum of porosity and could serve as guideline depths for machining to minimize the number of near-surface defects.

5.6 CONCLUSIONS

While significant effort is being focused on optimizing the process parameters in metal AM processes, relatively limited effort has been placed on understanding the influence of core design parameters on the fatigue life distribution and part reliability. The latter approach is key to industrializing this manufacturing process and enabling its use as a production process today. Build design parameters including part thickness and part location in the build space are often neglected in studies focused on the manufacture of parts for stress-critical applications. This phase of the investigation was focused on determining the effects of these key build design parameters on the fatigue performance of Grade 5 Ti6Al4V produced by EBM. The conclusions from this effort are:

- Thickness and radial distance had strong effects on the fatigue life of the metal in both the as-built and machined conditions.
    - The fatigue strength decreased with decreasing specimen diameter. The cause of this trend was the relative increase in defect size with respect to the part cross-section.
    - The smallest diameter specimens (3 mm diameter) had a greater number of large internal “rogue” defects, which increased the effective stress in as-built samples and served as origins for fatigue crack initiation in the machined samples.

  - The fatigue strength of the metal decreased with increasing radial distance from the center of the build plate.

- For the fatigue specimens evaluated in the as-built condition, the surface texture served as the origin of failure. Stress concentrations were posed by the surface texture that caused that served as sites for fatigue crack initiation sites and caused substantial reductions in the fatigue life.
  - The fatigue life of the as-built condition is significantly lower than that of in the post-machined condition and is comparable to cast Ti6Al4V parts and components.
  - Machining of the surface improves the fatigue resistance and results in part performance that is comparable to wrought annealed Ti6Al4V.
  - A post-process surface treatment is essential for metal components produced by EBM and intended for stress-critical applications.
- It is essential to understand the location of the internal pores/voids to optimize the post-process machining.
  - The depth of machining must be adequate to remove the defects inherent of the surface but avoid relieving the near-surface defects that are concentrated beneath the free surface.
- Further analysis of defect distributions is necessary to develop predictive models that can account for their contribution to the fatigue properties. The important parameters to account for include the pore/void size, their location relative to the surface of the part, the in-plane morphology and their proximity to each other. In addition to internal defects, it is essential to account for surface relieved pores that are generally not adequately identified by XCT.

Chapter 6. CONCLUSIONS

6.1 VARIABILITY IN ELECTRON BEAM MELTING OF TI6AL4V

Novel contributions to the body of knowledge for mechanical variability in electron beam melting (EBM) of Ti6Al4V were presented and discussed throughout this thesis. Powder reuse has been investigated by several research groups, but these prior efforts did not involve extensive study of the microstructure and defects. Similarly, the comprehensive design of experiments (DOE) performed with build space parameters expands upon literature by mapping a majority of the build envelope and providing clear guidelines for design engineers when planning builds on an EBM machine. Together these experiments provide a basis for minimizing mechanical variability and allows for more emphasis to be placed on reducing variability from other sources, bringing AM of titanium one step closer to industrialization.

6.1.1 *Powder Reuse and Inter-build Variability*

Inter-build variability is the inconsistency in process and resulting mechanical properties between builds. There are several avenues for process and property variability from build to build. Assuming that many of the potential sources for inter-build variability are strictly controlled (e.g. machine condition, laser power decline, etc), as necessary for stringent industrial applications, only a few factors remain. Prominent amongst the remaining sources of variability is feedstock reuse.

To offset the high cost of powder feedstock in the printing of nickel and titanium alloys, there is a need to reuse feedstock material that is not part of the printed component geometry. For PBF, the feedstock to reuse is the powder that remains in the build chamber. Determining the

effects of this reuse is necessary before further adoption. It is necessary to develop process bounds for powder reuse, such that the properties of printed parts meet required standards.

In the first half of this investigation, the effects of powder reuse on several aspects of the printed material and its mechanical properties were determined. Two core conclusions, relevant to industrial users of the information, were found regarding powder reuse:

1. A linear increase in oxygen content occurred with increasing build number, which resulted in coarsened alpha laths of the metal. Hence, the oxygen content of the powder must be monitored and the powder must be replaced or supplemented with unused (low oxygen content) powder periodically.
2. There were no trends between the metal porosity and extent of powder reuse in this investigation. Quality control via nondestructive inspection is still necessary, but there is no detrimental increase in porosity with powder reuse.

6.1.2 *Build Design Parameters and Intra-build Variability*

There are clear constraints on maintaining high levels of metal quality and performance build-to-build. Yet, there are also concerns of quality and property variability within a single build (intra-build). Often ignored are simplistic build design considerations and their effects. Component geometry and its orientation have been investigated, but location of the component in the build and their proximity to one another are seldom considered. Therefore, a design of experiments approach was adopted to determine the relative influence of the build design parameters on the printed metal.

There were large ranges in the mechanical properties of metal resulting from a single build. For monotonic loading, the elongation at failure experienced significant variance, ranging down to 1.5 %, which is not acceptable for damage tolerant applications. Similarly, there was substantial

scatter in the fatigue life distribution, with range in cycles to failure that exceeded the mean life. In general, a substantial contribution to the variability in mechanical behavior was the extreme porosity in parts with low thickness, and the proximity of pores to the edge of the build plane.

These results do not support the use of witness coupons placed in the build space and the belief they are indicative of the metal in other parts within the print. In general, these test articles would be placed near the edge of the build space to minimize obstruction to other components, which would result in very poor predictions of the ductility and strength with respect to metal build closer to the center of the build envelope. Furthermore, the thickness and orientation of the test coupon must be considered as they were identified to be important contributors to the mechanical behavior.

Based on the experimental results and the regression models developed for the two DOE, stress-critical parts intended for mission-critical applications should be located at the center of the build plane, near the bottom of the build space, and have thickness of at least 4.5 mm. Apart from the factors with substantial effects of metal quality and its mechanical behavior, it was determined that component spacing (proximity) has minimal influence. Hence, it is appropriate for builds to be designed with high part density for increased cost efficiency in EBM of Ti6Al4V.

Variability within a build is dominated by porosity, with size of the pore in the plane perpendicular to loading being most important. Other key characteristics include morphology, location relative to the surface, and proximity to other pores. Despite not capturing porosity that was exposed to the free surface and clustering of pores, the updated model that accounted for these other pore characteristics had improved capacity for predicting the fatigue life. Capturing pores via X-ray CT is a necessary technique for industry to predict responses.

6.2 FUTURE DIRECTIONS

6.2.1 *Powder Refreshing*

From the two major conclusions of powder reuse, it is recommended that industrial users focus efforts on developing appropriate powder recycling procedures. Further studies should be performed to determine the optimal procedures of blending virgin powder as oxygen uptake is likely tied to beam exposure time and time exposed to recovery. It is expected that larger builds will be more problematic in this regard than the small one utilized in this study. Additionally, studies are needed to determine if there is a method of negating the uptake of oxygen, whether through processing of the powder or replenishment with low oxygen powder.

6.2.2 *Confirming the Contribution of Build Design Parameters*

Build design was shown to be an important consideration when printing with EBM, but is it prevalent or an isolated case? Machine-to-machine variability is another area that was not addressed in the present study. It is reasonable to assume that the regression models determined for build design parameters on the Arcam A2X is not the same as the Q20, or even another A2X. Applying the same or similar DOE to other machines could be valuable at reinforce the findings established here or could show that the EBM machine used for this study was unique.

Compensating for the effects in the build space parameters could alleviate concerns of intra-build variability. Although the Arcam A2X is periodically calibrated to provided uniform power of the beam across the build plane, it may require further improvement to overcome the printing of poor metal quality near the periphery. In addition, hot isotatic pressing (HIP) is known to be capable of closing pores and improving the fatigue life [36], which makes it an ideal candidate to reduce the intra-build variability. A future study could be performed to establish that HIP can

eliminate concerns surrounding the build design and facilitate the manufacture of parts that take advantage of the many benefits of AM but also with highly uniform and reliable properties.

6.2.3 *Machine Parameters*

To avoid unwanted variability from other sources, many machine parameters were held constant in this investigation. An analysis of the effects from these neglected factors should be conducted to expand the understanding of variability in the EBM process with Ti6Al4V. Frequently investigated in this field are the beam parameters and scanning strategies, which have shown strong influence on part performance [33,78]. Other parameters such as preheating and powder spreading were not considered and need further investigation. Furthermore, there is a need to determine the cumulative influence of machine parameters and build space parameters.

6.2.4 *Machine Learning Development*

As illustrated throughout the previous chapters, there are a number of challenges to overcome in EBM of Ti6Al4V. There is a substantial degree of variability in the metal quality and mechanical properties in EBM of Ti6Al4V. The variability originates from factors that contribute within a build and between builds. Numerous factors, their subsequent effects on the metal microstructure, and resulting mechanical performance present a high-dimensional data problem that must be solved. A rather basic application of machine learning (ML) was adopted to support data analysis in the present investigation, which proved to be a useful tool. A more comprehensive effort involving ML should be pursued with growth in the dataset and an understanding of the underlying goals.

BIBLIOGRAPHY

[1] D.L. Bourell, Perspectives on Additive Manufacturing, Annual Review of Materials Research. 46 (2016) 1–18. https://doi.org/10.1146/annurev-matsci-070115-031606.

[2] B.P. Conner, G.P. Manogharan, A.N. Martof, L.M. Rodomsky, C.M. Rodomsky, D.C. Jordan, J.W. Limperos, Making sense of 3-D printing: Creating a map of additive manufacturing products and services, Additive Manufacturing. 1–4 (2014) 64–76. https://doi.org/10.1016/j.addma.2014.08.005.

[3] H. Bikas, P. Stavropoulos, G. Chryssolouris, Additive manufacturing methods and modelling approaches: a critical review, Int J Adv Manuf Technol. 83 (2016) 389–405. https://doi.org/10.1007/s00170-015-7576-2.

[4] T. Wohlers, T. Caffrey, R.I. Campbell, O. Diegel, J. Kowen, Wohlers Report 2018: 3D Printing and Additive Manufacturing State of the Industry; Annual Worldwide Progress Report, Wohlers Associates, 2018.

[5] D.D. Gu, W. Meiners, K. Wissenbach, R. Poprawe, Laser additive manufacturing of metallic components: materials, processes and mechanisms, International Materials Reviews. 57 (2012) 133–164. https://doi.org/10.1179/1743280411Y.0000000014.

[6] D. Herzog, V. Seyda, E. Wycisk, C. Emmelmann, Additive manufacturing of metals, Acta Materialia. 117 (2016) 371–392. https://doi.org/10.1016/j.actamat.2016.07.019.

[7] Sing Swee Leong, An Jia, Yeong Wai Yee, Wiria Florencia Edith, Laser and electron-beam powder-bed additive manufacturing of metallic implants: A review on processes, materials and designs, Journal of Orthopaedic Research. 34 (2015) 369–385. https://doi.org/10.1002/jor.23075.

[8] L.E. Murr, E. Martinez, K.N. Amato, S.M. Gaytan, J. Hernandez, D.A. Ramirez, P.W. Shindo, F. Medina, R.B. Wicker, Fabrication of Metal and Alloy Components by Additive Manufacturing: Examples of 3D Materials Science, Journal of Materials Research and Technology. 1 (2012) 42–54. https://doi.org/10.1016/S2238-7854(12)70009-1.

[9] W. Gao, Y. Zhang, D. Ramanujan, K. Ramani, Y. Chen, C.B. Williams, C.C.L. Wang, Y.C. Shin, S. Zhang, P.D. Zavattieri, The status, challenges, and future of additive manufacturing in engineering, Computer-Aided Design. 69 (2015) 65–89. https://doi.org/10.1016/j.cad.2015.04.001.

[10] T.D. Ngo, A. Kashani, G. Imbalzano, K.T.Q. Nguyen, D. Hui, Additive manufacturing (3D printing): A review of materials, methods, applications and challenges, Composites Part B: Engineering. 143 (2018) 172–196. https://doi.org/10.1016/j.compositesb.2018.02.012.

[11] W.E. Frazier, Metal Additive Manufacturing: A Review, J. of Materi Eng and Perform. 23 (2014) 1917–1928. https://doi.org/10.1007/s11665-014-0958-z.

[12] X. Gong, T. Anderson, K. Chou, Review on Powder-Based Electron Beam Additive Manufacturing Technology, (2012) 507–515. https://doi.org/10.1115/ISFA2012-7256.

[13] W.E. King, A.T. Anderson, R.M. Ferencz, N.E. Hodge, C. Kamath, S.A. Khairallah, A.M. Rubenchik, Laser powder bed fusion additive manufacturing of metals; physics, computational, and materials challenges, Applied Physics Reviews. 2 (2015) 041304. https://doi.org/10.1063/1.4937809.

[14] T. DebRoy, H.L. Wei, J.S. Zuback, T. Mukherjee, J.W. Elmer, J.O. Milewski, A.M. Beese, A. Wilson-Heid, A. De, W. Zhang, Additive manufacturing of metallic components

– Process, structure and properties, Progress in Materials Science. 92 (2018) 112–224. https://doi.org/10.1016/j.pmatsci.2017.10.001.
[15] H.K. Rafi, N.V. Karthik, H. Gong, T.L. Starr, B.E. Stucker, Microstructures and Mechanical Properties of Ti6Al4V Parts Fabricated by Selective Laser Melting and Electron Beam Melting, J. of Materi Eng and Perform. 22 (2013) 3872–3883. https://doi.org/10.1007/s11665-013-0658-0.
[16] N. Hrabe, T. Quinn, Effects of processing on microstructure and mechanical properties of a titanium alloy (Ti–6Al–4V) fabricated using electron beam melting (EBM), part 1: Distance from build plate and part size, Materials Science and Engineering: A. 573 (2013) 264–270. https://doi.org/10.1016/j.msea.2013.02.064.
[17] A.A. Antonysamy, J. Meyer, P.B. Prangnell, Effect of build geometry on the β-grain structure and texture in additive manufacture of Ti6Al4V by selective electron beam melting, Materials Characterization. 84 (2013) 153–168. https://doi.org/10.1016/j.matchar.2013.07.012.
[18] N. Hrabe, T. Quinn, Effects of processing on microstructure and mechanical properties of a titanium alloy (Ti–6Al–4V) fabricated using electron beam melting (EBM), Part 2: Energy input, orientation, and location, Materials Science and Engineering: A. 573 (2013) 271–277. https://doi.org/10.1016/j.msea.2013.02.065.
[19] H.P. Tang, M. Qian, N. Liu, X.Z. Zhang, G.Y. Yang, J. Wang, Effect of Powder Reuse Times on Additive Manufacturing of Ti-6Al-4V by Selective Electron Beam Melting, JOM. 67 (2015) 555–563. https://doi.org/10.1007/s11837-015-1300-4.
[20] N. Shen, K. Chou, Thermal Modeling of Electron Beam Additive Manufacturing Process: Powder Sintering Effects, (2012) 287–295. https://doi.org/10.1115/MSEC2012-7253.
[21] C. Körner, Additive manufacturing of metallic components by selective electron beam melting — a review, International Materials Reviews. 61 (2016) 361–377. https://doi.org/10.1080/09506608.2016.1176289.
[22] C. Wei, X. Ma, X. Yang, M. Zhou, C. Wang, Y. Zheng, W. Zhang, Z. Li, Microstructural and property evolution of Ti6Al4V powders with the number of usage in additive manufacturing by electron beam melting, Materials Letters. 221 (2018) 111–114. https://doi.org/10.1016/j.matlet.2018.03.124.
[23] V.V. Popov, A. Katz-Demyanetz, A. Garkun, M. Bamberger, The effect of powder recycling on the mechanical properties and microstructure of electron beam melted Ti-6Al-4 V specimens, Additive Manufacturing. 22 (2018) 834–843. https://doi.org/10.1016/j.addma.2018.06.003.
[24] Y. Sun, M. Aindow, R.J. Hebert, The effect of recycling on the oxygen distribution in Ti-6Al-4V powder for additive manufacturing, Materials at High Temperatures. 35 (2018) 217–224. https://doi.org/10.1080/09603409.2017.1389133.
[25] L.C. Ardila, F. Garciandia, J.B. González-Díaz, P. Álvarez, A. Echeverria, M.M. Petite, R. Deffley, J. Ochoa, Effect of IN718 Recycled Powder Reuse on Properties of Parts Manufactured by Means of Selective Laser Melting, Physics Procedia. 56 (2014) 99–107. https://doi.org/10.1016/j.phpro.2014.08.152.
[26] P.D. Nezhadfar, A. Soltani-Tehrani, A. Sterling, N. Tsolas, N. Shamsaei, The Effects of Powder Recycling on the Mechanical Properties of Additively Manufactured 17-4 PH Stainless Steel, (2018) 9.
[27] P. Nandwana, W.H. Peter, R.R. Dehoff, L.E. Lowe, M.M. Kirka, F. Medina, S.S. Babu, Recyclability Study on Inconel 718 and Ti-6Al-4V Powders for Use in Electron Beam

Melting, Metall and Materi Trans B. 47 (2016) 754–762. https://doi.org/10.1007/s11663-015-0477-9.
[28] L. Grainger, Investigating the effects of multiple re-use of Ti6Al4V powder in additive manufacturing (AM), Renishaw Plc. (2016).
[29] R.-P. Guo, L. Xu, B.Y.-P. Zong, R. Yang, Characterization of Prealloyed Ti–6Al–4V Powders from EIGA and PREP Process and Mechanical Properties of HIPed Powder Compacts, Acta Metallurgica Sinica (English Letters). 30 (2017) 735–744. https://doi.org/10.1007/s40195-017-0540-4.
[30] S. Liu, Y.C. Shin, Additive manufacturing of Ti6Al4V alloy: A review, Materials & Design. 164 (2019) 107552. https://doi.org/10.1016/j.matdes.2018.107552.
[31] R. Cunningham, A. Nicolas, J. Madsen, E. Fodran, E. Anagnostou, M.D. Sangid, A.D. Rollett, Analyzing the effects of powder and post-processing on porosity and properties of electron beam melted Ti-6Al-4V, Materials Research Letters. 5 (2017) 516–525. https://doi.org/10.1080/21663831.2017.1340911.
[32] R. Cunningham, S.P. Narra, T. Ozturk, J. Beuth, A.D. Rollett, Evaluating the Effect of Processing Parameters on Porosity in Electron Beam Melted Ti-6Al-4V via Synchrotron X-ray Microtomography, JOM. 68 (2016) 765–771. https://doi.org/10.1007/s11837-015-1802-0.
[33] H. Gong, K. Rafi, H. Gu, T. Starr, B. Stucker, Analysis of defect generation in Ti–6Al–4V parts made using powder bed fusion additive manufacturing processes, Additive Manufacturing. 1–4 (2014) 87–98. https://doi.org/10.1016/j.addma.2014.08.002.
[34] G. Chen, Q. Zhou, S.Y. Zhao, J.O. Yin, P. Tan, Z.F. Li, Y. Ge, J. Wang, H.P. Tang, A pore morphological study of gas-atomized Ti-6Al-4V powders by scanning electron microscopy and synchrotron X-ray computed tomography, Powder Technology. 330 (2018) 425–430. https://doi.org/10.1016/j.powtec.2018.02.053.
[35] C. Guo, W. Ge, F. Lin, Effects of scanning parameters on material deposition during Electron Beam Selective Melting of Ti-6Al-4V powder, Journal of Materials Processing Technology. 217 (2015) 148–157. https://doi.org/10.1016/j.jmatprotec.2014.11.010.
[36] A.H. Chern, P. Nandwana, T. Yuan, M.M. Kirka, R.R. Dehoff, P.K. Liaw, C.E. Duty, A review on the fatigue behavior of Ti-6Al-4V fabricated by electron beam melting additive manufacturing, International Journal of Fatigue. 119 (2019) 173–184. https://doi.org/10.1016/j.ijfatigue.2018.09.022.
[37] R. Cunningham, S.P. Narra, C. Montgomery, J. Beuth, A.D. Rollett, Synchrotron-Based X-ray Microtomography Characterization of the Effect of Processing Variables on Porosity Formation in Laser Power-Bed Additive Manufacturing of Ti-6Al-4V, JOM. 69 (2017) 479–484. https://doi.org/10.1007/s11837-016-2234-1.
[38] S. Leuders, M. Thöne, A. Riemer, T. Niendorf, T. Tröster, H.A. Richard, H.J. Maier, On the mechanical behaviour of titanium alloy TiAl6V4 manufactured by selective laser melting: Fatigue resistance and crack growth performance, International Journal of Fatigue. 48 (2013) 300–307. https://doi.org/10.1016/j.ijfatigue.2012.11.011.
[39] A. du Plessis, P. Rossouw, X-ray computed tomography of a titanium aerospace investment casting, Case Studies in Nondestructive Testing and Evaluation. 3 (2015) 21–26. https://doi.org/10.1016/j.csndt.2015.03.001.
[40] A. Karme, A. Kallonen, V.-P. Matilainen, H. Piili, A. Salminen, Possibilities of CT Scanning as Analysis Method in Laser Additive Manufacturing, Physics Procedia. 78 (2015) 347–356. https://doi.org/10.1016/j.phpro.2015.11.049.

[41] K. Heim, F. Bernier, R. Pelletier, L.-P. Lefebvre, High resolution pore size analysis in metallic powders by X-ray tomography, Case Studies in Nondestructive Testing and Evaluation. 6 (2016) 45–52. https://doi.org/10.1016/j.csndt.2016.09.002.
[42] F.H. Kim, S.P. Moylan, E.J. Garboczi, J.A. Slotwinski, Investigation of pore structure in cobalt chrome additively manufactured parts using X-ray computed tomography and three-dimensional image analysis, Additive Manufacturing. 17 (2017) 23–38. https://doi.org/10.1016/j.addma.2017.06.011.
[43] S. Romano, A. Brandão, J. Gumpinger, M. Gschweitl, S. Beretta, Qualification of AM parts: Extreme value statistics applied to tomographic measurements, Materials & Design. 131 (2017) 32–48. https://doi.org/10.1016/j.matdes.2017.05.091.
[44] G. Vastola, Q.X. Pei, Y.-W. Zhang, Predictive model for porosity in powder-bed fusion additive manufacturing at high beam energy regime, Additive Manufacturing. 22 (2018) 817–822. https://doi.org/10.1016/j.addma.2018.05.042.
[45] C.J. Smith, F. Derguti, E. Hernandez Nava, M. Thomas, S. Tammas-Williams, S. Gulizia, D. Fraser, I. Todd, Dimensional accuracy of Electron Beam Melting (EBM) additive manufacture with regard to weight optimized truss structures, Journal of Materials Processing Technology. 229 (2016) 128–138. https://doi.org/10.1016/j.jmatprotec.2015.08.028.
[46] V.J. Challis, X. Xu, L.C. Zhang, A.P. Roberts, J.F. Grotowski, T.B. Sercombe, High specific strength and stiffness structures produced using selective laser melting, Materials & Design. 63 (2014) 783–788. https://doi.org/10.1016/j.matdes.2014.05.064.
[47] M. Barclift, A. Armstrong, T.W. Simpson, S.B. Joshi, CAD-Integrated Cost Estimation and Build Orientation Optimization to Support Design for Metal Additive Manufacturing, in: Volume 2A: 43rd Design Automation Conference, American Society of Mechanical Engineers, Cleveland, Ohio, USA, 2017: p. V02AT03A035. https://doi.org/10.1115/DETC2017-68376.
[48] X. Zhao, S. Li, M. Zhang, Y. Liu, T.B. Sercombe, S. Wang, Y. Hao, R. Yang, L.E. Murr, Comparison of the microstructures and mechanical properties of Ti–6Al–4V fabricated by selective laser melting and electron beam melting, Materials & Design. 95 (2016) 21–31. https://doi.org/10.1016/j.matdes.2015.12.135.
[49] T. Searles, J. Tiley, A. Tanner, R. Williams, B. Rollins, E. Lee, S. Kar, R. Banerjee, H.L. Fraser, Rapid characterization of titanium microstructural features for specific modelling of mechanical properties, Measurement Science and Technology. 16 (2005) 60–69. https://doi.org/10.1088/0957-0233/16/1/009.
[50] J.A. Slotwinski, E.J. Garboczi, P.E. Stutzman, C.F. Ferraris, S.S. Watson, M.A. Peltz, Characterization of Metal Powders Used for Additive Manufacturing, Journal of Research of the National Institute of Standards and Technology. 119 (2014) 460. https://doi.org/10.6028/jres.119.018.
[51] R.K. McGEARY, Mechanical Packing of Spherical Particles, J American Ceramic Society. 44 (1961) 513–522. https://doi.org/10.1111/j.1151-2916.1961.tb13716.x.
[52] H.Y. Sohn, C. Moreland, The effect of particle size distribution on packing density, The Canadian Journal of Chemical Engineering. 46 (1968) 162–167. https://doi.org/10.1002/cjce.5450460305.
[53] B. Liu, R. Wildman, C. Tuck, I. Ashcroft, R. Hague, Investigation the effect of particle size distribution on processing parameters optimisation in selective laser melting process, Additive Manufacturing Research Group, Loughborough University. (2011) 227–238.

[54] H. Conrad, Effect of interstitial solutes on the strength and ductility of titanium, Progress in Materials Science. 26 (1981) 123–403. https://doi.org/10.1016/0079-6425(81)90001-3.
[55] G. Welsch, R. Boyer, E.W. Collings, eds., Materials properties handbook: titanium alloys, ASM International, Materials Park, OH, 1994.
[56] M. Neikter, P. Åkerfeldt, R. Pederson, M.-L. Antti, Microstructure characterisation of Ti-6Al-4V from different additive manufacturing processes, IOP Conference Series: Materials Science and Engineering. 258 (2017) 012007. https://doi.org/10.1088/1757-899X/258/1/012007.
[57] A.I. Kahveci, G.E. Welsch, Effect of oxygen on the hardness and alpha/beta phase ratio of Ti-6Al-4V alloy, Scripta Metallurgica. 20 (1986) 1287–1290. https://doi.org/10.1016/0036-9748(86)90050-5.
[58] S.M. Kelly, S.L. Kampe, Microstructural evolution in laser-deposited multilayer Ti-6Al-4V builds: Part I. Microstructural characterization, Metallurgical and Materials Transactions A. 35 (2004) 1861–1867. https://doi.org/10.1007/s11661-004-0094-8.
[59] X. Tan, Y. Kok, Y.J. Tan, M. Descoins, D. Mangelinck, S.B. Tor, K.F. Leong, C.K. Chua, Graded microstructure and mechanical properties of additive manufactured Ti–6Al–4V via electron beam melting, Acta Materialia. 97 (2015) 1–16. https://doi.org/10.1016/j.actamat.2015.06.036.
[60] X. Tan, Y. Kok, W.Q. Toh, Y.J. Tan, M. Descoins, D. Mangelinck, S.B. Tor, K.F. Leong, C.K. Chua, Revealing martensitic transformation and α/β interface evolution in electron beam melting three-dimensional-printed Ti-6Al-4V, Scientific Reports. 6 (2016) 26039. https://doi.org/10.1038/srep26039.
[61] B. Vayre, F. Vignat, F. Villeneuve, Metallic additive manufacturing: state-of-the-art review and prospects, Mechanics & Industry. 13 (2012) 89–96. https://doi.org/10.1051/meca/2012003.
[62] M. Seifi, A. Salem, J. Beuth, O. Harrysson, J.J. Lewandowski, Overview of Materials Qualification Needs for Metal Additive Manufacturing, JOM. 68 (2016) 747–764. https://doi.org/10.1007/s11837-015-1810-0.
[63] H. Gruber, C. Luchian, E. Hryha, L. Nyborg, Effect of Powder Recycling on Defect Formation in Electron Beam Melted Alloy 718, Metall and Mat Trans A. 51 (2020) 2430–2443. https://doi.org/10.1007/s11661-020-05674-8.
[64] S. Ghods, E. Schultz, C. Wisdom, R. Schur, R. Pahuja, A. Montelione, D. Arola, M. Ramulu, Electron beam additive manufacturing of Ti6Al4V: Evolution of powder morphology and part microstructure with powder reuse, Materialia. 9 (2020) 100631. https://doi.org/10.1016/j.mtla.2020.100631.
[65] T. Kohonen, The self-organizing map, Proceedings of the IEEE. 78 (1990) 1464–1480. https://doi.org/10.1109/5.58325.
[66] J. Qian, N.P. Nguyen, Y. Oya, G. Kikugawa, T. Okabe, Y. Huang, F.S. Ohuchi, Introducing self-organized maps (SOM) as a visualization tool for materials research and education, Results in Materials. 4 (2019) 100020. https://doi.org/10.1016/j.rinma.2019.100020.
[67] R. Schur, S. Ghods, C. Wisdom, R. Pahuja, A. Montelione, D. Arola, M. Ramulu, Electron Beam Melting Additive Manufacturing of Ti6Al4V: Contributions of Powder Reuse to Mechanical Properties and their Variability, (n.d.).

[68] G. Nicoletto, G. Anzelotti, R. Konečná, X-ray computed tomography vs. metallography for pore sizing and fatigue of cast Al-alloys, Procedia Engineering. 2 (2010) 547–554. https://doi.org/10.1016/j.proeng.2010.03.059.
[69] R. Biswal, A.K. Syed, X. Zhang, Assessment of the effect of isolated porosity defects on the fatigue performance of additive manufactured titanium alloy, Additive Manufacturing. 23 (2018) 433–442. https://doi.org/10.1016/j.addma.2018.08.024.
[70] T. Davis, D. Healy, A. Bubeck, R. Walker, Stress concentrations around voids in three dimensions: The roots of failure, Journal of Structural Geology. 102 (2017) 193–207. https://doi.org/10.1016/j.jsg.2017.07.013.
[71] H. Yu, S. Hayashi, K. Kakehi, Y.-L. Kuo, Study of Formed Oxides in IN718 Alloy during the Fabrication by Selective Laser Melting and Electron Beam Melting, Metals. 9 (2019) 19. https://doi.org/10.3390/met9010019.
[72] J.L. Murray, H.A. Wriedt, The O−Ti (Oxygen-Titanium) system, JPE. 8 (1987) 148–165. https://doi.org/10.1007/BF02873201.
[73] G. Lindwall, P. Wang, U.R. Kattner, C.E. Campbell, The Effect of Oxygen on Phase Equilibria in the Ti-V System: Impacts on the AM Processing of Ti Alloys, JOM. 70 (2018) 1692–1705. https://doi.org/10.1007/s11837-018-3008-8.
[74] E.S. Bumps, H.D. Kessler, M. Hansen, Titanium-Aluminum System, JOM. 4 (1952) 609–614. https://doi.org/10.1007/BF03397728.
[75] S.D. Luo, T. Song, S.L. Lu, B. Liu, J. Tian, M. Qian, High oxygen-content titanium and titanium alloys made from powder, Journal of Alloys and Compounds. 836 (2020) 155526. https://doi.org/10.1016/j.jallcom.2020.155526.
[76] A. du Plessis, I. Yadroitsev, I. Yadroitsava, S.G. Le Roux, X-Ray Microcomputed Tomography in Additive Manufacturing: A Review of the Current Technology and Applications, 3D Printing and Additive Manufacturing. 5 (2018) 227–247. https://doi.org/10.1089/3dp.2018.0060.
[77] H.-W. Mindt, O. Desmaison, M. Megahed, A. Peralta, J. Neumann, Modeling of Powder Bed Manufacturing Defects, J. of Materi Eng and Perform. 27 (2018) 32–43. https://doi.org/10.1007/s11665-017-2874-5.
[78] S. Tammas-Williams, H. Zhao, F. Léonard, F. Derguti, I. Todd, P.B. Prangnell, XCT analysis of the influence of melt strategies on defect population in Ti–6Al–4V components manufactured by Selective Electron Beam Melting, Materials Characterization. 102 (2015) 47–61. https://doi.org/10.1016/j.matchar.2015.02.008.
[79] R.J. Bourcier, D.A. Koss, R.E. Smelser, O. Richmond, The influence of porosity on the deformation and fracture of alloys, Acta Metallurgica. 34 (1986) 2443–2453. https://doi.org/10.1016/0001-6160(86)90147-1.
[80] P. Kumar, K.S.R. Chandran, Strength–Ductility Property Maps of Powder Metallurgy (PM) Ti-6Al-4V Alloy: A Critical Review of Processing-Structure-Property Relationships, Metall and Mat Trans A. 48 (2017) 2301–2319. https://doi.org/10.1007/s11661-017-4009-x.
[81] P. Kumar, K.S. Ravi Chandran, F. Cao, M. Koopman, Z.Z. Fang, The Nature of Tensile Ductility as Controlled by Extreme-Sized Pores in Powder Metallurgy Ti-6Al-4V Alloy, Metall and Mat Trans A. 47 (2016) 2150–2161. https://doi.org/10.1007/s11661-016-3419-5.

[82] S. Tammas-Williams, P.J. Withers, I. Todd, P.B. Prangnell, The Influence of Porosity on Fatigue Crack Initiation in Additively Manufactured Titanium Components, Scientific Reports. 7 (2017). https://doi.org/10.1038/s41598-017-06504-5.
[83] H. Masuo, Y. Tanaka, S. Morokoshi, H. Yagura, T. Uchida, Y. Yamamoto, Y. Murakami, Influence of defects, surface roughness and HIP on the fatigue strength of Ti-6Al-4V manufactured by additive manufacturing, International Journal of Fatigue. 117 (2018) 163–179. https://doi.org/10.1016/j.ijfatigue.2018.07.020.
[84] B. Foster, E. Reutzel, A. Nassar, B. Hall, S. Brown, C. Dickman, Optical, layerwise monitoring of powder bed fusion, in: Solid Freeform Fabrication Symposium, Austin, TX, Aug, 2015: pp. 10–12.
[85] C. Gobert, E.W. Reutzel, J. Petrich, A.R. Nassar, S. Phoha, Application of supervised machine learning for defect detection during metallic powder bed fusion additive manufacturing using high resolution imaging., Additive Manufacturing. 21 (2018) 517–528. https://doi.org/10.1016/j.addma.2018.04.005.
[86] L. Scime, J. Beuth, Using machine learning to identify in-situ melt pool signatures indicative of flaw formation in a laser powder bed fusion additive manufacturing process, Additive Manufacturing. 25 (2019) 151–165. https://doi.org/10.1016/j.addma.2018.11.010.
[87] M. Khanzadeh, P. Rao, R. Jafari-Marandi, B.K. Smith, M.A. Tschopp, L. Bian, Quantifying Geometric Accuracy With Unsupervised Machine Learning: Using Self-Organizing Map on Fused Filament Fabrication Additive Manufacturing Parts, J. Manuf. Sci. Eng. 140 (2018). https://doi.org/10.1115/1.4038598.
[88] Z. Zhu, N. Anwer, Q. Huang, L. Mathieu, Machine learning in tolerancing for additive manufacturing, CIRP Annals. 67 (2018) 157–160. https://doi.org/10.1016/j.cirp.2018.04.119.
[89] S.R. Kalidindi, M. De Graef, Materials Data Science: Current Status and Future Outlook, Annu. Rev. Mater. Res. 45 (2015) 171–193. https://doi.org/10.1146/annurev-matsci-070214-020844.
[90] P. Nandwana, M.M. Kirka, V.C. Paquit, S. Yoder, R.R. Dehoff, Correlations Between Powder Feedstock Quality, In Situ Porosity Detection, and Fatigue Behavior of Ti-6Al-4V Fabricated by Powder Bed Electron Beam Melting: A Step Towards Qualification, JOM. 70 (2018) 1686–1691. https://doi.org/10.1007/s11837-018-3034-6.
[91] A. Saboori, D. Gallo, S. Biamino, P. Fino, M. Lombardi, An Overview of Additive Manufacturing of Titanium Components by Directed Energy Deposition: Microstructure and Mechanical Properties, Applied Sciences. 7 (2017) 883. https://doi.org/10.3390/app7090883.
[92] S. Vock, B. Klöden, A. Kirchner, T. Weißgärber, B. Kieback, Powders for powder bed fusion: a review, Prog Addit Manuf. 4 (2019) 383–397. https://doi.org/10.1007/s40964-019-00078-6.
[93] Y. Kok, X.P. Tan, P. Wang, M.L.S. Nai, N.H. Loh, E. Liu, S.B. Tor, Anisotropy and heterogeneity of microstructure and mechanical properties in metal additive manufacturing: A critical review, Materials & Design. 139 (2018) 565–586. https://doi.org/10.1016/j.matdes.2017.11.021.
[94] S.S. Al-Bermani, M.L. Blackmore, W. Zhang, I. Todd, The Origin of Microstructural Diversity, Texture, and Mechanical Properties in Electron Beam Melted Ti-6Al-4V,

Metall and Mat Trans A. 41 (2010) 3422–3434. https://doi.org/10.1007/s11661-010-0397-x.
[95] B.E. Carroll, T.A. Palmer, A.M. Beese, Anisotropic tensile behavior of Ti–6Al–4V components fabricated with directed energy deposition additive manufacturing, Acta Materialia. 87 (2015) 309–320. https://doi.org/10.1016/j.actamat.2014.12.054.
[96] L.E. Murr, S.M. Gaytan, E. Martinez, F. Medina, R.B. Wicker, Next Generation Orthopaedic Implants by Additive Manufacturing Using Electron Beam Melting, International Journal of Biomaterials. 2012 (2012) e245727. https://doi.org/10.1155/2012/245727.
[97] D. Barba, C. Alabort, Y.T. Tang, M.J. Viscasillas, R.C. Reed, E. Alabort, On the size and orientation effect in additive manufactured Ti-6Al-4V, Materials & Design. 186 (2020) 108235. https://doi.org/10.1016/j.matdes.2019.108235.
[98] Q. Guo, C. Zhao, L.I. Escano, Z. Young, L. Xiong, K. Fezzaa, W. Everhart, B. Brown, T. Sun, L. Chen, Transient dynamics of powder spattering in laser powder bed fusion additive manufacturing process revealed by in-situ high-speed high-energy x-ray imaging, Acta Materialia. 151 (2018) 169–180. https://doi.org/10.1016/j.actamat.2018.03.036.
[99] E. Fitzgerald, W. Everhart, The Effect of Location on the Structure and Mechanical Properties of Selective Laser Melted 316L Stainless Steel, Solid Freeform Fabrication. (2016) 10.
[100] H. Galarraga, D.A. Lados, R.R. Dehoff, M.M. Kirka, P. Nandwana, Effects of the microstructure and porosity on properties of Ti-6Al-4V ELI alloy fabricated by electron beam melting (EBM), Additive Manufacturing. 10 (2016) 47–57. https://doi.org/10.1016/j.addma.2016.02.003.
[101] T. Wang, Y.Y. Zhu, S.Q. Zhang, H.B. Tang, H.M. Wang, Grain morphology evolution behavior of titanium alloy components during laser melting deposition additive manufacturing, Journal of Alloys and Compounds. 632 (2015) 505–513. https://doi.org/10.1016/j.jallcom.2015.01.256.
[102] S. Palanivel, A.K. Dutt, E.J. Faierson, R.S. Mishra, Spatially dependent properties in a laser additive manufactured Ti–6Al–4V component, Materials Science and Engineering: A. 654 (2016) 39–52. https://doi.org/10.1016/j.msea.2015.12.021.
[103] M.M. Kirka, F. Medina, R. Dehoff, A. Okello, Mechanical behavior of post-processed Inconel 718 manufactured through the electron beam melting process, Materials Science and Engineering: A. 680 (2017) 338–346. https://doi.org/10.1016/j.msea.2016.10.069.
[104] H. Galarraga, R.J. Warren, D.A. Lados, R.R. Dehoff, M.M. Kirka, P. Nandwana, Effects of heat treatments on microstructure and properties of Ti-6Al-4V ELI alloy fabricated by electron beam melting (EBM), Materials Science and Engineering: A. 685 (2017) 417–428. https://doi.org/10.1016/j.msea.2017.01.019.
[105] J. Tiley, T. Searles, E. Lee, S. Kar, R. Banerjee, J.C. Russ, H.L. Fraser, Quantification of microstructural features in α/β titanium alloys, Materials Science and Engineering: A. 372 (2004) 191–198. https://doi.org/10.1016/j.msea.2003.12.008.
[106] G. Lütjering, J.C. Williams, Titanium, Springer Berlin Heidelberg, Berlin, Heidelberg, 2007. https://doi.org/10.1007/978-3-540-73036-1.
[107] M. Kusano, S. Miyazaki, M. Watanabe, S. Kishimoto, D.S. Bulgarevich, Y. Ono, A. Yumoto, Tensile properties prediction by multiple linear regression analysis for selective laser melted and post heat-treated Ti-6Al-4V with microstructural quantification,

Materials Science and Engineering: A. 787 (2020) 139549. https://doi.org/10.1016/j.msea.2020.139549.
[108] A.K. Syed, M. Awd, F. Walther, X. Zhang, Microstructure and mechanical properties of as-built and heat-treated electron beam melted Ti–6Al–4V, Materials Science and Technology. 35 (2019) 653–660. https://doi.org/10.1080/02670836.2019.1580434.
[109] W. Xu, E.W. Lui, A. Pateras, M. Qian, M. Brandt, In situ tailoring microstructure in additively manufactured Ti-6Al-4V for superior mechanical performance, Acta Materialia. 125 (2017) 390–400. https://doi.org/10.1016/j.actamat.2016.12.027.
[110] W. Xu, M. Brandt, S. Sun, J. Elambasseril, Q. Liu, K. Latham, K. Xia, M. Qian, Additive manufacturing of strong and ductile Ti–6Al–4V by selective laser melting via in situ martensite decomposition, Acta Materialia. 85 (2015) 74–84. https://doi.org/10.1016/j.actamat.2014.11.028.
[111] T. Scharowsky, V. Juechter, R.F. Singer, C. Körner, Influence of the Scanning Strategy on the Microstructure and Mechanical Properties in Selective Electron Beam Melting of Ti–6Al–4V, Advanced Engineering Materials. 17 (2015) 1573–1578. https://doi.org/10.1002/adem.201400542.
[112] E. Landau, E. Tiferet, Y.I. Ganor, R.K. Ganeriwala, M.J. Matthews, D. Braun, M. Chonin, G. Ziskind, Thermal characterization of the build chamber in electron beam melting, Additive Manufacturing. 36 (2020) 101535. https://doi.org/10.1016/j.addma.2020.101535.
[113] E. Tiferet, M. Ganor, D. Zolotaryov, A. Garkun, A. Hadjadj, M. Chonin, Y. Ganor, D. Noiman, I. Halevy, O. Tevet, O. Yeheskel, Mapping the Tray of Electron Beam Melting of Ti-6Al-4V: Properties and Microstructure, Materials. 12 (2019) 1470. https://doi.org/10.3390/ma12091470.
[114] Ż.A. Mierzejewska, Effect of Laser Energy Density, Internal Porosity and Heat Treatment on Mechanical Behavior of Biomedical Ti6Al4V Alloy Obtained with DMLS Technology, Materials. 12 (2019) 2331. https://doi.org/10.3390/ma12142331.
[115] G.W. Mugica, D.O. Tovio, J.C. Cuyas, A.C. González, Effect of porosity on the tensile properties of low ductility aluminum alloys, Mat. Res. 7 (2004) 221–229. https://doi.org/10.1590/S1516-14392004000200002.
[116] P. Kumar, K.S.R. Chandran, A Quantitative Relationship to Predict the Effect of Extreme-Sized Pores on Tensile Ductility of Powder Metallurgy Ti-6Al-4V Alloy, in: Proceedings of the 13th World Conference on Titanium, John Wiley & Sons, Ltd, 2016: pp. 1441–1446. https://doi.org/10.1002/9781119296126.ch243.
[117] M. Galati, L. Iuliano, A. Salmi, E. Atzeni, Modelling energy source and powder properties for the development of a thermal FE model of the EBM additive manufacturing process, Additive Manufacturing. 14 (2017) 49–59. https://doi.org/10.1016/j.addma.2017.01.001.
[118] F. Cao, T. Zhang, M.A. Ryder, D.A. Lados, A Review of the Fatigue Properties of Additively Manufactured Ti-6Al-4V, JOM. 70 (2018) 349–357. https://doi.org/10.1007/s11837-017-2728-5.
[119] A. Fatemi, R. Molaei, J. Simsiriwong, N. Sanaei, J. Pegues, B. Torries, N. Phan, N. Shamsaei, Fatigue behaviour of additive manufactured materials: An overview of some recent experimental studies on Ti-6Al-4V considering various processing and loading direction effects, Fatigue & Fracture of Engineering Materials & Structures. 42 (2019) 991–1009. https://doi.org/10.1111/ffe.13000.

[120] P. Li, D.H. Warner, A. Fatemi, N. Phan, Critical assessment of the fatigue performance of additively manufactured Ti–6Al–4V and perspective for future research, International Journal of Fatigue. 85 (2016) 130–143. https://doi.org/10.1016/j.ijfatigue.2015.12.003.
[121] R. Molaei, A. Fatemi, N. Sanaei, J. Pegues, N. Shamsaei, S. Shao, P. Li, D.H. Warner, N. Phan, Fatigue of additive manufactured Ti-6Al-4V, Part II: The relationship between microstructure, material cyclic properties, and component performance, International Journal of Fatigue. 132 (2020) 105363. https://doi.org/10.1016/j.ijfatigue.2019.105363.
[122] J.W. Pegues, S. Shao, N. Shamsaei, N. Sanaei, A. Fatemi, D.H. Warner, P. Li, N. Phan, Fatigue of additive manufactured Ti-6Al-4V, Part I: The effects of powder feedstock, manufacturing, and post-process conditions on the resulting microstructure and defects, International Journal of Fatigue. 132 (2020) 105358. https://doi.org/10.1016/j.ijfatigue.2019.105358.
[123] J. Pegues, M. Roach, R. Scott Williamson, N. Shamsaei, Surface roughness effects on the fatigue strength of additively manufactured Ti-6Al-4V, International Journal of Fatigue. 116 (2018) 543–552. https://doi.org/10.1016/j.ijfatigue.2018.07.013.
[124] B. Vayssette, N. Saintier, C. Brugger, M. Elmay, E. Pessard, Surface roughness of Ti-6Al-4V parts obtained by SLM and EBM: Effect on the High Cycle Fatigue life, Procedia Engineering. 213 (2018) 89–97. https://doi.org/10.1016/j.proeng.2018.02.010.
[125] V.-D. Le, E. Pessard, F. Morel, S. Prigent, Fatigue behaviour of additively manufactured Ti-6Al-4V alloy: The role of defects on scatter and statistical size effect, International Journal of Fatigue. 140 (2020) 105811. https://doi.org/10.1016/j.ijfatigue.2020.105811.
[126] I. Serrano-Munoz, J.-Y. Buffiere, R. Mokso, C. Verdu, Y. Nadot, Location, location & size: defects close to surfaces dominate fatigue crack initiation, Sci Rep. 7 (2017) 1–9. https://doi.org/10.1038/srep45239.
[127] E. Wycisk, A. Solbach, S. Siddique, D. Herzog, F. Walther, C. Emmelmann, Effects of Defects in Laser Additive Manufactured Ti-6Al-4V on Fatigue Properties, Physics Procedia. 56 (2014) 371–378. https://doi.org/10.1016/j.phpro.2014.08.120.
[128] Y. Murakami, Metal Fatigue: Effects of Small Defects and Nonmetallic Inclusions, Academic Press, 2019.
[129] Y.N. Hu, S.C. Wu, Z.K. Wu, X.L. Zhong, S. Ahmed, S. Karabal, X.H. Xiao, H.O. Zhang, P.J. Withers, A new approach to correlate the defect population with the fatigue life of selective laser melted Ti-6Al-4V alloy, International Journal of Fatigue. 136 (2020) 105584. https://doi.org/10.1016/j.ijfatigue.2020.105584.
[130] S.M.J. Razavi, B. Van Hooreweder, F. Berto, Effect of build thickness and geometry on quasi-static and fatigue behavior of Ti-6Al-4V produced by Electron Beam Melting, Additive Manufacturing. 36 (2020) 101426. https://doi.org/10.1016/j.addma.2020.101426.
[131] T. Persenot, A. Burr, G. Martin, J.-Y. Buffiere, R. Dendievel, E. Maire, Effect of build orientation on the fatigue properties of as-built Electron Beam Melted Ti-6Al-4V alloy, International Journal of Fatigue. 118 (2019) 65–76. https://doi.org/10.1016/j.ijfatigue.2018.08.006.
[132] Y. Murakami, M. Endo, Quantitative evaluation of fatigue strength of metals containing various small defects or cracks, Engineering Fracture Mechanics. 17 (1983) 1–15. https://doi.org/10.1016/0013-7944(83)90018-8.
[133] P. Edwards, A. O'Conner, M. Ramulu, Electron Beam Additive Manufacturing of Titanium Components: Properties and Performance, J. Manuf. Sci. Eng. 135 (2013) 061016-061016–7. https://doi.org/10.1115/1.4025773.

[134] Properties and Selection: Nonferrous Alloys and Special-Purpose Materials, ASM International, 1990. https://doi.org/10.31399/asm.hb.v02.9781627081627.
[135] N.E. Dowling, K. Siva Prasad, R. Narayanasamy, Mechanical behavior of materials: engineering methods for deformation, fracture, and fatigue, 4. ed., internat. ed, Pearson, Boston, Mass., 2013.
[136] J. Newman, I. Raju, Stress-Intensity Factor Equations for Cracks in Three-Dimensional Finite Bodies, in: J. Lewis, G. Sines (Eds.), Fracture Mechanics: Fourteenth Symposium—Volume I: Theory and Analysis, ASTM International, 100 Barr Harbor Drive, PO Box C700, West Conshohocken, PA 19428-2959, 1983: p. I-238-I-238–28. https://doi.org/10.1520/STP37074S.
[137] P.R. Carriere, S. Yue, Energy absorption during pulsed electron beam spot melting of 304 stainless steel: Monte-Carlo simulations and in-situ temperature measurements, Vacuum. 142 (2017) 114–122. https://doi.org/10.1016/j.vacuum.2017.04.039.
[138] W. Yan, W. Ge, J. Smith, S. Lin, O.L. Kafka, F. Lin, W.K. Liu, Multi-scale modeling of electron beam melting of functionally graded materials, Acta Materialia. 115 (2016) 403–412. https://doi.org/10.1016/j.actamat.2016.06.022.
[139] Y. Murakami, S. Aoki, N. Hasebe, Y. Itoh, H. Miyata, N. Miyazaki, H. Terada, K. Tohgo, M. Toya, R. Yuuki, Stress Intensity Factor Handbook, Vol. 1 and 2, Pergamon Press, NY, 1987.
[140] Y. Murakami, M. Endo, Effects of defects, inclusions and inhomogeneities on fatigue strength, International Journal of Fatigue. 16 (1994) 163–182. https://doi.org/10.1016/0142-1123(94)90001-9.
[141] Y. Murakami, Material defects as the basis of fatigue design, International Journal of Fatigue. 41 (2012) 2–10. https://doi.org/10.1016/j.ijfatigue.2011.12.001.

APPENDIX A

Table A.1. Tensile properties for the horizontally oriented parts from the powder reuse study.

Build Number	Elastic Modulus (GPa)	Yield Strength (MPa)	Ultimate Tensile Strength (MPa)	Elongation at Failure (%)
1	92.7	738.8	857.4	9.28
2	100.0	806.3	933.5	9.56
3	100.8	820.5	951.0	8.47
4	102.1	826.6	950.6	8.42
5	107.5	853.4	981.6	8.37
6	109.6	856.6	978.5	7.65
7	107.0	840.5	960.5	9.22
8	99.0	829.6	948.0	7.82
9	96.4	862.1	974.7	7.17
10	107.7	837.4	939.8	6.38
11	104.8	860.0	959.8	5.93
12	105.8	860.6	961.3	5.54
13				
14	101.3	862.5	957.1	5.53
15	106.8	860.3	969.8	6.28
16	109.3	933.2	1031.4	5.56
17	106.7	930.3	1022.7	5.09
18	107.5	936.2	1021.1	4.56
19	113.4	947.3	1051.1	5.06
20	101.9	927.5	1007.6	4.30
21	107.0	971.7	1071.3	5.02
22	108.5	989.2	1072.1	4.17
23	113.6	1001.1	1088.4	4.21
24	106.1	992.6	1066.7	3.62
25	97.4	1022.0	1098.3	3.61
26	108.2	998.8	1090.9	4.56
27	112.0	1014.9	1099.5	4.10
28	105.5	1027.5	1101.0	3.32
29	106.2	1011.8	1075.4	2.93
30	109.4	1050.3	1122.1	3.53

Table A.2. Tensile Properties for the vertically oriented parts from the powder reuse study.

Build Number	Elastic Modulus (GPa)	Yield Strength (MPa)	Ultimate Tensile Strength (MPa)	Elongation at Failure (%)
1	100.7	761.0	888.0	11.67

2				
3				
4	106.4	808.9	934.9	10.70
5	108.9	813.7	942.0	10.44
6	104.2	810.5	936.9	10.60
7	99.9	812.3	860.7	3.16
8	103.7	837.6	954.5	9.49
9	111.7	843.3	938.8	7.75
10	116.0	838.5	923.5	6.91
11	109.4	845.6	943.7	7.32
12	99.9	821.5	949.0	9.82
13				
14	102.8	831.7	960.5	10.50
15	113.5	866.2	998.5	9.71
16	111.0	895.7	1032.8	10.08
17	107.5	904.9	1044.1	10.42
18	108.9	937.7	1075.1	9.94
19				
20	112.6	939.0	1074.8	9.18
21	111.2	948.3	1088.7	9.09
22	108.8	968.8	1109.1	9.43
23	111.9	966.3	1095.6	8.49
24	113.2	955.7	1095.9	9.39
25	108.9	972.6	1095.1	7.77
26	113.8	969.8	1109.7	8.64
27	107.9	984.5	1109.9	7.73
28	109.6	995.2	1122.6	7.59
29	111.2	986.1	1122.2	8.20
30	108.9	1005.3	1129.0	7.34

VITA

Sean Ghods

Education:

Ph.D., University of Washington, Seattle, WA **2018 - 2021**
Doctor of Philosophy in Materials Science and Engineering

Dissertation: Origins of Variability in Electron Beam Powder Bed Fusion of Ti6Al4V

M.S., University of Washington, Seattle, WA **2016 - 2018**
Master of Science in Materials Science and Engineering

Thesis: Design of Biomimetic Armor Based on Strain Rate Sensitive Natural Dermal Armor

B.S., University of Washington, Seattle, WA **2012 - 2016**
Major: Materials Science in Engineering

Awards/Honors:

University of Washington, Seattle, WA

- Distinguished Thesis Award for Master's Thesis
- Stoebe Fellowship
- Torrence Tech Fellowship
- Comotion Innovation Fund Award

Publications:

[1] **S. Ghods**, R. Schur, E. Schultz, R. Pahuja, A. Montelione, C. Wisdom, D. Arola, M. Ramulu, Powder reuse and its contribution to porosity in additive manufacturing of Ti6Al4V, Materialia. 15 (2021) 100992. https://doi.org/10.1016/j.mtla.2020.100992.

[2] R. Schur, **S. Ghods**, C. Wisdom, R. Pahuja, A. Montelione, D. Arola, M. Ramulu, Mechanical anisotropy and its evolution with powder reuse in Electron Beam Melting AM of Ti6Al4V, Materials & Design. 200 (2021) 109450. https://doi.org/10.1016/j.matdes.2021.109450.

[3] **S. Ghods**, E. Schultz, C. Wisdom, R. Schur, R. Pahuja, A. Montelione, D. Arola, M. Ramulu, Electron beam additive manufacturing of Ti6Al4V: Evolution of powder morphology and part microstructure with powder reuse, Materialia. 9 (2020) 100631. https://doi.org/10.1016/j.mtla.2020.100631.

[4] **S. Ghods**, S. Waddell, E. Weller, C. Renteria, H.-Y. Jiang, J.M. Janak, S.S. Mao, T.J. Linley, D. Arola, On the regeneration of fish scales: structure and mechanical behavior, Journal of Experimental Biology. 223 (2020). https://doi.org/10.1242/jeb.211144.

[5] R. Schur, **S. Ghods**, E. Schultz, C. Wisdom, R. Pahuja, A. Montelione, D. Arola, M. Ramulu, A Fractographic Analysis of Additively Manufactured Ti6Al4V by Electron Beam Melting: Effects of Powder Reuse, J Fail. Anal. and Preven. (2020). https://doi.org/10.1007/s11668-020-00875-0.

[6] A. Montelione, **S. Ghods**, R. Schur, C. Wisdom, D. Arola, M. Ramulu, Powder Reuse in Electron Beam Melting Additive Manufacturing of Ti6Al4V: Particle Microstructure, Oxygen Content and Mechanical Properties, Additive Manufacturing. 35 (2020) 101216. https://doi.org/10.1016/j.addma.2020.101216.

[7] H. Jiang, **S. Ghods**, Y. Ma, X. Dai, F. Yang, X. He, Designed for the enhancement of structure mechanostability and strength: Suture-serrate margins of bivalve shells, Journal of the Mechanical Behavior of Biomedical Materials. 103 (2020) 103586. https://doi.org/10.1016/j.jmbbm.2019.103586.

[8] H. Jiang, **S. Ghods**, E. Weller, S. Waddell, E.A. Ossa, F. Yang, D. Arola, Contributions of intermolecular bonding and lubrication to the mechanical behavior of a natural armor, Acta Biomaterialia. 106 (2020) 242–255. https://doi.org/10.1016/j.actbio.2020.02.014.

[9] **S. Ghods**, S. Murcia, E.A. Ossa, D. Arola, Designed for resistance to puncture: The dynamic response of fish scales, Journal of the Mechanical Behavior of Biomedical Materials. 90 (2019) 451–459. https://doi.org/10.1016/j.jmbbm.2018.10.037.

[10] D. Arola, **S. Ghods**, C. Son, S. Murcia, E.A. Ossa, Interfibril hydrogen bonding improves the strain-rate response of natural armour, Journal of The Royal Society Interface. 16 (2019) 20180775. https://doi.org/10.1098/rsif.2018.0775.